HEINRICH HEINE
UNIVERSITÄT DÜSSELDORF

Theoretical Investigations on Chemical Structures and Reaction Mechanisms Using Semi-empirical and Density Functional Methods

Inaugural-Dissertation

zur
Erlangung des Doktorgrades der
Mathematisch-Naturwissenschaftlichen Fakultät
der Heinrich-Heine-Universität Düsseldorf

vorgelegt von
Berit Walter
aus Offenbach am Main

Mülheim an der Ruhr, Düsseldorf, Dezember 2015

Gedruckt mit der Genehmigung der Mathematisch-Naturwissenschaftlichen
Fakultät der Heinrich-Heine-Universität Düsseldorf

Referent: Herr Prof. Dr. Walter Thiel
Koreferentin: Frau Prof. Dr. Christel Marian
Tag der mündlichen Prüfung: 1. Februar 2016

Hiermit versichere ich an Eides Statt, dass die Dissertation von mir selbstständig und ohne unzulässige fremde Hilfe unter Beachtung der „Grundsätze zur Sicherung guter wissenschaftlicher Praxis an der Heinrich-Heine-Universität Düsseldorf“ erstellt worden ist. Die Dissertation wurde in der vorgelegten oder in ähnlicher Form noch bei keiner Institution eingereicht. Ich habe keine erfolglosen Promotionsversuche unternommen.

Mülheim an der Ruhr, den 3. Dezember 2015

(Berit Walter)

Abstract

This thesis presents the results of investigations on chemical structures and reaction mechanisms. All investigations reported here employed theoretical methods especially semi-empirical and Density Functional Theory methods.

The semi-empirical OM2/MRCI method was used to study the origin of photostability of the nucleobase guanine. It is known from experiment that nucleobases in general strongly absorb in the UV/VIS range but there exist decay mechanisms that prevent damage to the molecule. The decay of excited guanine in water was simulated through surface hopping dynamics and the geometrical changes along the decay pathway were monitored. The use of a QM/MM computational setup allowed a detailed study of solvent effects in aqueous solution. Comparing the results with those obtained in the gas phase reveals that the preferred decay channels change and that the decay is faster in aqueous solution, while the optimized geometries of the ground and first excited state and of the relevant conical intersections are similar in the gas phase and in solution. The results are in good agreement with static *ab initio* computations and with the available experimental studies, which validates the application of the semi-empirical OM2/MRCI method. The time evolution of the computed excited-state ionization potentials is consistent with recent experimental results from ultrafast photoelectron spectroscopy on guanosine in water.

Density Functional Theory methods were used to answer questions on chemical structure and reaction mechanisms raised by experimental investigations. Concerning structures the question was how to describe the bonding interactions of bimetallic gold-chromium complexes and whether these complexes are carbenes. Starting from the crystal structure the geometries of the complexes were optimized and then these structures were examined by using NBO analysis, fragment analysis, and the AIM method. It was found that these complexes are best described as chromium-carbenes with a gold unit coordinated to the C-Cr bond in an η^2 mode.

On the mechanistic side, an organocatalytic reaction and the reaction of an organoferrate complex were studied. In the first case the issue was whether the ring closing reaction of an unsaturated hydrazone could be regarded as a pericyclic electrocyclization or not. The analysis showed that it is better classified as an intramolecular nucleophilic addition (structurally) or a pseudopericyclic reaction (electronically); it is not pericyclic as confirmed by comparison with the cyclization of the pentadienyl anion which is known to cyclize in a pericyclic manner. In the second case study, methylation reactions mediated by an organoferrate complex were found to proceed via a substitution mechanism. In agreement with experiment up to four methyl groups can be transferred per ferrate complex, the first three in a facile manner and the fourth one with some more activation. This demonstrates the ability of ferrate complexes to alkylate, and hence their potential to act as intermediates in iron cross coupling reactions.

Zusammenfassung

In der vorliegenden Arbeit werden die Ergebnisse zu Untersuchungen chemischer Strukturen und Reaktionsmechanismen vorgestellt. Alle Untersuchungen wurden mit theoretischen Methoden, insbesondere semi-empirischen und Dichte-Funktional-Methoden durchgeführt.

Die semi-empirische OM2/MRCI Methode wurde verwendet, um die Ursachen für die Photostabilität der Nucleobase Guanin aufzuklären. Experimentell ist bekannt, dass Nucleobasen allgemein im UV/VIS-Spektrum absorbieren, aber über Abregungsmechanismen verfügen, die eine Beschädigung des Moleküls verhindern. Mit dynamischen Surface Hopping-Rechnungen wurde die Abregung von Guanin simuliert und die geometrischen Änderungen entlang des Abregungspfads verfolgt. Dabei wurden die Umgebungseffekte einer wässrigen Lösung durch die Verwendung eines QM/MM Ansatzes berücksichtigt. Im Vergleich zu Rechnungen in der Gasphase sind in wässriger Lösung Relaxationspfade mit anderen geometrischen Verzerrungen bevorzugt. Die Abregungsrate ist in wässriger Lösung etwas größer, während die optimierten Geometrien der Minima im Grund- und ersten angeregten Zustand sowie an den konischen Durchschneidungen ähnlich sind. Die Ergebnisse sind in guter Übereinstimmung mit statischen *ab initio* Rechnungen und mit experimentellen Untersuchungen, so dass die Anwendung der semi-empirischen OM2/MRCI Methode gerechtfertigt ist. Die zeitliche Abhängigkeit der berechneten Ionisierungspotentiale im angeregten Zustand ist konsistent mit aktuellen experimentellen Daten aus Untersuchungen an Guanosin in Wasser mittels ultraschneller Photoelektronenspektroskopie.

Methoden der Dichte-Funktional-Theorie wurden angewendet, um aus Experimenten resultierende Fragen zu Strukturen oder Reaktionsmechanismen zu beantworten. In struktureller Hinsicht wurde analysiert, wie die Bindungsverhältnisse in bimetallischen Gold-Chrom-Komplexen zu beschreiben sind und ob in diesen Komplexen Carben-Bindungen vorliegen. Ausgehend von den Kristallstrukturen wurden die Geometrien optimiert und dann mit Hilfe von NBO-Analyse, Fragmentanalyse und der AIM-Methode untersucht. Fazit ist, dass sich die Verbindungen am besten als Chrom-Carbene beschreiben lassen, wobei die Goldeinheit in η^2-Orientierung an die Chrom-Kohlenstoffbindung koordiniert.

Auf der mechanistischen Seite wurden eine organokatalytische Reaktion und die Reaktion eines Organoferratkomplexes untersucht. Im ersten Fall ging es darum, ob es sich bei der Ringschlussreaktion eines ungeättigten Hydrazons um eine Elektrozyklisierung handelt oder nicht. Die Analyse ergab, dass die Reaktion als eine intramolekulare nucleophile Addition oder eine pseudoperizyklische Reaktion klassifiziert werden kann, je nach Betrachtungsweise; sie ist nicht perizyklisch, wie durch den Vergleich mit der bekanntermaßen perizyklisch verlaufenden Zyklisierung des Pentadienylanions belegt werden konnte. In der zweiten Fallstudie wurde gezeigt, dass der experimentell zur Methylierung eingesetzte Ferratkomplex bis zu vier Methylgruppen durch Substitution an das Substrat übertragen kann. Dies zeigt, dass Organoferratkomplexe zur Alkylierung in eisenkatalysierten Kreuzkupplungsreaktionen eingesetzt werden können.

List of papers included in this thesis

1. Nonadiabatic decay dynamics of 9H-Guanine in aqueous solution

   Berit Heggen, Zhenggang Lan and Walter Thiel, *Phys. Chem. Chem. Phys.*, **2012**, 14, 8137 – 8146.

   Carried out and analyzed all the calculations in the paper.

2. Excited-state dynamics of Guanosine in aqueous solution revealed by time-resolved photoelectron spectroscopy: experiment and theory

   Franziska Buchner, **Berit Heggen**, Hans-Hermann Ritze, Walter Thiel and Andrea Lübke, *Phys. Chem. Chem. Phys.*, **2015**, 17, 31978-31987.

   Carried out and analyzed the calculations of 9H-guanine in aqueous solution for the evaluation of the ionization potential along the decay pathways.

3. Gold carbenoids: lessons learnt from a transmetalation approach

   Günter Seidel, Barbara Gabor, Richard Goddard, **Berit Heggen**, Walter Thiel and Alois Fürstner, *Angew. Chem. Int. Ed.*, **2014**, 53, 879 – 882.

   Performed the theoretical investigations in the paper.

4. Cyclization of an α,β-unsaturated hydrazone catalyzed by a BINOL-phosphoric acid: pericyclic or not?

   Berit Heggen, Mahendra Patil, Walter Thiel, *J. Comput. Chem.*, **2016**, 37, 280 – 285.

   Carried out and analyzed all the calculations in the paper.

5. Theoretical investigation on the mechanism of iron catalyzed cross coupling reactions via ferrate intermediates

   Berit Heggen, Walter Thiel, *J. Organomet. Chem.*, **2016**, 804, 42 – 47.

   Carried out and analyzed all the calculations in the paper.

Danksagung

Herr Thiel, ich danke Ihnen für das Vertrauen, das Sie mir entgegengebracht haben. Vielen Dank, dass Sie immer mit Rat, Wissen und Erfahrung weitergeholfen haben, mir eine sehr große Eigenständigkeit ermöglicht haben und immer wieder offen und flexibel reagiert haben.

Vielen Dank an meine Projektpartner in der Theorie-Gruppe für viele hilf- und lehrreiche Gespräche, insbesondere an Zhenggang Lan, Gopinadhanpillai Gopakumar und Mahendra Patil. Auch meinen Projektpartnern aus experimentellen Gruppen danke ich herzlich für ihre Fragen, Einblicke und Diskussionen: Alois Fürstner, Jens Willwacher, Richard Goddard, Benjamin List, Steffen Müller und Andrea Lübcke.

Ein dickes Dankeschön an Horst Lenk: Ohne Dich wäre so manches technische Problem vermutlich heute noch ein Problem – vielen Dank für schnelle und gute Hilfe nahezu jederzeit. Bei technischen Fragen nicht zu vergessen ist natürlich Volker Schmidts, denn „der Computer macht, was Du sagst, Du musst eben sagen, was er machen soll“. Danke dafür und dass Du mir dann auch verraten hast, was ich dem Computer genau sagen soll. Und danke für die Hilfe insbesondere bei allen Verwaltungsfragen und „sonstigen Kleinigkeiten“ an Ursula Scheifhacken und Monika Lickfeld.

Da ich ja eine ganze Weile Mitglied der Theorie-Gruppe in der Kofo war, habe ich viele Kollegen kennen gelernt und mich immer über die spannenden Diskussionen gefreut, die wissenschaftlichen wie auch alle anderen von Cricket bis Weltmeisterschaft und immer mit internationalem Anstrich. Ein Highlight jeden Tages: die Doppelkopfrunde in der Mittagspause. Danke an all die Mitspieler: Claudia, Felix, Jan, Lasse, Mahendra, Peter, Rasmus, Thibaut, Victor (kein Anspruch auf Vollständigkeit). Für die tolle Unterstützung gerade zu Beginn am MPI vielen Dank an Tobias Benighaus, Sebastian Metz und Mark Waller. Elliot Boulanger und Claudia Loerbroks: Euch ein herzliches Dankeschön für unsere sehr kurzweilige Bürogemeinschaft und Eure Freude, wenn mal wieder Mittwoch war. Und Claudia: Vielen Dank für Deine Hilfe bei meinen Versuchen mit Zucker und dem Schreiben dieser Arbeit. Und Dir Jan Philipp Götze: vielen Dank für Deine Antworten bei allerlei wichtigen und unwichtigen Fragen, und die vielen Diskussionen über theoretische Chemie und die Wissenschaft an sich.

Die größte Hilfe aber habe ich immer und in allen Lagen von Dir bekommen, Dominic. Ich danke Dir, dass Du mich immer unterstützt hast, Geduld mit mir hattest und mir Mut gemacht hast. Und vor allem, dass Du Dich mit mir an das größte Experiment überhaupt gewagt hast.

Contents

Chapter 1

Introduction

The determination of chemical structures and reaction mechanisms is an important field in chemical research. In the second half of the 19th century the basic postulates of our modern understanding of chemical structure of organic compounds were introduced by Couper, Kekulé and Butlerov.[1–3] They were first in postulating the tetravalence of carbon and the idea of linking atoms in a unique structure in space to form a certain molecule. As spectroscopic techniques and X-ray crystallography had not been invented by that time no methods were available to the chemists to elucidate the structure of molecules by physical methods. They were forced to prove their ideas on chemical structure and reactivity by wet chemistry experiments. In the early 20th century Lewis structures were introduced allowing to represent not just the probable geometry but as well partly the electronic structure of a chemical compound.[4]

The development of organic structure theory by the end of the 19th century caused ever more strategic synthesis of organic compounds.[5] So, new reactions could be started by guessing structures and applying knowledge about reactivities. Attempts were made to describe chemical reactions by reaction equations, developing the concept of transition states and deriving mathematical formulas to calculate the rate of reactions. The latter was in the beginning based on the kinetic theory of gases assuming that two molecules with sufficient energy must hit each other in the reaction mixture to react with each other. Refinements to this theory were made by *e.g.* introducing a steric factor taking into account that molecules are not spherically symmetric and therefore have to hit each other at the right side. Finally, including the idea of the non-observable transition states and assuming a fast pre-equilibrium between reactants and transition states led to the development of transition state theory in 1935 by Eyring, Evans and Polanyi.[6,7]

The development of quantum mechanics initiated by the publications of

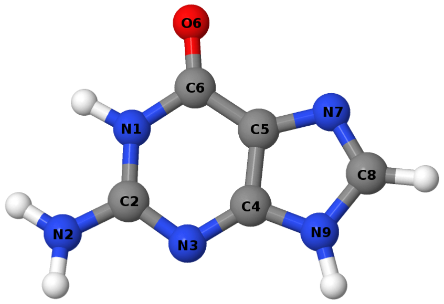

Figure 1.1: Graphical representation of the biological relevant 9*H*-tautomer of the nucleobase guanine.

Heisenberg[8] and Schrödinger[9] gave the theoretical foundations to gain insight into chemical structure and reactivity. Quantum chemistry offered a new mathematical framework to describe the postulated concepts like bonding in molecules on an electronic level. The early days of quantum chemistry already witnessed the derivation of the Hartree-Fock equations and the Hückel model was used to perform simple calculations on π systems. But in general, quantum mechanical computations that would address real chemical questions were impossible by that time due to the lack of appropriate computer power. In the following decades, the development of ever more powerful computers (starting in the 1940s and ever since continuing) and of a hierarchy of approximate quantum chemical methods (*ab initio*, density functional theory, and semi-empirical methods) made it increasingly possible to tackle chemical problems by using theoretical methods. Today many computational approaches are available for theoretical chemists to answer questions on chemical structure and reactivity for small, medium-sized, and even large molecular systems, including solvent or surface effects.

The main advantage of theoretical methods is the capability to investigate the object of interest on an atomistic and even electronic scale. This is still difficult to achieve with experimental techniques especially with regard to dynamic processes such as chemical reactions. On the theoretical side, problematic issues are, depending on the systems investigated, insufficient accuracy and high computational costs. Techniques like X-ray crystallography, atom-force-microscopy and nuclear magnetic resonance spectroscopy already allow very detailed insight into chemical structures. However, such experimental investigations often do not deliver unambiguous and comprehensive results, even when combining different techniques. Theoretical electronic structure methods can provide complementary information and can offer a detailed atomistic understanding of molecules and their reactions – even though one should always remember that this is limited by the approximations necessary to make the underlying calculations feasible.

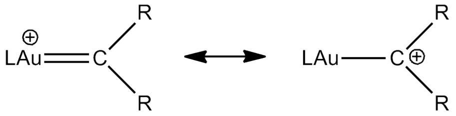

Figure 1.2: Gold carbenoid structures under discussion: gold-carbon double bond with positive charge centered at the gold atom (left side) or gold-carbon single bond with the positive charge centered at the carbon atom (right side).

In the field of chemical structure and reaction mechanisms, a combined experimental and theoretical approach can be very successful. Some examples will be given in this thesis. To start with, the biologically relevant $9H$-tautomer of the nucleobase guanine (see Figure 1.1) in aqueous solution is studied, with focus on its photostability and the changes in geometry upon deexcitation. The nucleobases are key building blocks of the DNA, and hence their stability against environmental influences is important. Even though nucleobases strongly absorb sun light they are highly photostable as the quantum yield is very low.[10] Most likely this is due to deexcitation by ultrafast nonradiative decay through conical intersections. At a conical intersection different potential energy surfaces cross; in the case of the nucleobases this requires severe distortions of the aromatic systems. The decay rates of the nucleobases have been studied using various experimental methods, but structural changes are difficult to observe in these ultrafast relaxation processes. The use of semi-empirical quantum chemical methods in combination with molecular dynamics allows the simulation of these processes and affords insight into the geometrical changes and competing deexcitation channels. Environmental effects such as solvent effects can be taken into account through multiscale modeling.

Chemical bonding is a theoretical concept to describe the interactions of atoms in molecules. The bonding situation in gold carbenoides as intermediates in π-acid catalysis is under debate for some time already.[11] Two bonding schemes are suggested as shown in Figure 1.2: Either a gold-carbon double bond with the positive charge centered at gold (carbene structure description) or a gold-carbon single bond with the positive charge centered at carbon (carbocation structure description, strictly speaking no carbene). Short-lived intermediates in catalytic reactions are usually difficult to characterize experimentally, for example with regard to bonding interactions. Therefore, Fürstner and coworkers attempted to synthesize unstabilized gold carbenoids via carbene transfer from chromium carbenes,[12] a well-established procedure for preparing Fischer-type gold carbenoids. Unexpectedly, they found that the carbene was not transferred to the gold moiety but rather a bimetallic complex was formed. The available analytic methods such as X-ray crystallography and NMR spectroscopy were

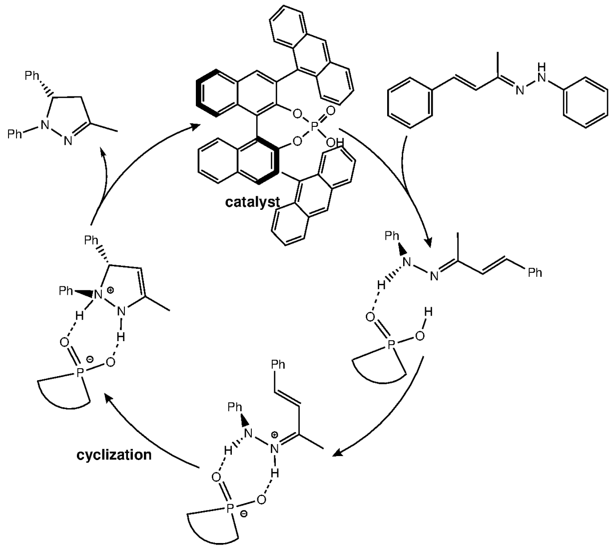

Figure 1.3: Schematic representation of the cyclization reaction studied experimentally.

not sufficient to understand the bonding in these complexes, and in particular they could not answer the question whether the prepared structures are gold carbenoids at all. Density Functional Theory (DFT) methods were employed to analyze the geometry and bonding of these bimetallic complexes in detail using methods such as natural bond orbital (NBO) or atoms-in-molecules (AIM) analysis.

Another important field is chemical reactivity where one wants to know on an atomistic or even electronic scale what happens in a chemical reaction: for example, which atoms interact with each other in the reaction, which are the influences of the surrounding atoms and the environment, and which are the most likely reaction pathways. Theoretical calculations can nowadays provide reasonable structures of intermediates and experimentally not observable transition states, as well as realistic energy profiles, thus allowing the evaluation of reaction pathways and kinetics. This helps to understand the underlying mechanisms of *e.g.* catalyzed reactions, to advance the control over chemical reactions, and to design molecules with desired properties. Two examples from the wide field of catalysis will be addressed in this thesis: firstly, the analysis of the mechanism of an organocatalytic reaction especially with regard to the electronic structure of the crucial transition state, and secondly, an investigation on an iron complex as supposed intermediate in iron catalyzed cross-coupling reactions.

A rather new concept in the field of organocatalysis is asymmetric counteranion-

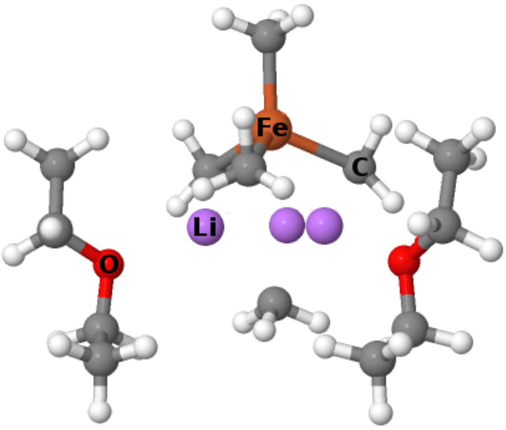

Figure 1.4: Organoferrate complex as synthesized and used for alkylation reactions by Fürstner *et al.*.[15]

directed catalysis (ACDC),[13] where the enantioselectivity of a catalytic reaction is caused by ion pairing of a cationic intermediate with an enantiomerically pure anion formed by the catalyst. Often chiral Brønsted acids are used to generate the anions, while at the same time activating the reactant by protonation. Common representatives of such Brønsted acids are 1,1'-bi-2-naphthol (BINOL) derived phosphoric acids. ACDC by itself does not determine the mechanism of the reaction catalyzed. Müller and List suggested for a recent example of ACDC a pericyclic ring closure (see Figure 1.3)[14] since the stereochemical outcome agreed with the requirements for thermal 6π-electrocyclization. Alternative mechanisms can be envisioned; for example, the stereochemistry may be determined by the chiral counteranion. In view of these uncertainties, a DFT study was performed to analyze the electronic structure of reactants and transition states.

The cross-coupling reactions forming carbon-carbon or carbon-heteroatom bonds catalyzed by noble metals such as platinum or palladium are well-established in organic synthesis. Their development has been honored by the 2010 Nobel prize in chemistry.[16,17] These reactions are indeed potent and versatile tools but the need for expensive catalysts and the presence of toxic salts is unfavorable. If an environmentally benign, cheap, and nontoxic metal such as iron could take over the central role in the cross-coupling catalysis, the method would become even more valuable. Several successful iron-catalyzed cross-coupling reactions have already been published but many mechanistic details still need to be clarified.[18,19] It is commonly agreed that different mechanisms may operate under different reaction conditions:[20] either catalytic cycles comprising oxidative addition/transmetalation/reductive elimination, in analogy to palladium-catalyzed cross-coupling reactions, or so-called -ate mechanisms involving highly alkylated iron species.[19, 21] These mechanisms have been studied by experiments and computations[18, 22, 23] for certain reactions. Generally speaking, intermediates in catalytic processes are difficult to be trapped and analyzed. As a step towards identifying possible intermediates in iron-catalyzed cross-coupling reactions, Fürstner and co-workers prepared organoferrate complexes stable enough for X-ray crystallography and demonstrated their ability to mediate alkylation reactions (as required for their supposed catalytic cross-coupling activity).[15] For a more detailed mechanistic understanding, DFT computations were carried out for the alkylation of 4-chlorobenzoylchloride by the organoferrate complex shown in Figure 1.4.

Chapter 2

Theoretical Methods

In this chapter a short overview is given about the basic concepts of theoretical and computational chemistry. This part provides a brief introduction to the methods used to investigate the reported structures and reaction mechanisms, *i.e.* semi-empirical methods for nonadiabatic dynamics and density functional theory (DFT). For more details on the formalism and the derivations please refer to the original publications or standard textbooks on computational chemistry.[24–27]

In general, the predominant purpose of applied theoretical and computational chemistry is to solve the time-independent Schrödinger equation of a given system:

$$\mathcal{H}\Psi = E\Psi \tag{2.1}$$

where $\mathcal{H}$ is the Hamiltonian, an operator corresponding to the total energy E of a system described by its wave function Ψ. In only very few cases, such as a particle in a box, equation 2.1 is analytically solvable, but approximations are generally necessary when solving the Schrödinger equation for chemically relevant molecular systems. A first step is the Born-Oppenheimer approximation: as the nuclei are much heavier than the electrons the latter can almost immediately adjust to changes in the positions of the nuclei. Since the nuclei move much more slowly than the electrons, they can be assumed to be fixed. Therefore the wave function can be separated into two parts:

$$\Psi_{tot}(nuclei, electrons) = \Psi(nuclei)\Psi(electrons) \tag{2.2}$$

Analogously the energy can be represented as the sum of nuclear energy (electrostatic repulsion between nuclei) and electronic energy (kinetic energy, potential energy of the electrons in the field of the nuclei, and electron-electron repulsion). Evaluating the energy as a function of the positions of the nuclei leads to a sampling of the potential energy surface (PES) with respect to the nuclear coordinates. Further separation of the electronic variables is achieved by approximating the electronic wave function of a polyelectronic system by an antisymmetrized product of one-electron wave functions, representing spin orbitals χ_i. This results in a so-called Slater determinant. In the Hartree-Fock approach (HF) this Slater determinant is varied to find the lowest energy possible by solving the Hartree-Fock equation:[28–30]

$$f_i\chi_i = \epsilon_i\chi_i \tag{2.3}$$

where f_i is the one-electron Fock operator acting on orbital χ_i. The Fock operator includes the kinetic and potential energy of an electron resulting from the electron-nuclei interactions and the Hartree-Fock potential induced by the N-1 remaining electrons of the system. The latter includes both a Coulomb operator for Coulomb repulsion and an exchange operator. As the solution of the Hartree-Fock equation for a given electron affects the solution for all other electrons, the equations are solved in a self-consistent field approach (SCF). In more detail, an initial guess for the Slater determinant is used to calculate the Coulomb and exchange operators, then the HF equation is solved to obtain a new Slater determinant, and this is repeated until the energy and Slater determinant do not change anymore, *i.e.* until self-consistency is reached. The variational principle ensures that the approximate energy obtained from this iterative procedure will remain above the true energy.

An efficient way to solve the HF equation was introduced by Roothaan and Hall in 1951, by introducing a basis and thus transforming the integro-differential HF equation to a matrix form:[31, 32]

$$\mathbf{FC} = \mathbf{SCE} \tag{2.4}$$

where **F** is the Fock matrix, **C** is the eigenvector matrix containing the coefficients of the basis orbitals, **S** is the overlap matrix, and **E** is the diagonal matrix of the orbital energies.

In the Hartree-Fock approach electron correlation is neglected. The difference between the Hartree-Fock energy and the true energy of a system is called the correlation energy. One possible way to include electron correlation is to apply configuration interaction (CI). The full CI wave function is a linear combination of all Slater determinants that can be built from the Hartree-Fock reference determinant by including all possible excitations. As the number of possible configurations increases quickly with excitation level, usually only a limited number of excitations is taken into account, for example, only single and double excitations (CISD). When both the orbitals and the CI coefficients are optimized, the method is called multiconfiguration self-consistent field method (MCSCF).

Another way to limit the number of excitations taken into account is the definition of an active space that includes only a limited number of orbitals (usually located above and below the highest occupied orbital). In a complete active space (CAS) treatment, all possible excitations within the range of orbitals are taken into account. When combined with MCSCF this treatment is called CASSCF.

An efficient way to increase the accuracy of CI methods is to introduce several reference configurations and to perform multi-reference configuration interaction (MRCI) calculations. Generally speaking, one major advantage of CI methods is their flexibility and their ability to deal not only with the electronic ground state but also with systems in electronically excited states. The CI methods and their MCSCF or CASSCF variants are variational and thus provide an upper bound to the true energy.

2.1 Semi-empirical Methods and Nonadiabatic Dynamics

In *ab initio* HF calculations most of the computational effort is needed to manipulate and calculate the integrals in the Fock matrix and the Roothaan-Hall equation 2.4. Semi-empirical methods neglect many of the integrals and approximate the remaining ones thereby saving computational effort. For instance, the Roothaan-Hall equation is simplified by replacing the overlap matrix $\mathbf{S}$ by the unity matrix $\mathbf{I}$. Furthermore, only valence electrons are treated in semi-empirical calculations while the core electrons are absorbed into the nuclear core. Many of the non-vanishing integrals are represented by parameters or parametric functions in an attempt to compensate for the approximations in the semi-empirical formalism. The quality of a semi-empirical method is strongly dependent on the quality of the chosen parameters. Usually these are optimized with respect to experimental and/or high level *ab initio* reference data, for example atomization energies and geometries of reference molecules in suitable training sets.

The semi-empirical method employed here is the orthogonalization model 2 (OM2),[33] which is based on the neglect of diatomic differential overlap (NDDO).[34] Compared with traditional NDDO approaches, the OM2 method includes additional orthogonalization corrections to better model conformational effects and electronically excited states. It has been parameterized for hydrogen, carbon, oxygen, nitrogen, and fluorine.

The combination of the OM2 method with MRCI allows for the treatment of excited states. MRCI is efficiently implemented for semi-empirical methods using the graphical unitary group approach (GUGA).[35] The OM2/MRCI method can be used not only for static excited-state calculations, for example to explore the potential energy surface (PES) in the Franck-Condon region, but also for dynamics simulations to monitor the temporal evolution of the excited states. Following the nuclear motion on the excited-state PES may lead to regions where different states get close to each other or even cross. In this case, nonadiabatic processes become possible and it is necessary to go beyond the Born-Oppenheimer approximation to model the system. Nonadiabatic processes can be described dynamically, *i.e.* with regard to their time evolution, by nonadiabatic excited-state simulations. For this purpose, the Tully surface hopping method[36] was chosen, which treats the system in a semi-classical way: the nuclei are propagated by classical molecular dynamics (MD) on an adiabatic surface, whereas the electronic energies, gradients, and coupling terms for the relevant PES are computed by a quantum-chemical method on the fly at each MD step. Based on a probability measure evaluated from a random fewest-switches algorithm, the system is allowed to change the electronic state, *i.e.* to "hop" from one PES to another, which corresponds to a nonadiabatic transition. A large number of trajectories must be computed to obtain statistically meaningful results as an average over these trajectories.

2.2 Density Functional Theory

In their seminal work Hohenberg and Kohn laid the foundations of Density Functional Theory (DFT) in 1964.[37] They showed that the electronic energy of a non-degenerate ground state system is uniquely defined by its electron density ρ. Thus the electronic energy is a functional of the electron density: $\mathrm{E}[\rho]$. Hence, it depends only on the three spatial coordinates of the one-electron density (independent of the number of electrons in the system). This is a significant formal simplification compared with wave function methods that depend on three spatial coordinates and one spin coordinate per electron. The total energy $\mathrm{E}[\rho]$ is given by

$$E[\rho] = T[\rho] + E_{ne}[\rho] + E_{ee}[\rho] \tag{2.5}$$

where $\mathrm{T}[\rho]$, $\mathrm{E}_{ne}[\rho]$, and $\mathrm{E}_{ee}[\rho]$ represent the kinetic energy of the electrons, the nuclei-electron interactions, and the electron-electron interactions, respectively. Exactly known are the functional $\mathrm{E}_{ne}[\rho]$ and the classical Coulomb part of $\mathrm{E}_{ee}[\rho]$, whereas the exact form of the kinetic energy functional $\mathrm{T}[\rho]$ and of the exchange-correlation part of $\mathrm{E}_{ee}[\rho]$ are unknown. Kohn and Sham presented in 1965 a formalism, in which the kinetic energy term is split into two parts, namely an exactly known term for non-interacting electrons and an unknown correction term accounting for the electron-electron interactions.[38] The latter is commonly included in the so-called exchange-correlation term E^{XC} that represents the two-electron exchange and correlation interactions and the kinetic energy corrections.

Over the past decades, DFT development has focused on generating ever more accurate and refined exchange-correlation functionals. The simplest local density approximation (LDA) expresses these functionals in terms of the density of a uniform electron gas, which may be appropriate for solids but not for molecules. The introduction of the generalized gradient approximation (GGA) and of hybrid functionals in the 1980s and early 1990s triggered the widespread use of DFT in computational chemistry. In GGA functionals the energy depends on the (local) electron density and on its first derivative.[39, 40] The parameters in such functionals are either fitted numerically to experimental data or are adopted to satisfy general principles from wavefunction theory. Hybrid functionals additionally take into account a fraction of (exact) HF exchange. The most commonly used hybrid functional is B3LYP,[41] where the fraction of exact exchange included has been determined by fitting against experimental data. There are many other (at least partially semi-empirical) density functionals that may be more or less accurate for specific types of application, so careful validation is always recommended in DFT studies.

Weak interactions such as dispersion (*i.e.* the attractive part of van der Waals interactions) are formally not included in standard DFT functionals. The simplest way of accounting for dispersion in such cases is to include empirical dispersion interactions:[42] the dispersion energy is computed as a sum over empirical atom-pair terms (involving atom-specific dispersion coefficients) and then added to the DFT energy. In this thesis the DFT-D3 approach was applied.[43] Finally, it should be noted that electronically excited states can be studied using time-dependent density functional theory (TD-DFT).[44, 45]

2.3 Solvation Models

There are implicit and explicit solvation models to model the solvent environment. Implicit models do not treat the solvent molecules individually, instead they attempt to account for solvation effects such as polarization and dipole orientation in an overall manner. Explicit models take solvent molecules into account explicitly; this is a more realistic but also more costly description. A compromise is to treat explicitly only the solvent molecules close to the solute (*e.g.* the first solvation shell) and to account for bulk solvent effects implicitly.

Implicit solvation methods such as the polarizable continuum model (PCM) describe the solvent as a uniform polarizable medium with a fixed dielectric constant.[46] The solute molecule is placed in a cavity within the reaction field.

The variants of these methods vary with regard to size and shape of the cavity and how the interactions between solute and solvent are treated. In PCM the cavity is defined by the empirically scaled sum of the van der Waals radii of the atoms of the solute, the solvent-solute interactions are parameterized as a function of the surface area of the solute, and electrostatic interactions are evaluated using the electrostatic potential generated from a point charge field.

Explicit solvation methods often utilize a hybrid quantum mechanics/molecular mechanics (QM/MM) approach.[47,48] Here the solute is treated at an appropriate quantum-chemical level (*e.g.* DFT or semi-empirical) while the surrounding solvent molecules are described by force field methods (molecular mechanics, MM). This allows for an atomistic modeling of specific solute-solvent interactions such as hydrogen bonds and of specific shell structures in the surrounding of the solute. QM/MM aproaches require a realistic modeling of the interactions between the QM part and the surrounding MM part (bonding and non-bonding interactions). Electrostatic QM/MM interactions are commonly treated by electrostatic embedding,[49] *i.e.* the point charges in the MM region are included as additional one-electron terms in the QM Hamiltonian, while the van der Waals interactions are dealt with at the MM level. Bonding interactions between the QM and MM parts usually do not exist because of the absence of covalent bonds between the QM region (solute) and the MM region (solvent molecules).

Chapter 3

Results and Discussion

The main findings of the studies on nonadiabatic dynamics, structures, and reaction mechanisms studied are summarized in this chapter. Detailed discussions can be found in the attached publications (Appendix A to E).

3.1 Studying nonadiabatic decay dynamics of 9*H*-Guanine in water

9*H*-guanine (GUA) as shown in Figure 3.1 was studied in aqueous solution using the semi-empirical OM2/MRCI method in the framework of QM/MM computations, which employed the ChemShell package[50, 51] for combining the MNDO99 semi-empirical code[52] for the quantum part and the TIP3P force field[53] for the molecular mechanics treatment of the solvent. The two regions were linked together via electronic embedding. The geometries of the ground state, the first and second excited state, and the relevant conical intersections were optimized, and vertical excitation energies were computed for validating the chosen semi-empirical method by comparisons to higher-level computations and experiments and for studying solvent effects. Nonadiabatic dynamics simulations were started from the first and second excited state and were run for 6000 time steps of 0.2 fs. To allow for surface hopping during the dynamics, the Tully fewest-switches algorithm was employed.[36] To assess the reliability of the computed decay dynamics, the ionization potential along the trajectories was computed based on Koopmans' theorem and compared to the experimentally measured ionisation potential of guanosine in water during deexcitation. Details on the computational procedures and further detailed results are given in Appendices A and B.

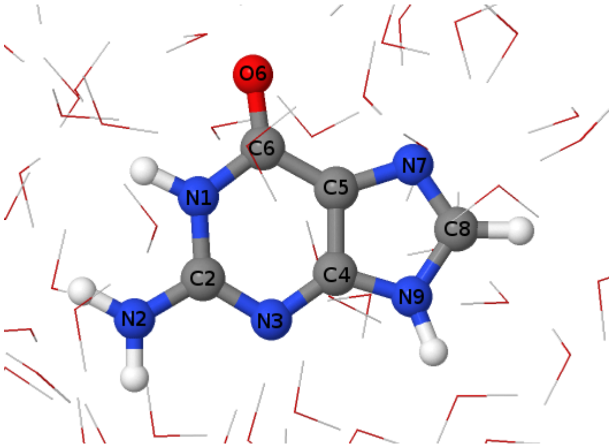

Figure 3.1: Representative optimized geometry of the ground state of solvated GUA (with atom labels).

Potential energy surfaces

The optimized structure of the ground-state minimum $(S_0)_{min}$ of GUA is planar with a slight pyramidalization of the amino group, in agreement with previous gas-phase and solvated GUA models. As the total energy of a QM/MM system is not only dependent on the geometry of solute in the QM part but also on the arrangement of the surrounding solvent molecules, a number of snapshots taken from a ground-state MD run were chosen for geometry optimization. Starting from ten optimized ground-state structures the system was then optimized in the first and second excited state. The optimizations of the first excited state led to two distinct $(S_1)_{min}$ geometries as shown in Figure 3.2, while those of the second excited state (S_2) led to a conical intersection or did not converge. In one of the $(S_1)_{min}$ structures the rings remain planar (as in $(S_0)_{min}$) but the carbonyl oxygen O6 is moved out of the molecular plane ($S_{1\alpha}$, see Figure 3.2 a). The other $(S_1)_{min}$ structure shows a distinct distortion of the molecular plane, best described as a boat-like conformation of the six-membered ring ($S_{1\beta}$, see Figure 3.2 b). These two types of $(S_1)_{min}$ structures are often found in similar systems. Previous gas-phase optimizations had only reported the $S_{1\beta}$ minimum structure, but re-optimizing the $S_{1\alpha}$ structures without solvent retained the out-of-plane position of the carbonyl oxygen. Thus, $S_{1\alpha}$ exists both in the gas phase and in solution, lying close to a conical intersection of similar geometry (see below).

The search for optimized geometries at conical intersections between the S_0 and S_1 states (*i.e.* CI_{01}) was started from corresponding hopping structures obtained from nonadiabatic decay dynamics simulations. Three different geometries for CI_{01} were found: $CI_{01\alpha}$ structures are characterized by a boat-like

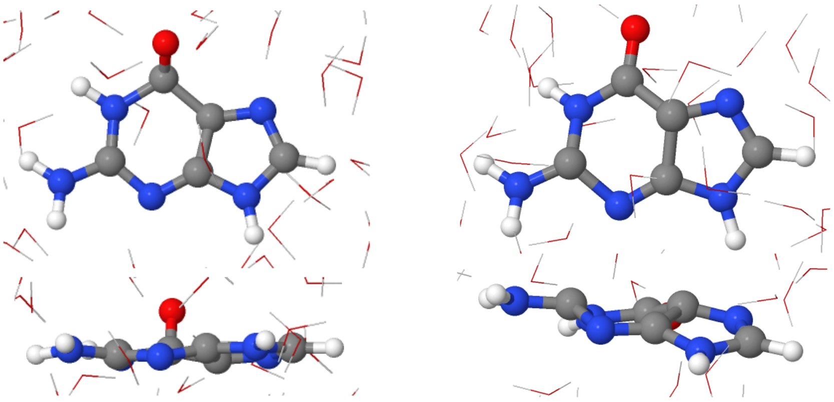
(a) $S_{1\alpha}$ (b) $S_{1\beta}$

Figure 3.2: Representative optimized geometries of the $S_{1\alpha}$ minimum (a) and the $S_{1\beta}$ minimum (b).

distortion of the six-membered ring. $CI_{01\beta}$ structures feature a strong out-of-plane motion of the amino group. $CI_{01\gamma}$ structures show a strong out-of-plane motion of the carbonyl oxygen. The out-of-plane motion of either the amino group or the carbonyl oxygen may be up or down relative to the molecular plane. Representative examples for these three structures are given in Figure 3.3. These three types of CI_{01} are consistent with previous gas-phase studies both at the OM2/MRCI level[54] and the *ab initio* MRCIS level.[55,56]

Geometries of the conical intersection between the S_1 and S_2 states (CI_{12}) were optimized starting either from corresponding hopping structures (as in the CI_{01} case) or from $(S_0)_{min}$ when trying to optimize the S_2 state. The computed CI_{12} structures are characterized by slight distortions of the six-membered ring partly accompanied by a moderate out-of-plane motion of the amino group. One example is given in Figure 3.4.

At the ground-state minima of the different snapshots the computed vertical excitation energies of the first two singlet excited states are typically in the range of 4.40–4.53 eV and 4.74–4.82 eV, respectively. They are in the same range as the excitation energies computed with similar QM(DFT/MRCI)/MM setups using large basis sets (average values: 4.42 and 4.98 eV, respectively, with standard deviations of 0.14-0.16 eV).[57] They are close to the experimental maxima of the first bands at 4.51 and 5.04 eV.[58] The first two singlet excited states are bright L_a and L_b $\pi\pi^*$ states, as also reported in various computational and experimental studies.[54,57–60] Gas-phase OM2/MRCI computation assign these states accordingly but with slightly shifted excitation energies (L_a blue shifted in solution by around 0.2 eV, L_b red shifted in solution by around 0.2 eV).[54]

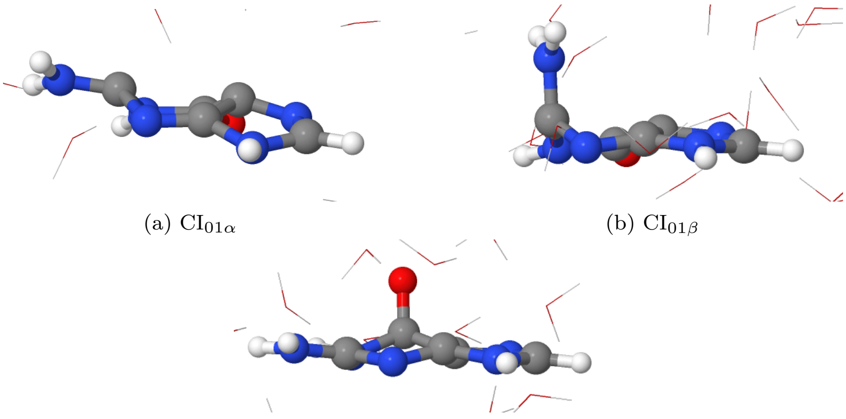

(a) $\mathrm{CI}_{01\alpha}$ (b) $\mathrm{CI}_{01\beta}$

(c) $\mathrm{CI}_{01\gamma}$

Figure 3.3: Representative optimized geometries for the three types of conical intersections connecting the ground and the first excited state (CI_{01}).

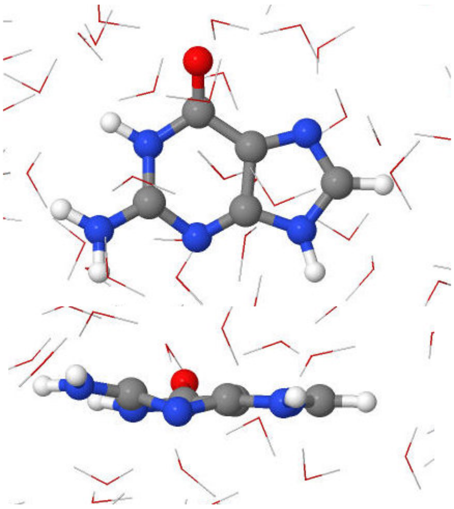

Figure 3.4: Representative optimized geometry of the conical intersection between the first and second excited state (CI_{12}).

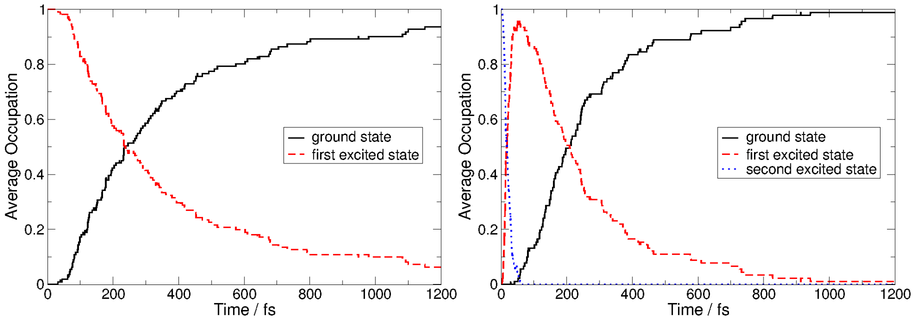

(a) Set A (b) Set B

Figure 3.5: Occupation of the low-lying adiabatic states after initial excitation to the S_1 state (set A) and the S_2 state (set B) as a function of simulation time.

The gap between S_1 and S_2 is thus reduced in solution but still sizeable. At the $(S_1)_{min}$ geometries, the S_1 state is still a $\pi\pi^*$ state, whereas the S_2 state is of mixed character (with $n\pi^*$ and $\pi\pi^*$ contributions).

Nonadiabatic dynamics

The starting configurations for the surface hopping runs were snapshots from a ground-state MD run chosen such that their excitation yields overall a theoretical absorption spectrum reasonably close to the experimental spectrum. Two sets of surface hopping dynamics runs were performed. The 122 (100) snapshots of set A (B) were excited to the first (second) excited state. For technical reasons some of the surface hopping runs terminated unsuccessfully before a hop occurred. Therefore, only 97 (84) trajectories could be analyzed for set A (B). In both sets ultrafast internal conversion to the ground state was found. The average occupations of the respective states over time are shown in Figure 3.5.

For the nonadiabatic dynamics starting from the S_1 state (set A), the deexcitation can be described as an exponential decay:

$$f(t) = f_0 + (1 - f_0)e^{-\frac{t-t_0}{\tau}} \tag{3.1}$$

where f_0 is the fraction of the population remaining in the S_1 state at the end of the simulation, t_0 is the time when the exponential decay sets in, and τ is the corresponding decay constant. The fitting results in $t_0 = 37$ fs and $\tau = 277$ fs. Hence the lifetime of the S_1 state is 314 fs (the sum of t_0 and τ). After 1.2 ps there is still a fraction of about 6 % remaining in the S_1 state.

For the nonadiabatic dynamics starting from the S_2 state (set B), the two subsequent decays can be described by

$$f(t) \propto \frac{\tau_2}{\tau_1 - \tau_2}(e^{-\frac{t}{\tau_1}} - e^{-\frac{t}{\tau_2}}) \tag{3.2}$$

where τ_1 and τ_2 refer to the decay constants for the deexcitation from S_2 to S_1 and from S_1 to S_0, respectively. The fitting yields $\tau_1 = 20$ fs and $\tau_2 = 248$ fs. The decay from the S_2 state is completed within 60 fs, and after 1.2 ps only 1 % of the population remains in the S_1 state.

The overall deexcitation to the ground state is obviously slightly faster when starting from the S_2 rather than the S_1 state. This can be attributed to the higher initial energy that is available after excitation to the S_2 state, which results in faster nuclear motion and allows the molecule to reach the S_0–S_1 conical intersection more quickly. In addition, the higher nuclear velocity enhances the nonadiabatic coupling term (the dot product between the nonadiabatic coupling vector and the nuclear velocity vector) and thus leads to a higher hopping probability for the nonadiabatic $S_1 \rightarrow S_0$ transition.

The average $S_2 \rightarrow S_1$ hopping time is computed to be 21 fs. The geometries at the hopping event are almost planar with slight distortions of the ring system, sometimes in a boat-like conformation or with a slight out-of-plane motion of the amino group and/or the carbonyl oxygen. Five of these hopping structures were selected for geometry optimization on the S_2 PES, which yielded CI_{12} geometries quite similar to the initial hopping structures.

Regardless of whether the nonadiabatic dynamics were started in the S_1 or S_2 state (sets A and B), four groups of hopping structures were found for the $S_1 \rightarrow S_0$ internal conversion. The characteristic features of these four groups are (a) the distortion of the six-membered ring in a boat-like manner, (b) the out-of-plane motion of the amino group, (c) the out-of-plane displacement of the carbonyl oxygen, and (d) the overall distortion of the aromatic ring system. One representative example of each group is displayed in Figure 3.6. The corresponding average hopping times are given in Table 3.1 for both sets separately.

Around a dozen hopping structures of each group from set A (in total 50) were chosen as input for CI_{01} geometry optimization. More than half of these (28) converged to a conical intersection structure. As already mentioned above, three types of minimum-energy conical intersections were found in this manner for GUA in water (see Figure 3.3). When starting from hopping structures with a distorted boat-like six-membered ring, the optimization either failed or reached $CI_{01\alpha}$. Optimizations of hopping structures with an out-of-plane amino group or carbonyl oxygen most often succeeded and arrived at the corresponding conical intersection, *i.e.,* $CI_{01\beta}$ or $CI_{01\gamma}$, respectively. Optimizations of hopping structures from the last group (with distorted rings) mostly crashed or led to

Table 3.1: Characteristics and occurrence of different types of $S_1 \rightarrow S_0$ hopping structures for GUA in water

	Set A		Set B	
Characteristics	occ.	av. hopping time / fs	occ.	av. hopping time / fs
boatlike ($CI_{01\alpha}$)	26	343	8	395
NH_2 oop ($CI_{01\beta}$)	13	441	6	517
O oop ($CI_{01\gamma}$)	41	265	60	216
distortion of rings	17	224	10	140

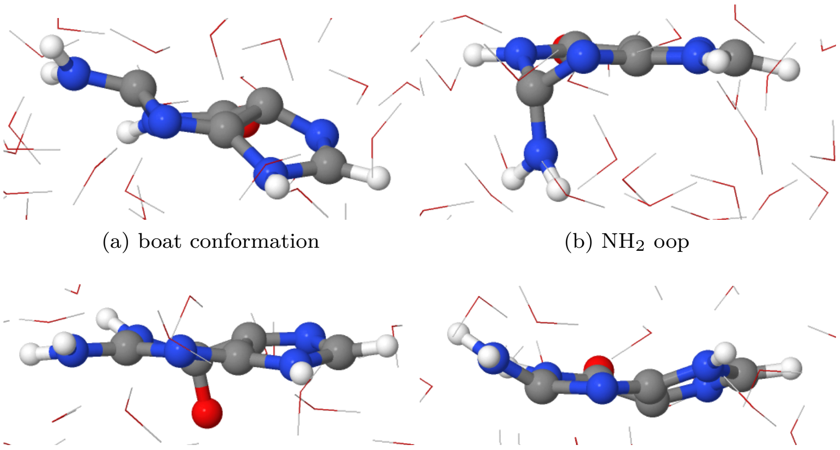
(a) boat conformation

(b) NH_2 oop

(c) O oop

(d) plane distorted

Figure 3.6: Representative examples for the four groups of $S_1 \rightarrow S_0$ hopping structures for GUA in water.

Table 3.2: Norm of the S_1 gradient components perpendicular to the molecular plane at atoms O6 and N2, respectively, for GUA in the gas phase and in aqueous solution, given in kcal/(mol Å).

gradient at	gas phase	aqueous solution
N2	6.77	7.47
O6	5.00	10.25

$CI_{01\gamma}$, *i.e.* no fourth type of conical intersection geometry could be identified in this manner.

Compared to the nonadiabatic dynamics of GUA in the gas phase at the same OM2/MRCI level, the internal conversion is slightly faster in aqueous solution: for the two decay pathways identified in the gas phase the average hopping times are 190 fs through $CI_{01\alpha}$ and 400 fs through $CI_{01\beta}$. But more remarkably than the slight speed-up of decay is the fact that the water environment modifies the preferences among the decay pathways. First of all, the decay via $CI_{01\gamma}$ is only found in aqueous solution. Secondly, it even becomes the main decay pathway in solution whereas the decay via $CI_{01\alpha}$ or $CI_{01\beta}$ dominates in the gas phase. These different preferences probably originate from changes in the S_1 gradient at the N2 atom and more importantly at the O6 atom. The norms of the respective S_1 gradients are given in Table 3.2. As can be seen, the S_1 gradient norm is on average increased only slightly at N2 but approximately doubled at O6 in solution. This may explain not only the preference to decay via $CI_{01\gamma}$ but also the slightly faster decay in solution.

These findings might be related to possible hydrogen-bonding interactions in solution, especially between the carbonyl oxygen O6 and surrounding water molecules. However, an analysis of the shortest O6-H distances along the trajectories and at the hopping geometries did not provide firm quantitative evidence in support of this explanation.

Comparison with experiment

Experimental studies on GUA in aqueous solution are scarce, probably at least partly due to the low solubility of GUA in water. Guanosine (GUO), the nucleoside of GUA with a sugar substituent at N9, is more soluble and thus easier to study experimentally. Recently, Lübcke and co-workers investigated the decay of GUO in aqueous solution by ultrafast time-resolved photoelectron spectroscopy. Pump-probe experiments were performed using UV pulses of 4.66 eV and 5.2 eV (for experimental details please see Appendix B). As GUO absorbs at both energies, the decay dynamics can be observed for excitation

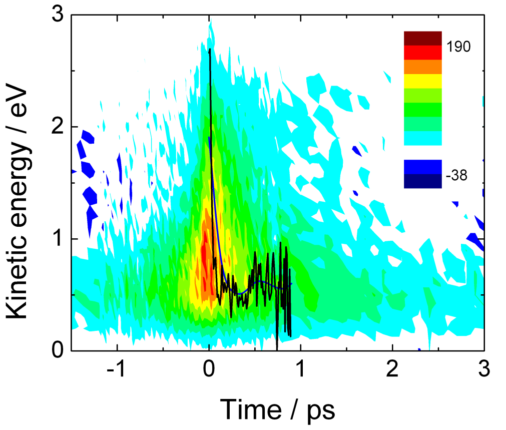

Figure 3.7: Time-resolved photoelectron spectra of GUO: computed kinetic energy (black line, shifted) and experimental kinetic energy (blue line, folded), see text.

at 4.66 eV (positive delay, $t > 0$) and 5.2 eV (negative delay, $t < 0$). The measured kinetic energies as function of delay time are shown in Figure 3.7. These measurements yield an S_1 lifetime of GUO in the ps range, much longer than the computed lifetime of GUA in water (around 310 fs). This difference may be due to the different substituents at N9 (sugar and hydrogen, respectively).

For comparison with the experimental data, the ionization potential (IP) of GUA was calculated along the computed trajectories in steps of 10 fs, on the basis of Koopmans' theorem (*i.e.* neglecting orbital relaxation and correlation effects). In Figure 3.8 the evolution of the IP over time is shown, with the time t=0 corresponding to the initial photoexcitation. For the 47 trajectories directly excited to the S_1 state, the IP was computed every 10 fs starting at t=0. For the 83 trajectories initially excited to the S_2 state, the IP was calculated only after the system had relaxed to the S_1 state (after ca. 30 fs on average). This is reflected in the evolution of the number of trajectories in the S_1 state (red line, indicated at the right-hand y-axis, measure of the intensity). This number rises steeply within the first 50 fs, because the 83 trajectories initially excited to the S_2 state populate the S_1 state (ultrafast internal conversion). The average IP of the S_1 state quickly rises from an initial value of ca. 3-4 eV to a value in the range of 5-6 eV, typically within 50 fs. For calibration, the computed IP of the first excited state of GUA in water was compared with the corresponding experimental value for GUO in water. The latter is the difference between the IP of GUO in the ground state and in the first excited state: $IP_{exp} = 2.55$ eV. The IP of GUA in the first excited state is obtained as the average value (Koopmans'

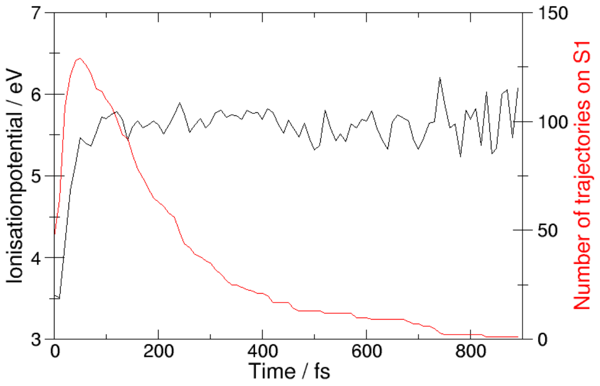

Figure 3.8: Time evolution of the computed IPs of the S_1 state (black line, average over trajectories) and of the occupation of the S_1 state (red line).

theorem) of the corresponding 47 trajectories at time t=0: $IP_{comput} = 3.54$ eV. For a direct comparison between experiment and theory for GUO at later times, the computed energies of GUA are thus shifted by -1 eV.

The ionization potential is related to the kinetic energy E_{kin} measured by photoelectron spectroscopy via

$$E_{kin} = E_{photon} - IP \tag{3.3}$$

where E_{photon} is the energy of the UV pulse. The calculated kinetic energy (black line) is plotted along with the measured kinetic energy in Figure 3.7. Due to limited time resolution the experimental values are folded using a Gauss function (blue line) to smoothen the curve. The time evolution of the calculated kinetic energies along the trajectories fits the experimental data fairly well (Figure 3.7). However, the computed differences in the kinetic energies along the distinct decay pathways are too small to be resolved experimentally.

Conclusion

In summary, the chosen QM/MM setup with the semi-empirical OM2/MRCI method as QM component is well suited to investigate the potential energy surfaces and nonadiabatic decay dynamics of 9*H*-guanine in water. The results are in reasonable agreement with the available experimental and *ab initio* findings. The effect of the solvent environment on the geometries of GUA at the excited-state minima and conical intersections is small, while the computed vertical excitations energies are significantly shifted in solution. The nonadiabatic decay of GUA is computed to be somewhat faster in aqueous solution than in the gas phase, and more importantly, the main decay pathway changes: while in the gas phase the decay mainly proceeds via the conical intersections $\mathrm{CI}_{01\alpha}$ and $\mathrm{CI}_{01\beta}$, these two play only a minor role in solution where the dominant decay channel goes through $\mathrm{CI}_{01\gamma}$. The time evolution of the computed excited-state ionization potentials along the trajectories of GUA in water compares reasonably well with corresponding experimental data for GUO in water obtained from ultrafast photoelectron spectroscopy.

3.2 Examining the nature of bonding in gold carbenoids

DFT was used to study the bonding situation in bimetallic gold-chromium carbenoids synthesized by Fürstner and co-workers.[12] Experimental data from X-ray crystallography and NMR spectroscopy were available but not sufficient to clarify the bonding situation. To shed light on the bonding especially with regard to the metal-carbon interactions, several approaches were used to characterize the bonding in these systems: natural bond orbital (NBO) analysis, fragment analysis, atoms-in-molecules (AIM) analysis, and comparison of dissociation energies.

The optimized geometries of the two complexes **2-1** and **2-2** under investigation are shown in Figures 3.9 and 3.10, respectively. Optimizations were started from the X-ray crystal structure employing the BP86 functional[39, 61] and the def2-TZVP basis set[62] and including Grimme dispersion interactions (D3).[43] The gold atom was described using the def2-ECP basis set and applying an effective core potential for the 60 inner-shell core electrons.[63] The computations were mainly performed with Turbomole,[64] in some cases also with Gaussian09[65] and ADF.[66] For more details regarding the computational methods and results please see the Supporting Information in Appendix C.

The optimized geometries are in good agreement with experiment as can be seen from the comparison of selected calculated and experimental bond lengths given in Table 3.3. Additionally, the quality of the optimized structure of **2-2** was evaluated by comparing measured and computed NMR chemical shifts. Experimentally, NMR chemical shifts were measured for C_{ipso} and $\mathrm{C'}_{ipso}$ (for atom numbering please see Figure 3.11). The chemical shifts were calculated with several DFT-based procedures (using different density functionals and basis sets, without and with inclusion of relativistic effects). The NMR chemical shifts δ are obtained from the computed isotropic shielding constants σ via:

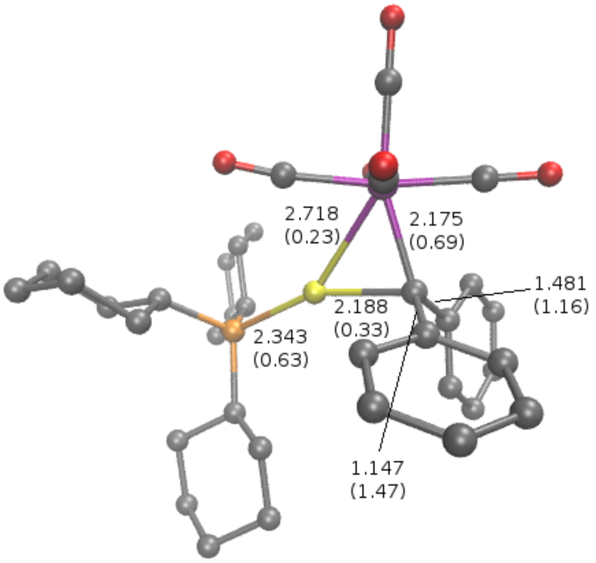

Figure 3.9: Optimized geometry of complex **2-1** at RI-BP86/def2-TZVP+D3 level. The hydrogen atoms are omitted for clarity (color code: black=carbon, violet=chromium, yellow=gold, red=oxygen, orange=phosphorus). Selected bond lengths (Å) and Wiberg bond indices (in parentheses) are also given.

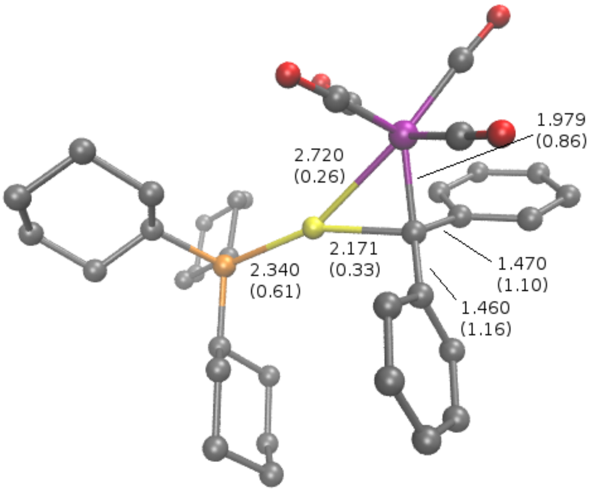

Figure 3.10: Optimized geometry of complex **2-2** at RI-BP86/def2-TZVP+D3 level. The hydrogen atoms are omitted for clarity (color code: black=carbon, violet=chromium, yellow=gold, red=oxygen, orange=phosphorus). Selected bond lengths (Å) and Wiberg bond indices (in parentheses) are also given.

$$\delta = \delta_{ref} + \sigma_{ref} - \sigma \tag{3.4}$$

where δ_{ref} and σ_{ref} are the chemical shift and isotropic shielding constant of a reference compound. As in the experimental work, dichloromethane was chosen as reference. The reference values σ_{ref} were computed at the same level as σ, and δ_{ref} was taken from experiment. The experimental chemical shifts were well reproduced when using the recommended functional B3LYP, a large basis set and including relativistic effects. Thus, the electronic structure obtained from the DFT calculations is consistent with the experimental NMR data.

Concerning the bonding situation, answers were sought to the following questions:

- Do the gold-chromium complexes contain a true carbene?
- Is there a direct metal-metal bond?

Natural bond orbital analysis - Wiberg bond indices

The natural bond orbital analysis package (NBO) allows the computation of Wiberg bond indices (WBI).[67] The computed WBI for the central bonds are given in Figures 3.9 and 3.10 for complexes **2-1** and **2-2**, respectively. In both cases the bonding between the gold atom and the chromium atom or the carbene carbon C1 is quite weak (WBI of around 0.2 to 0.3), whereas the bonding between Cr and C1 is considerably stronger (WBI of 0.7 and almost 0.9, respectively).

Fragment analysis

The basic concept behind fragment molecular orbital analysis is to build a molecule from user-defined fragments. For each of these fragments the fragment

Table 3.3: Selected bond lengths in complex **2-2** [experimental (X-ray structure) vs. calculated (RI-BP86/def2-TZVP+D3)].

bond	bond length / Å experimental	bond length / Å calculated
Au-P	2.331	2.340
Au-C1	2.136	2.171
Au-Cr	2.718	2.720
C1-Cr	1.993	1.979
C1-C_{ipso}	1.469	1.470
C1-C'_{ipso}	1.476	1.460
Cr-C_{ipso}	2.272	2.330

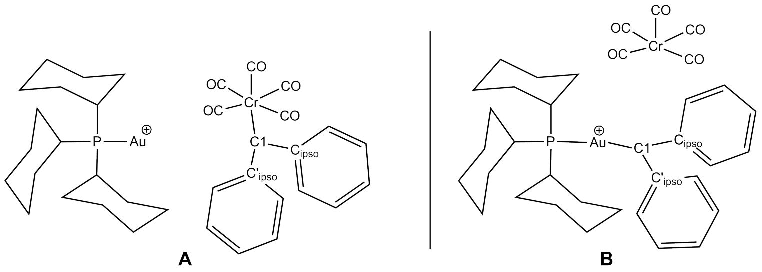

Figure 3.11: Representation of the two fragmentation schemes adopted for complex **2-1**.

orbitals (FOs) are calculated starting from atomic orbitals (AOs). These FOs are used as new basis functions to recompute the molecular orbitals (MOs) of the full complexes.[66] We have adopted two different fragment analysis schemes for complexes **2-1** and **2-2**. In the first one (fragmentation A), the complex after full geometry optimization is divided into a $[P(Cy)_3Au]^+$ fragment and a $[C(Ph)_2Cr(CO)_n]$ fragment. In the second scheme (fragmentation B), the complex is divided into a $[Cr(CO)_n]$ fragment and a $[C(Ph)_2P(Cy)_3Au]^+$ fragment (*cf.* Figure 3.11). MOs are generated for each of these fragments, and the total electronic structure is then recomputed based on the fragment orbitals. In this way it is possible to determine the contributions of the fragment orbitals to the MOs of the corresponding complex.

Fragmentation A

First of all, the findings with regard to the fragmentation of complexes **2-1** and **2-2** are very similar. The relevant FOs for the following analysis are selected by the criterion that the population of the FO has to change by at least ±0.1 electrons upon recombination. The lowest unoccupied molecular orbital (LUMO) of the gold fragment, which has a large contribution from the 6s atomic orbital of the metal atom ($\%s_{Au}$=44, illustrated in Figure 3.12), receives 0.51 and 0.45 electrons in case of complex **2-1** and **2-2**, respectively. The charge is donated mainly from the HOMO-1 of the $[C(Ph)_2Cr(CO)_5]$ fragment in case of complex **2-1** (0.3 electrons lost), and from the HOMO and HOMO-1 of the $[C(Ph)_2Cr(CO)_4]$ fragment in case of complex **2-2** (loss of 0.15 to 0.18 electrons each). The main contributions from FOs (single contribution larger than 0.1) to the orbitals LUMO to HOMO-3 are given in Table 3.4 for both complexes. Please note that the MOs resulting from the interaction of fragment orbitals have large contributions from the $[C(Ph)_2Cr(CO)_5]$ fragment. In case of complex **2-1**, HOMO-1 and HOMO-3 of the $[C(Ph)_2Cr(CO)_5]$ fragment contribute 48 % and

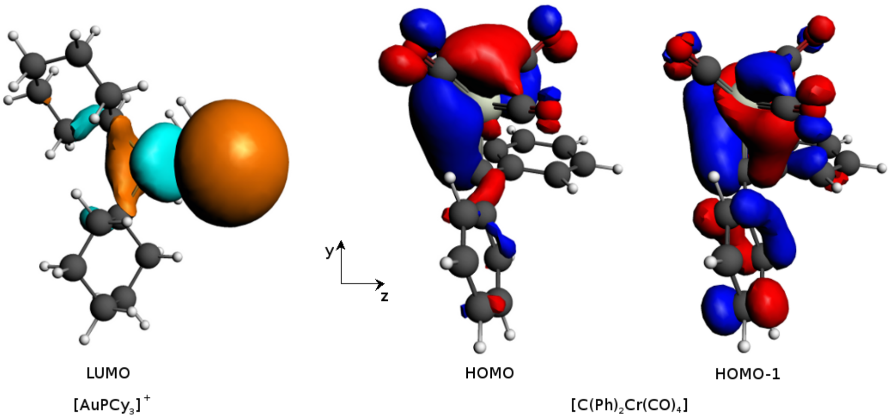

Figure 3.12: Shape of selected fragment orbitals (fragmentation A) of complex **2-2** at BP86/TZP(ZORA) level. The local axis frame chosen for the analysis is also specified in the figure.

17 %, respectively, while there are only minor contributions from the HOMO-2 (8 %) and the LUMO (6 %) of the $[P(Cy)_3Au]^+$ fragment. In case of complex **2-2**, HOMO-1 and HOMO of the $[C(Ph)_2Cr(CO)_4]$ fragment contribute 43 % and 11 %, respectively, while there is only 7% contribution from the LUMO of the $[P(Cy)_3Au]^+$ fragment. Hence, as there is no strong orbital mixing between the $[P(Cy)_3Au]^+$ and $[C(Ph)_2Cr(CO)_n]$ fragments, the bonding situation can be described as a chromium-carbene complex with a weakly coordinating gold unit (η^2 binding mode).

Fragmentation B

Again, the analysis is focused on those FOs for which the population changes upon recombination by at least ±0.1 electrons. Selected FOs are shown graphically in Figures 3.13 and 3.14 for complexes **2-1** and **2-2**, respectively. The main findings with regard to the FOs are: The LUMO of fragment $[AuPCy_3C(Ph)_2]^+$ has large contributions from the $2p_z$ orbital of C1 (39 % and 44 % in complex **2-1** and **2-2**, respectively). Additionally, the LUMO+1 of this fragment has small contributions from the 2p orbital of both ipso carbon atoms (around 10 % each). In the case of complex **2-1**, the HOMO of the $[AuPCy_3C(Ph)_2]^+$ fragment has large contributions from the $2p_y$ orbital located at C1 (20 %) with a minor contribution from the $5d_{xz}$ orbital at Au (5 %). Correspondingly, for complex **2-2** the main contributions to the HOMO arise from a $2p_y$ orbital located at C1 (19 %) complemented by minor contributions from the 6s orbital located at Au (7 %). For both complexes, the HOMO-1 is mainly localized around Au, with main contributions from 6s (23-26 %) and 5d (14-19 %). In both complexes, this

Table 3.4: Contributions of fragment orbitals (fragmentation scheme A, contributions larger than 0.1) to molecular orbitals of both complexes, respectively.

MO of complex **2-1**	contributions from fragments
LUMO	0.86 LUMO $[C(Ph)_2Cr(CO)_5]$
HOMO	0.95 HOMO $[C(Ph)_2Cr(CO)_5]$
HOMO-1	0.48 HOMO-1, 0.17 HOMO-3 $[C(Ph)_2Cr(CO)_5]$
HOMO-2	0.86 HOMO-2 $[C(Ph)_2Cr(CO)_5]$
HOMO-3	0.61 HOMO-3, 0.11 HOMO-1 $[C(Ph)_2Cr(CO)_5]$
MO of complex **2-2**	contributions from fragments
LUMO	0.85 LUMO $[C(Ph)_2Cr(CO)_4]$
HOMO	0.66 HOMO, 0.27 HOMO-1 $[C(Ph)_2Cr(CO)_4]$
HOMO-1	0.87 HOMO-2 $[C(Ph)_2Cr(CO)_4]$
HOMO-2	0.47 HOMO-1, 0.11 HOMO $[C(Ph)_2Cr(CO)_4]$
HOMO-3	0.40 HOMO-2 $[AuPCy_3]^+$, 0.23 HOMO-3, 0.15 HOMO-6 $[C(Ph)_2Cr(CO)_4]$

fragment receives electrons from the HOMO of the $[Cr(CO)_n]$ fragment, and at the same time there is a considerable amount of back-donation to the LUMO of the latter fragment (up to 0.5 electrons). The resulting MOs have contributions from both fragments. The main contributions (larger than 0.1) of FOs to the orbitals LUMO up to HOMO-3 are listed in Table 3.5 for both complexes. In contrast to fragmentation A strong mixing is evident: For both complexes the mentioned orbitals are build from FOs from both fragments. *E.g.* the HOMO-1 of complex **2-1** has contributions from the HOMO of the $[Cr(CO)_5]$ fragment (39 %) and from the LUMO of the $[AuPCy_3C(Ph)_2]^+$ fragment (15 %). Similarly the HOMO-3 has main contributions from the HOMO of the $[AuPCy_3C(Ph)_2]^+$ fragment (65 %) and from the LUMO and the HOMO-1 of the chromium fragment (4 % each). For complex **2-2**, the LUMO has the following contributions from the respective FOs: 49 % from the LUMO of $[AuPCy_3C(Ph)_2]^+$ fragment, 24 % from the HOMO of the chromium fragment. The HOMO-2 has mainly contributions from the HOMO and HOMO-2 of $[Cr(CO)_4]$ (25 % and 24 %, respectively) and the LUMO+1 of $[AuPCy_3C(Ph)_2]^+$ (19 %). This clearly indicates σ-bonding/π-backbonding interactions between the chromium and carbene units in both complexes, which are also reflected in the electron transfers between these fragments mentioned before.

Dissociation energies

The energies E_{diss} required to separate the complexes **2-1** and **2-2** into the respective fragments are listed in Table 3.6 for fragmentation schemes A and B. The energy of the fragments was computed at the geometry that they adopt in

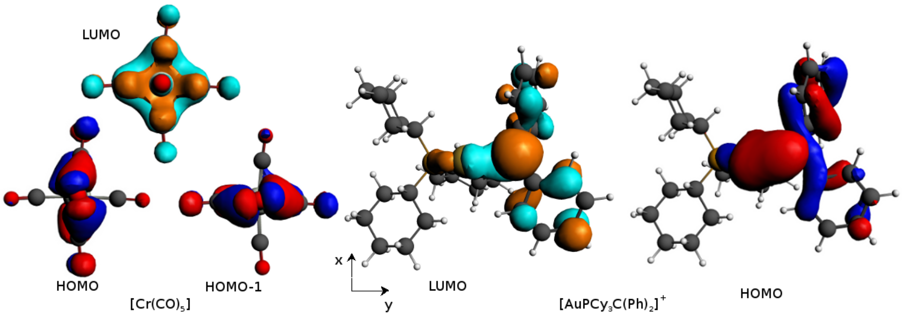

Figure 3.13: Shape of selected fragment orbitals (fragmentation B) of complex **2-1** at BP86/TZP(ZORA) level. The local axis frame chosen for the analysis is also specified in the figure.

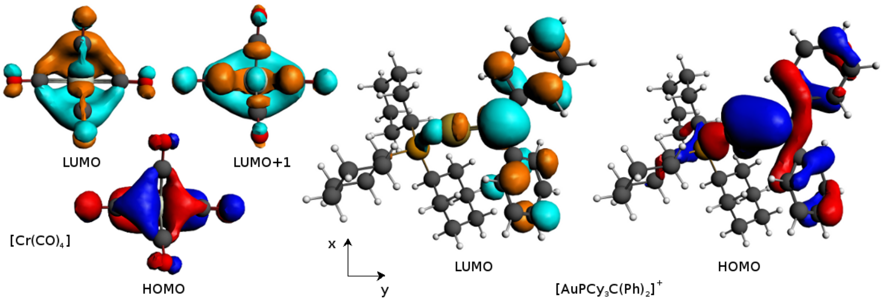

Figure 3.14: Shape of selected fragment orbitals (fragmentation scheme B) of complex **2-2** at BP86/TZP(ZORA) level. The local axis frame chosen for the analysis is also specified in the figure.

Table 3.5: Contributions of fragment orbitals (fragmentation B, contributions larger than 0.1) to molecular orbitals of both complexes.

MO of complex **2-1**	contributions from fragments
LUMO	0.64 LUMO $[AuPCy_3C(Ph)_2]^+$, 0.14 HOMO $[Cr(CO)_5]$
HOMO	0.75 HOMO-1, 0.12 HOMO $[Cr(CO)_5]$
HOMO-1	0.39 HOMO, 0.14 HOMO-2 $[Cr(CO)_5]$, 0.15 LUMO $[AuPCy_3C(Ph)_2]^+$
HOMO-2	0.76 HOMO-2 $[Cr(CO)_5]$
HOMO-3	0.65 HOMO $[AuPCy_3C(Ph)_2]^+$
MO of complex 2-2	**contributions from fragments**
LUMO	0.49 LUMO $[AuPCy_3C(Ph)_2]^+$, 0.24 HOMO $[Cr(CO)_4]$
HOMO	0.91 HOMO-1 $[Cr(CO)_4]$
HOMO-1	0.61 HOMO-2, 0.15 HOMO $[Cr(CO)_4]$
HOMO-2	0.25 HOMO, 0.24 HOMO-2 $[Cr(CO)_4]$, 0.19 LUMO $[AuPCy_3C(Ph)_2]^+$
HOMO-3	0.69 HOMO-1 $[AuPCy_3C(Ph)_2]^+$

Table 3.6: Dissociation energies of the complexes into frozen fragments (no relaxation) at BP86/TZP(ZORA) level in kcal/mol.

	E_{diss} fragmentation A	E_{diss} fragmentation B
complex **2-1**	42.44	39.09
complex **2-2**	49.44	63.76

the complex (no relaxation). For complex **2-1**, the computed energies are similar for fragmentation schemes A and B, while there are considerable differences in the case of complex **2-2**. The dissociation of the Cr-C1 bond (i.e., fragmentation B) into frozen fragments requires more energy than that of the Au-Cr/C1 bond. This implies a strong Cr-C1 bonding interaction in complex **2-2**.

AIM analysis

For further characterization of the bonding, a topological analysis of the electron density distribution was performed using the Atoms in Molecules (AIM) method.[68] This method identifies bonds between atoms through so-called bond critical points. These are saddle points of the electron density, where the gradient is zero in all directions while the second derivatives are positive along the bond and negative in the two other orthogonal directions. The resulting bond network

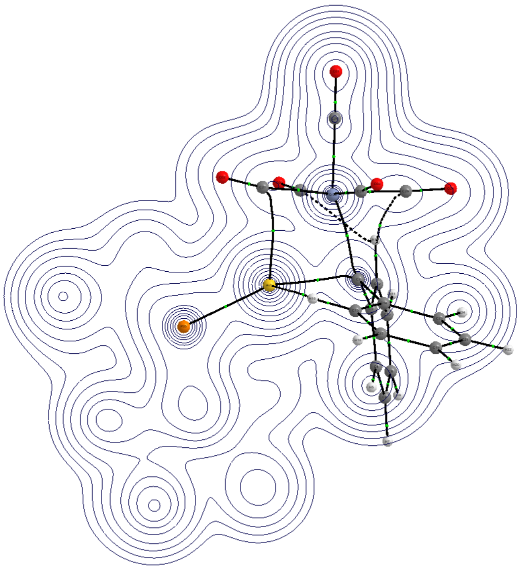

Figure 3.15: Graphical representation of bond critical points (green dots) and the electron density contour map in the plane Au, C1, Cr as obtained by the AIM method for complex **2-1**. The ligands at phosphorus are left out for clarity.

(with bond critical points indicated as green dots) and the associated density contour maps are shown in Figure 3.15 for complex **2-1** and in Figure 3.16 for complex **2-2**, respectively.

One should be cautious, however, not to over-interpret the AIM results. It is known that the AIM method may have difficulties to identify bridging bonding interactions. In the present case, the AIM analysis finds a bond critical point between Au and the carbene carbon atom C1 in both complexes (see Figures 3.15 and 3.16). There is no separate nearby bond critical point between Au and Cr, since the electron density distribution indicates only one bonding path that is directed more towards C1 than to Cr. Moreover, for complex **2-1** the AIM analysis provides an unexpected bond critical point between Au and a carbonyl group (see Figure 3.15). This is in contrast to the low NBO Wiberg bond index of 0.15 and the lack of a distinct orbital interaction in the fragment analysis.

Conclusion

In summary, the performed analyses indicate that the gold unit of the two complexes is only weakly bound to the chromium/carbene unit, so no pronounced metal-metal bond is detectable. Even though some electron density is transferred towards the gold unit, neither WBI nor any orbital mixing in the fragment analysis points to strong bonding. On the other hand, due to considerable σ

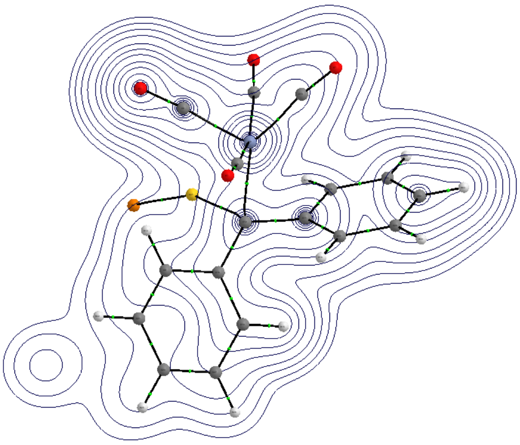

Figure 3.16: Graphical representation of bond critical points (green dots) and the electron density contour map in the plane C1, Cr, C_{ipso} as obtained by the AIM method for complex **2-2**. The ligands at phosphorus are left out for clarity.

donation and π backdonation the Cr-C1 bond can be characterized as a true carbene bond. Overall, the bonding in the gold-chromium carbenoid is thus best described as a chromium carbene carrying an η^2-bound gold unit.

3.3 Exploring the mechanism of an organocatalytic reaction

The reaction mechanism of the cyclization of the α,β-unsaturated hydrazone **3-1** catalyzed by a BINOL-derived phosphoric acid[14] (Figure 3.17) could not be clarified from experiment. Therefore DFT methods were used to elucidate the mechanism. The main question is whether the cyclization of the hydrazone **3-1** is pericyclic.

The DFT calculations focused on the cyclization step itself (highlighted in Figure 3.17). To reduce the computational effort, the bulky acid catalyst was replaced by a proton. In the final step of the study it was confirmed that the coordination of the conjugate base of the catalyst does not affect the reaction mechanism in a qualitative sense. The effective reaction under investigation is shown in Figure 3.18. Both the unprotonated hydrazone **3-1** and the protonated hydrazone **3-2** were considered to study the effect of acid catalysis. Additionally, the isoelectronic pure carbon analogue, pentadienyl anion **3-3**, was investigated as known reference for a pericyclic cyclization.

The computations were performed at the B3LYP/6-31G* level of theory[41, 69, 70] using the Gaussian09 program package.[65] Additionally, single-point calcula-

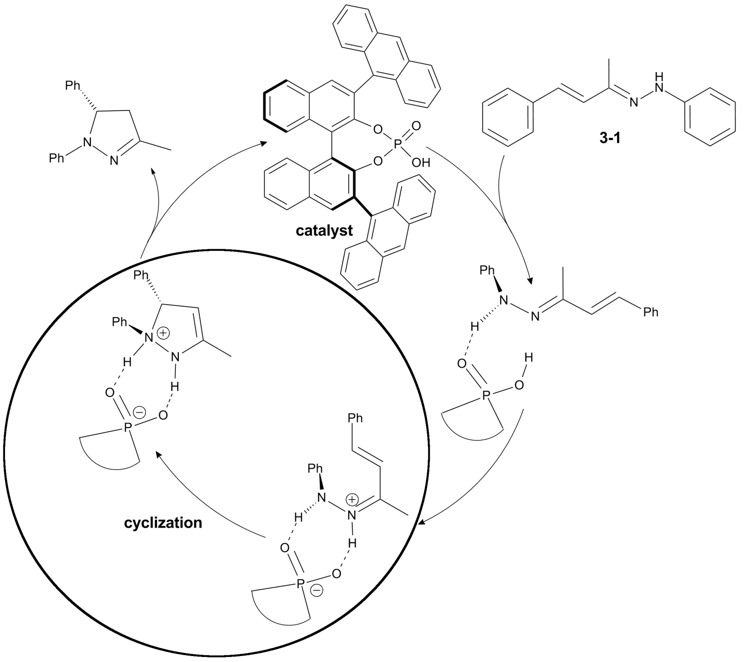

Figure 3.17: Catalytic cycle for the intramolecular ring closing reaction of the unsaturated hydrazone **3-1**; the cyclization step is highlighted.

tions were done including a larger basis set (6-311+G**), dispersion corrections, and solvent effects by PCM[46] (chlorobenzene). All energies reported here refer to these single-point calculations. For more details regarding computational methods and results please see Appendix D.

Cyclization - transition state search

Upon cyclization of **3-2**, two stereocenters are formed: one at N1 and one at C5 (cf. Figure 3.18). Therefore, the phenyl groups can be oriented either *cis* or *trans* to each other. In total four diastereomeric transition states are

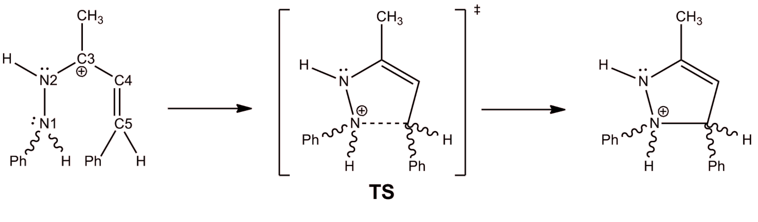

Figure 3.18: Reaction equation for the cyclization of **3-2** as investigated here.

Table 3.7: Relative free energies for the unprotonated hydrazone **3-1**, the protonated hydrazone **3-2** and the pentadienyl anion **3-3** given in kcal/mol (PCM/B3LYP-D/6-311+G**//B3LYP/6-31G*).

ΔG / kcal/mol	**3-1**	**3-2**	**3-3**
reactant	0	0	0
TS-*trans*	34.56	18.49	37.87
TS-*cis*	32.96	15.71	34.64
product-*trans*	6.09	10.80	23.08
product-*cis*	7.53	12.36	23.75

possible; transition states with the same relative configuration regarding the phenyl groups have the same reaction barrier as they are enantiomers. The same stereochemical findings are valid for the cyclization of **3-1**. As the pentadienyl anion **3-3** contains a mirror plane, there are only two relevant transition states that differ in the relative positions of the phenyl groups, *i.e.* either *cis* or *trans*. It should also be noted that the cyclization of **3-1** formally generates two charged groups in the molecule, and hence an additional proton shift from N1 to N2 is needed to obtain the final product. As this is a separate reaction step, the cyclizations of **3-1** and **3-2** are not as similar as those of **3-2** and **3-3**. The relative single-point free energies for the relevant minima and transition states of all three systems are given in Table 3.7.

First of all, it can be seen that acid catalysis reduces the activation barrier for the cyclization considerably as the barrier for **3-2** is around 16 kcal/mol lower than that for **3-1** (*cf.* columns 2 and 3 in Table 3.7). This agrees well with the experimental finding that adding an acid is necessary to run the reaction. The reaction barrier found for **3-3** seems unexpectedly high at first sight. However, the computed barriers published for various pericyclic reactions cover a broad range from 16 to 32 kcal/mol, depending on substituents and functional.[71] So the presently calculated barriers are high, but still close to the usual range.

Cyclization - electronic structure analysis

Pericyclic reactions are characterized by the existence of a closed-loop 6π molecular orbital at the transition state (TS).[72] DFT computations allow first of all to locate these TS but also to analyze further properties indicative of the existence of such an orbital at the TS. A related criterion is the aromatic character of the transition state (compared with reactants and products) which can be assessed by the Nucleus Independent Chemical Shift (NICS) analysis.[73] Moreover, pericyclic reactions are stereoselective, *i.e.* in the present case the orbitals at the terminal positions forming the new bond have to rotate in a concerted, disrotatory man-

Table 3.8: NBO analysis for the ring atoms in the reactant, the TS, and the product of the protonated hydrazone **3-2** and the pentadienyl anion **3-3**: NPA charges and occupation of lone pairs, if existent.

	atom	charge		occupation of lone pairs	
		3-2	**3-3**	**3-2**	**3-3**
reactant	N1/C1	-0.47	-0.34	1.86	
	N2/C2	-0.35	-0.20	1.57	
	C3	0.35	-0.17	0.80	1.18
	C4	-0.34	-0.20		
	C5	-0.04	-0.34		
TS-*trans*	N1/C1	-0.37	-0.26	1.63	
	N2/C2	-0.45	-0.42	1.80	
	C3	0.25	-0.05		
	C4	-0.37	-0.40		1.29
	C5	0.02	-0.27	0.69	
TS-*cis*	N1/C1	-0.35	-0.26	1.58	
	N2/C2	-0.44	-0.43	1.81	
	C3	0.22	-0.05		
	C4	-0.36	-0.43		
	C5	-0.01	-0.26	0.72	
product-*trans*	N1/C1	-0.29	-0.25		
	N2/C2	-0.46	-0.51	1.89	
	C3	0.17	-0.03		
	C4	-0.31	-0.50		1.40
	C5	-0.05	-0.25		
product-*cis*	N1/C1	-0.29	-0.25		
	N2/C2	-0.46	-0.46	1.88	
	C3	0.18	-0.04		
	C4	-0.32	-0.53		1.41
	C5	-0.05	-0.25		

ner to be symmetrically allowed to overlap. On the contrary, pseudopericyclic reactions are always allowed; their TS geometry is typically close to planarity and the 6π orbital has at least one orbital disconnection, therefore, aromaticity is not increased at the TS. Usually reaction barriers are very small in the case of pseudopericyclic reactions.[74]

To gain detailed insight into the electronic structure of all relevant stationary points, NBO analyses were performed with focus on charges, bonding, and the occupation of lone pairs and π orbitals. The results are summarized in Tables 3.8 and 3.9, respectively.

Let us first consider the reactants. Upon protonation of the hydrazone, the substituents at N1 of the reactant are rotated out of the molecular plane to an almost perpendicular position in **3-2**; the positive charge leads to an increase in

Table 3.9: NBO analysis with regard to the bonds in the ring for the reactant, the TS, and the product of the protonated hydrazone **3-2** and the pentadienyl anion **3-3**: bond lengths in Å, Wiberg bond orders (BO) and occupations of π bond orbitals, if existent.

	bond	bond length /Å		BO		occupation of π bond orbitals	
		3-2	**3-3**	**3-2**	**3-3**	**3-2**	**3-3**
reactant	N1-N2/C1-C2	1.40	1.39	1.02	1.50		1.80
	N2-C3/C2-C3	1.33	1.42	1.40	1.34		
	C3-C4	1.42	1.42	1.28	1.33		
	C4-C5	1.37	1.39	1.55	1.50	1.72	1.80
	C5-N1/C5-C1	2.99	3.30	0.02	0.04		
TS-*trans*	N1-N2/C1-C2	1.41	1.46	1.02	1.20		
	N2-C3/C2-C3	1.40	1.41	1.11	1.40		1.83
	C3-C4	1.35	1.39	1.67	1.45	1.86	
	C4-C5	1.45	1.46	1.14	1.19		
	C5-N1/C5-C1	2.12	2.08	0.36	0.53		
TS-*cis*	N1-N2/C1-C2	1.42	1.47	1.02	1.16		
	N2-C3/C2-C3	1.40	1.40	1.09	1.43		1.84
	C3-C4	1.35	1.40	1.70	1.43	1.88	
	C4-C5	1.46	1.47	1.13	1.16		1.44
	C5-N1/C5-C1	2.04	1.97	0.42	0.61		
product-*trans*	N1-N2/C1-C2	1.47	1.52	0.97	1.01		
	N2-C3/C2-C3	1.43	1.40	1.03	1.44		1.91
	C3-C4	1.34	1.40	1.80	1.44	1.94	
	C4-C5	1.50	1.52	1.02	1.01		
	C5-N1/C5-C1	1.61	1.59	0.79	0.93		
product-*cis*	N1-N2/C1-C2	1.46	1.52	0.98	1.01		
	N2-C3/C2-C3	1.43	1.41	1.03	1.48		1.91
	C3-C4	1.34	1.39	1.79	1.40	1.94	
	C4-C5	1.50	1.52	1.02	1.02		
	C5-N1/C5-C1	1.65	1.59	0.75	0.94		

charge mainly at C3 and C5. For the unprotonated reactant **3-1** NBO analyses reveal two distinct double bonds N2-C3 and C4-C5, whereas for the protonated reactant **3-2** only one π orbital remains located at C4-C5; additionally an anti-bonding, partially filled p-orbital appears at C3. The electrons in p- and π-orbitals sum up to almost six in both cases.

The pentadienyl anion **3-3** contains a plane of symmetry which affects the electron distribution: the charge is rather evenly distributed over the five future ring atoms and the bond orders show less deviations pointing to a delocalized system. There are two double bonds C1-C2 and C4-C5 in **3-3** compared to just one double bond C4-C5 for **3-2**. These two double bonds are accompanied by a partially filled p-orbital at C3. The electrons in the p- and π-orbitals of **3-3** sum up to less than five electrons (cf. Tables 3.8 and 3.9). Careful evaluation of the NBO results reveals that due to delocalization electrons are moved to antibonding π^*-orbitals of **3-3**. So, taking electrons in these orbitals also into account again yields a total of six electrons.

The electron distribution changes when moving to the transition state. As expected, upon bond formation the N1-C5 distance is reduced and the respective bond order increases from almost zero to 0.4-0.6 at the TS and further to 0.8-0.9 in the final product. For **3-2** both the *cis*- and *trans*-TS are similar with regard to the electronic structure. The lone pairs at the nitrogen atoms are kept, while charges and occupations are slightly shifted. On the other hand, the double bond is shifted to C3-C4 while the partially filled p-orbital moves to C5. At that point NBO analysis does not yield any bonding orbital between N1 and C5. Again, the electrons in the p- and π-orbitals sum up to six.

By contrast, these transition states differ for the pure carbon analogue **3-3**. While in both cases the negative charge is mainly located at C2 and C4 and a C2-C3 double bond is formed, there is a second double bond C4-C5 for TS-*cis* but only a lone pair at C4 at TS-*trans*, each of them filled with around 1.4 electrons. While the charge distribution at TS-*trans* is already similar to that in the final product, it is right in between reactant and product at TS-*cis*. In both cases, a new σ-orbital along the bond C1-C5 is already formed at the TS. This newly formed bond has to be taken into account in the analysis as it is part of the extended π-system characteristic for 6π-electrocyclizations. The occupations in π-orbitals (at atoms C1 to C5), in the π^*-orbitals (delocalization), and in the new bond orbital again sum up to six.

At the product stage **3-3** is still symmetric with a delocalized system from C2 via C3 to C4 (BO 1.4). In the case of the hydrazone heterosystem **3-2** the product has a distinct C3-C4 double bond (BO 1.8) and a lone pair localized at N2.

In a pericyclic 6π-electrocyclization the six electrons need to be located in a closed loop cyclic array (*i.e.* in a ring orbital). Inspection of the highest lying orbitals of **3-2** at the transition state could not provide any evidence for the presence of such an orbital. Such a closed loop orbital gives rise to an aromatic transition state that should be identifiable through a NICS analysis.[75] In case of an aromatic transition state leading from a non-aromatic reactant to a non-aromatic product the NICS values need to have a minimum at the transition state. However, no clear minimum could be found for either transition state structure in the case of **3-2**.

For **3-3** the classification of the reaction depends on the relative configuration at the transition state. For TS-*trans* no cyclic orbital can be found, and likewise the NICS analysis does not yield a pronounced minimum at the TS. By contrast, for TS-*cis*, a cyclic orbital is present and a distinct minimum of the NICS values is found at the TS. Hence, this confirms the pericyclic character of the cyclization of **3-3** via TS-*cis*. Moreover, the stereochemical conditions for a pericyclic reaction are obeyed in this case: For a thermal 6π-electrocyclization only the disrotatory motion of the terminal groups is allowed (see above). This criterion is fulfilled in case of the TS-*cis* whereas the pathway via TS-*trans* involves a conrotatory disallowed motion.

To sum up, in the case of the cyclization of **3-2** the conditions of concerted disrotation and an aromatic TS are not fulfilled, and the reaction thus cannot be classified as pericyclic. By contrast, the cyclization of the isoelectronic pure carbon analogue **3-3** is confirmed to be pericyclic. As discussed elsewhere,[76] this difference may be related to the symmetry breaking introduced by the heteroatoms in the ring of **3-2**.

The cyclization of **3-2** may better be regarded as pseudopericyclic reaction, given the presence of a cyclic array of orbitals with disconnections, the planar TS geometries, and the lack of stereoselectivity. It should be noted, however, the computed reaction barriers of about 16 to 18 kcal/mol (cf. Table 3.7) are relatively high since typical pseudopericyclic reactions are normally found to be almost barrierless. Alternatively, this cyclization reaction may also be considered as an intramolecular nucleophilic addition, with the lone pair at N1 attacking the C5 atom which is in conjugation to the formally positively charged C3 atom (allyl group C3-C4-C5). This characterization as a nucleophilic addition is supported by the NBO analysis that reveals a strong donation from the respective lone pair at N1 to C5 at the transition state. On the other hand, this would formally resemble a 5-*endo*-trig reaction which is believed to be unlikely according to Baldwin's rules;[77] however, these rules are only qualitative and considered most suitable for systems without heteroatoms,[78] so they may not apply in the case of **3-2**.

Conclusion

In summary, the cyclization of the protonated hydrazone **3-2** is not pericyclic as no closed-loop 6π-electron orbital and no concerted disrotation are detectable at the transition state. This is in contrast to the cyclization of the isoelectronic pentadienyl anion **3-3** that is confirmed to be pericyclic in the present investigation. The mechanism of the cyclization of **3-2** may be described by two complementary concepts. From a geometrical view it is a pseudopericyclic reaction (closed-loop orbital with orbital disconnection at the TS, planar TS structure). From a nucleophilicity view it can be described as an intramolecular nucleophilic addition because of strong electron donation from the lone pair at N1 to the allylic C5 atom.

3.4 Investigating a ferrate complex as intermediate in iron catalyzed cross coupling

The mechanism for methylation of 4-chlorobenzoyl chloride by the ferrate complex **4-1** was studied at the DFT level. The initial DFT calculations employed the OPBE functional[79, 80] in combination with the 6-311+G** basis set,[69, 70, 81] and the LANL2DZ pseudopotential and basis set for the iron atom.[82–84] The OPBE functional has been shown in the literature to give good descriptions of spin states,[85, 86] and it was therefore chosen to determine the preferred spin state of **4-1**.

For this purpse, complex **4-1** was optimized as singlet, triplet, and quintet, starting in each case from the crystal structure. Table 3.10 lists the resulting relative energies and the RMSD values (root mean square deviations) relative to the crystal structure. The quintet state is lowest in energy followed by the triplet state and, still higher, the singlet state. The RMSD values clearly show that the computed geometry of the quintet is closest to the crystal structure, whereas the geometries of the singlet and triplet deviate strongly. Hence, the ground state of complex **4-1** is a quintet (consistent with an oxidation state of +2 for iron).

For further validation, additional functionals were tested that are recommended in the literature for transition metal complexes:[43, 87–90] M06,[91] B3LYP,[41, 92] B3LYP+D with D3 dispersion corrections,[43] and TPSSh.[93] Complex **4-1** was optimized in the quintet state using these functionals. Again the 6-311+G** basis set was chosen for all atoms except iron, which was described by the SDD basis set and pseudopotential.[63] The smallest errors in geometry (compared to the crystal structure) are indeed found for the quintet structures computed with the OPBE functional closely followed by B3LYP.

For further analysis the geometries optimized at the OPBE-level were used for single-point calculations with several other functionals (BP86, B3LYP, B3LYP+D, TPSSh, M06) and/or larger basis sets such as QZVP[62] or SDD[82, 94] for iron (SDD pseudopotential as well). When appropriate, solvent effects were taken into account by using the polarizable continuum model (PCM)[46] with THF as solvent (as in the experiment). All calculations were carried out using the Gaussian09 program package, revision D.01.[65] For more details regarding the computational methods please see Appendix E.

Single Transfer

An exemplary reaction for the methylation by ferrate complex **4-1** is the transfer of a methyl group to 4-chlorobenzoyl chloride **4-2**, see Figure 3.19. As can be seen, **4-1** carries in total five methyl groups. Four of them are directly bound to the central iron atom forming a tetrahedral coordination sphere. The fifth methyl group is farther away from the central iron atom (3.84 Å compared to 2.05 to 2.27 Å) being coordinated to the three lithium atoms in-between. To distinguish these five methyl groups they are colored differently in Figure 3.19. The black methyl group is in the top position (in short: to), the two red ones are equivalent by symmetry and occupy the back position (ba), the blue one is in the front position (fr), and the green one is located below the lithium atoms in the bottom position (bo).

For the oxidative addition-reductive elimination mechanism, intermediates with the substrate **4-2** being attached to the iron complex **4-1** were located, both in the triplet and quintet state (Figure 3.20). The free energy relative to the separated reactants is 1.11 kcal/mol for the quintet species and 0.45 kcal/mol for the triplet species (*i.e.* 0.66 kcal/mol lower in free energy). In both cases, the carbonyl carbon C1 is bound to the central iron atom (Fe–C1: quintet, 1.98 Å; triplet: 1.81 Å), thereby distorting the tetrahedral coordination sphere around iron, while the chlorine atom binds to the free lithium atom (Li–Cl: quintet, 2.13 Å; triplet, 2.10 Å); the pertinent Li-O distances are similar (quintet,

Table 3.10: Energies and free energies (relative to the quintet state) and RMSD values of the optimized geometries with respect to the crystal structure of complex **4-1** (OPBE/6-311+G**, Fe: LANL2DZ).

spin state	singlet	triplet	quintet
E (kcal/mol)	34.56	17.24	0.00
G (kcal/mol)	39.93	20.66	0.00
RMSD bonds (Å)	0.19	0.13	0.07
RMSD angles (°)	13.5	15.5	4.7

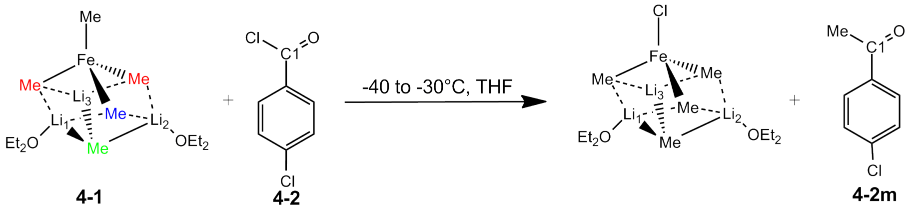

Figure 3.19: Investigated reaction for the alkylation of 4-chlorobenzoyl chloride **4-2** by ferrate complex **4-1**; reaction conditions are indicated. To highlight the different methyl groups they are colored (black: top, red: back, blue: front, green: bottom).

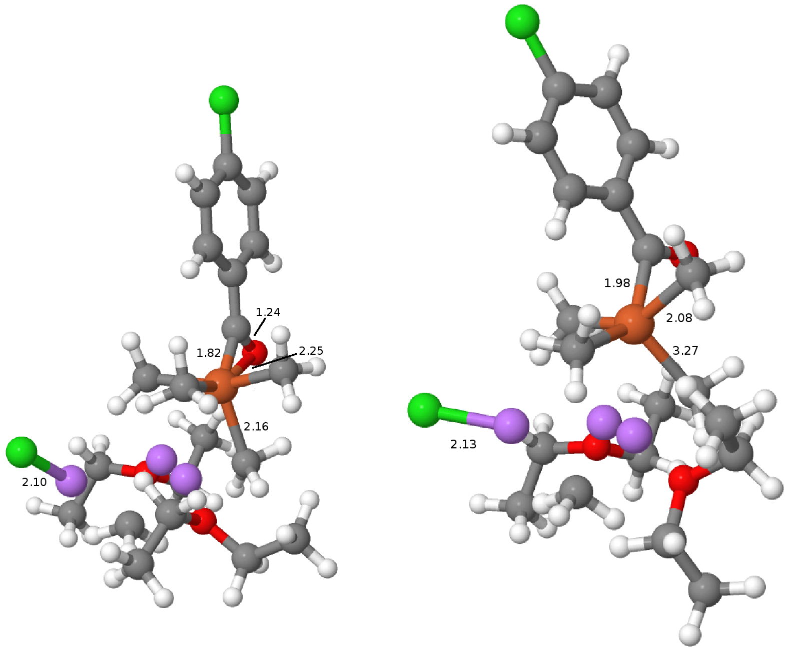

(a) triplet (b) quintet

Figure 3.20: Putative intermediate structures for the addition of 4-chlorobenzoyl chloride **4-2** to complex **4-1** in the triplet state (left) and the quintet state (right) (color code: gray: carbon, white: hydrogen, brown: iron, violet: lithium, red: oxygen, green: chlorine). Key distances are given in Å.

2.08 and 2.16 Å; triplet, 2.12 and 2.17 Å). In the quintet intermediate the iron atom remains almost at the center of a distorted tetrahedron, whereas in the triplet state the Fe[Me]$_4$-unit with the attached substrate is turned away from the center of the lithium triangle. However, it was not possible to locate any transition state for oxidative addition or reductive elimination that would connect these intermediates to reactants or products. Scans of the quintet potential energy surface indicate that the oxidative addition step will require somewhat more activation than the substitution reaction (see below) and that the subsequent reductive elimination step should be facile. We also did not find any corresponding pathways when allowing for intersystem crossing (as commonly encountered in iron chemistry).

On the other hand, distinct transition states (TS) could be located for the substitution pathway in the quintet state. As an example, Figure 3.21 shows the transition state for the transfer of the methyl group at the top position of complex **4-1** to substrate **4-2**. This transition state is consistent with a substitution mechanism. The transition vector (imaginary frequency: $435i$ cm^{-1}) describes the motion of the methyl-carbon (Me) along a straight line between iron and the carbonyl carbon C1 of substrate **4-2**. The angle between Fe, Me, and C1 is 171°, and the Fe–Me and Me–C1 distances are 2.19 and 2.12 Å, respectively. For comparison, the corresponding Fe–Me distance in the isolated ferrate complex **4-1** is 2.05 Å, and the C1–Me bond length in the product is 1.51 Å. The hydrogen atoms of the migrating methyl group invert upon moving from the ferrate complex towards **4-2**. Moreover, the closer the methyl group gets towards the carbonyl group, the farther away moves the chloride bound to the carbonyl carbon (C1–Cl: quintet reactant, 1.80 Å; quintet TS, 1.95 Å). In fact, following the IRC path towards the products indicates some kind of double substitution: the chloride of substrate **4-2** is replaced by a methyl group from **4-1** but then moves into the free coordination site at the iron center, replacing the methyl group and thereby keeping the ferrate complex in shape.

Analogous transition states in the quintet state were located for the transfer of methyl groups from the back and bottom positions, and their nature was confirmed by frequency analysis and IRC calculations as well. A similar transition state could also be found at the front position, but IRC calculations failed to connect it with the expected product but yielded an unreasonably distorted structure (probably because of steric hindrance by the nearby ether groups). Therefore, methyl transfer from the front position will not be further considered in the following.

Table 3.11 lists Gibbs free energies of the three transition states relative to the separated reactants **4-1** and **4-2** at infinite distance. Geometries were fully optimized at the OPBE-level (entry 1) and at the B3LYP+D-level (entry 9).

Table 3.11: Relative Gibbs free energies of the transition states in the quintet state for single methyl transfers from the back, bottom, and top positions. Entries 1 and 9 are optimized, the others represent single-point calculations at the geometries obtained at the OPBE-level. Energies are given in kcal/mol relative to separated reactants. Basis set: 6-311+G**; for iron the basis set and pseudopotential are indicated individually in the footnotes.

entry	method	top	back	bottom
1 opt	OPBE[1]	28.67	26.72	28.40
2	OPBE[2]	21.83	28.08	23.02
3	OPBE[3]	29.78	26.82	28.45
4	OPBE[4]	28.04	26.26	28.09
5	OPBE[5]	20.72	27.42	22.63
6	B3LYP[4]	28.26	23.43	25.59
7	B3LYP+D[4]	21.80	14.17	18.08
8	B3LYP+D[5]	14.11	16.06	12.97
9 opt	B3LYP+D[5]	17.63	12.80	17.69
10	BP86[4]	21.88	17.19	20.68
11	M06[4]	22.36	16.67	21.23
12	TPSSh[4]	25.09	20.52	23.48

[1] Fe: LANL2DZ (basis set and pseudopotential)

[2] Fe: LANL2DZ (basis set and pseudopotential), PCM (THF)

[3] Fe: SDD (basis set and pseudopotential)

[4] Fe: QZVP, SDD (pseudopotential)

[5] Fe: QZVP, SDD (pseudopotential), PCM (THF)

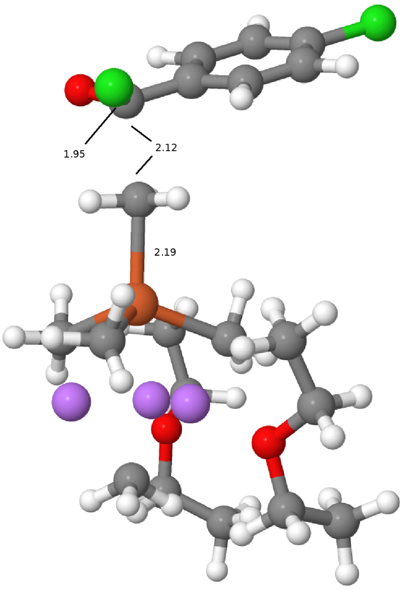

Figure 3.21: Transition state for the transfer of the methyl group from the top position of complex **4-1** to 4-chlorobenzoyl chloride **4-2** in the quintet state (color code: gray: carbon, white: hydrogen, brown: iron, violet: lithium, red: oxygen, green: chlorine). Key distances are given in Å.

Single-point calculations were performed at the OPBE-optimized geometries (all other entries) to assess the effects of various computational options (functionals, basis sets, pseudopotentials, solvent effects, dispersion corrections); zero-point energies and thermal corrections were taken from harmonic frequency calculations at the OPBE-level.

The trends are generally the same for the relative energies and relative free energies of the three transition states, so the discussion is focused on the latter in the following (Table 3.11). The OPBE results indicate that the choice of basis set and pseudopotential has only a minor influence on the relative free energies (up to 1 kcal/mol, see entries 1, 3, and 4 as well as 2 and 5). Comparing the results of different functionals using the large QZVP basis and the SDD pseudopotential at iron shows that OPBE generally yields the highest barriers: the computed values are lower for B3LYP by 0-3 kcal/mol (entries 4 vs. 6), for BP86 by 6-9 kcal/mol (entries 4 vs. 10), for M06 by 6-10 kcal/mol (entries 4 vs. 11), and for TPSSh by 3-6 kcal/mol (entries 4 vs. 12); in all cases, the computed barriers are lowest for methyl transfer at the back position, while those at the top and bottom positions tend to be somewhat larger and of similar magnitude. Explicit inclusion of dispersion effects at the B3LYP level lowers the computed barriers substantially, by 6-9 kcal/mol (entries 6 vs. 7), and brings them rather close, within 1-3 kcal/mol, to those obtained from the M06 functional that implicitly accounts for dispersion (entries 7 vs. 11). Inclusion of solvent effects via PCM(THF) significantly lowers the computed barriers at the top and bottom positions, by 7-8 and 5 kcal/mol, respectively, and slightly increases them by 1-2 kcal/mol at the top position (entries 1 vs. 2, 4 vs. 5, and 7 vs. 8).

Obviously, the chosen computational methods predict quite different barriers, and it is hard to decide *a priori* on the most trustworthy approach. The OPBE functional seems least suitable for the energetics in view of the fact that modern functionals with a good track record in transition metal chemistry (M06, TPSSh) give much smaller barriers. Moreover, dispersion and solvent effects appear to be quite large and non-uniform in the present case, and should thus be both included explicitly. Therefore, we decided to re-optimize all relevant species at the B3LYP+D level using the large QZVP basis and the SDD pseudopotential at iron and representing solvent effects through PCM (THF); we consider the resulting free energy barriers to be our most reliable results (entry 9). At this B3LYP+D level, the lowest barrier is found for the methyl transfer at the back position (12.8 kcal/mol), significantly smaller than those at the top and bottom positions (17.6-17.7 kcal/mol). The reaction at the back position is also favored by other approaches (see e.g. entries 6 and 10-12), which however predict larger values since they do not account for dispersion and/or solvent effects.

For the sake of completeness, reactions in the triplet and singlet states were considered as well since intersystem crossings are common in iron chemistry. Only some of the corresponding transition states for methyl transfer could be located, but they were always much higher in energy than those in the quintet state. Therefore one may conclude that spin crossings do not play a role in the substitution reactions investigated here.

Multiple Transfer

It is known from experiment that not only one methyl group is transferred per complex **4-1** but three or four. Therefore transition states for the whole sequence of methyl transfers between complex **4-1** and 4-chlorobenzoyl chloride **4-2** were located (without considering the methyl group in the front position, as discussed above). The geometries were first optimized at the OPBE-level and then re-optimized at the B3LYP+D-level. Generally, the geometries of the transition states for the second, third, and fourth methyl transfer are qualitatively quite similar to those for the first transfer. In Table 3.12 relative Gibbs free energies are presented only for three of the most probable sequences of multiple transfers, *i.e.* those with the lowest barriers to overcome; they are visualized in Figure 3.22. The free energy barriers are given in Table 3.12 relative to the

Table 3.12: Free energy barriers in kcal/mol for consecutive transfer of different methyl groups from complex **4-1** to substrate molecules **4-2**, each relative to the preceding minimum.

Sequence	1^{st}	2^{nd}	3^{rd}	4^{th}
OPBE/6-311+G** Fe: LANL2DZ, optimized				
ba-ba-bo-to	26.72	25.05	22.73	33.18
ba-bo-ba-to	26.72	27.55	24.49	33.18
bo-ba-ba-to	28.40	26.38	24.49	33.18
B3LYP+D/6-311+G** Fe: QZVP, SDD (pseudopotential), PCM (THF), optimized				
ba-bo-ba-to	12.80	9.07	13.64	18.69
ba-ba-bo-to	12.80	14.15	13.12	18.69
to-ba-bo-ba	17.63	14.50	8.34	13.89

preceding minimum, while the Gibbs free energies are plotted in Figure 3.22 with respect to the separated reactants (**4-1** and four molecules of **4-2**). For further details please see Appendix E.

The following comments are based on the results obtained by geometry optimization at the B3LYP+D-level with inclusion of dispersion and solvent effects, which is the most reliable approach applied presently (see above, Table 3.11, entry 9). The most favorable sequence starts with a substitution at the back position, followed by substitution at the bottom and the second back position (ba-bo-ba), with barriers of similar magnitude (9.1-13.6 kcal/mol), while the fourth substitution at the remaining top position (to) is notably less facile (18.7 kcal/mol). The alternative ba-ba-bo-to sequence has a very similar free energy profile. When the reaction starts at the top position, the initial free energy barrier is higher (17.6 kcal/mol) while the following steps in the to-ba-bo-ba sequence are quite facile. The computed barriers indicate that the transfer of three methyl groups per ferrate complex is probable (if the first one is feasible) whereas the fourth transfer is less likely (involving the less favorable substitution at the top position). Generally speaking, the barriers for methyl transfer at the back and top positions remain similar regardless whether they occur in the first or subsequent steps, whereas those at the top position are lowered substantially in later steps (presumably because of the changes in the ligand sphere of complex **4-1**).

Experimentally, the methylation of 4-chlorobenzoyl chloride **4-2** by complex **4-1** is very facile and fast (complete consumption of 0.57 mmol of **4-2** within 20 minutes at -30 to -40 °).[15] In line with these findings, the overall reaction is computed to be strongly exergonic (see Figure 3.22). The computed free energy barriers are clearly much too high at the OPBE-level, but more realistic

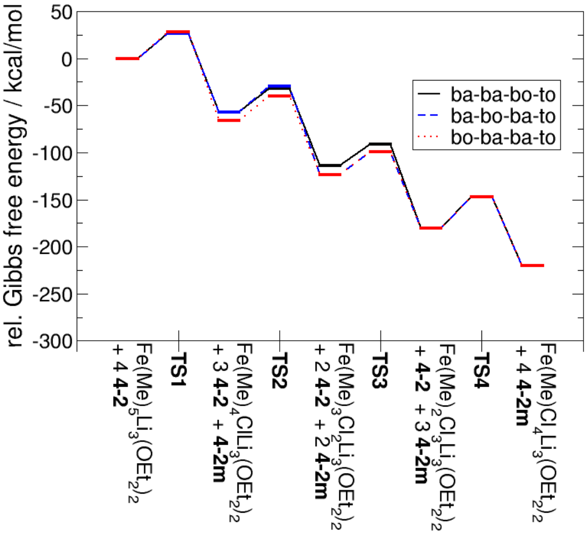

(a) optimized: OPBE/6-311+G** Fe: LANL2DZ

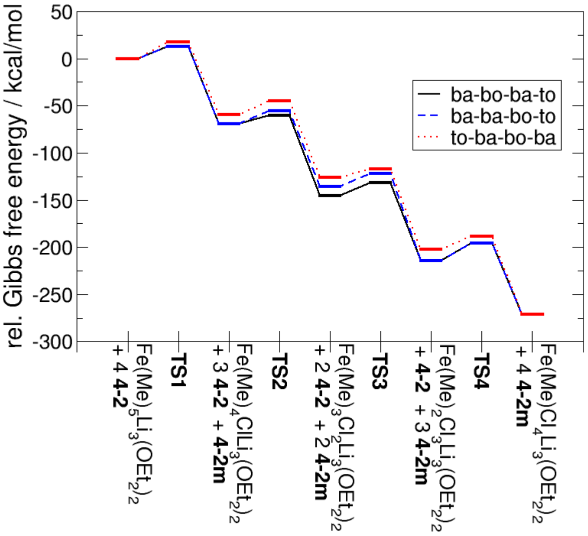

(b) optimized: B3LYP+D/6-311+G**, Fe: QZVP, SDD (pseudopotential), PCM (THF)

Figure 3.22: Free energy profiles for subsequent transfer of methyl groups from complex **4-1** to **4-2**, relative to the separated reactants. The sequences of transfer positions are indicated in the figures (see text).

at the preferred B3LYP+D level with inclusion of dispersion and solvent effects (maximum barrier of 13.6 kcal/mol for the first three steps). It is known from the literature that B3LYP does generally reasonably well in estimating reaction barriers, with a slight tendency to overestimate them.[95, 96] One should also note that experimentally there may be some side reactions, because 100 % conversion was reported to lead to a yield of 60 %.[15] Given these caveats, the B3LYP+D results are considered to be in reasonable agreement with the experimental findings.

Conclusion

The OPBE functional was found suitable for computing reasonable geometries and spin state energies for the organoferrate complex **4-1**, but predicted barriers to methyl transfer that are clearly much too high. More realistic barriers were computed employing the B3LYP functional including Grimme dispersion corrections and a PCM treatment of the solvent environment. No transition states could be located for a two step-mechanism consisting of an oxidative addition and a reductive elimination. Instead, the DFT computations showed the methylation to proceed via a direct substitution mechanism. Methyl transfers are most facile for the methyl groups in the back positions followed by the top and bottom positions. In qualititative agreement with the experimental findings multiple methyl transfers are feasible: the barriers for the first three transfers are similar and rather low whereas the fourth transfer requires some more activation.

Chapter 4

Closing Remarks

A broad range of topics concerning chemical structures and reaction mechanisms is covered by this thesis. It shows that today theoretical methods such as semi-empirical computations and density functional calculations are valuable tools for chemists.

Nonadiabatic dynamics simulations are nowadays feasible even for medium-size organic chromophores in solution, such as guanine in water, which unravel the possible photoinduced processes and the various relaxation channels to the electronic ground state, thus helping to interpret the experimental findings from ultrafast photoelectron spectroscopy (chapter 3.1). The electronic structure and the nature of bonding in complicated reaction intermediates can be elucidated using density function theory in combination with established analysis tools, thus providing the chemists with a well-founded qualitative description of species such as bimetallic transition metal complexes, which is based on computation rather than speculation (chapter 3.2). In the realm of chemical reactivity and catalysis, density functional calculations have become reliable enough to clarify the nature of crucial transition states by distinguishing between different proposed qualitative scenarios, as shown in the case study on the cyclization of a protonated hydrazone (chapter 3.3), and they are also able to verify experimental hypotheses on the mechanistic relevance of short-lived intermediates, as shown in another case study on organoferrate complexes and their possible role in iron cross coupling reactions (chapter 3.4).

Thus, the invention of organic structure theory in the 19th century and the development of quantum mechanics from the early 20th century on led to valuable new tools in chemical research. State of the art computational chemistry complements the experimental techniques to answer questions on chemical structure and reaction mechanisms.

Bibliography

[1] A. J. Rocke. Kekulé, Butlerov, and the Historiography of the Theory of Chemical Structure. *Brit. J. History of Science* **1981**, *14*, 27–57.

[2] V. I. Minkin. Current Trends in the Development of A. M. Butlerov's Theory of Chemical Structure. *Russ. Chem. Bull. Int. Ed.* **2012**, *61*, 1265–1290.

[3] H. M. Leicester. Kekulé, Butlerov, Markovnikov: Controversies on Chemical Structure from 1860 to 1870 in *Kekulé Centennial*, O. Benfey (Ed.), American Chemical Society, Washington D.C., **1966**, pp. 13–23.

[4] G. N. Lewis. The Atom and the Molecule. *J. Am. Chem. Soc.* **1916**, *38*, 762–785.

[5] J. Hudson, *The History of Chemistry*, Chapman and Hall, New York, **1992**.

[6] H. Eyring. The Activated Complex in Chemical Reaction. *J. Chem. Phys.* **1935**, *3*, 107–115.

[7] M. G. Evans, M. Polanyi. Some Applications of the Transition State Method to the Calculation of Reaction Velocities, Especially in Solution. *Trans. Faraday Soc.* **1935**, *31*, 875–894.

[8] W. Heisenberg. Über Quantentheoretische Umdeutung Kinematischer und Mechanischer Beziehungen. *Z. Phys.* **1925**, *33*, 879–893.

[9] E. Schrödinger. Quantisierung als Eigenwertproblem. *Ann. Phys.* **1926**, *79*, 361–376.

[10] M. Daniels, W. Hauswirth. Fluorescence of the Purine and Pyrimidine Base of a Nucleic Acid in Neutral Aqueous Solution at 300 K. *Science* **1971**, *171*, 675–677.

[11] A. S. K. Hashmi. Homogeneous Gold Catalysis Beyond Assumptions and Proposals - Characterized Intermediates. *Angew. Chem. Int. Ed.* **2010**, *49*, 5232–5241.

[12] G. Seidel, B. Gabor, R. Goddard, B. Heggen, W. Thiel, A. Fürstner. Gold Carbenoids: Lessons Learnt from a Transmetalation Approach. *Angew. Chem. Int. Ed.* **2014**, *53*, 879–882.

[13] M. Mahlau, B. List. Asymmetric Counteranion-Directed Catalysis: Concept, Definition, and Applications. *Angew. Chem. Int. Ed.* **2013**, *52*, 518–533.

[14] S. Müller, B. List. A Catalytic Asymmetric 6π-Electrocyclisation - Enantioselective Synthesis of 2-Pyrazolines. *Angew. Chem. Int. Ed.* **2009**, *48*, 9975–9978.

[15] A. Fürstner, R. Martin, H. Krause, G. Seidel, R. Goddard, C. W. Lehmann. Preparation, Structure and Reactivity of Nonstabilized Organoiron Compounds. Implications for Iron-Catalyzed Cross Coupling Reactions. *J. Am. Chem. Soc.* **2008**, *130*, 8773–8787.

[16] J. F. Hartwig, *Organotransition Metal Chemistry: From Bonding to Catalysis*, University Science Books, Herndon, **2010**.

[17] C. C. C. J. Seechurn, M. O. Kitching, T. J. Colacot, V. Snieckus. Palladium-Catalyzed Cross-Coupling: A Historical Contextual Perspective to the 2010 Nobel Prize. *Angew. Chem. Int. Ed.* **2012**, *51*, 5062–5085.

[18] B. D. Sherry, A. Fürstner. The Promise and Challenge of Iron-Catalyzed Cross Coupling. *Acc. Chem. Res.* **2008**, *41*, 1500–1511.

[19] J. Kleimark, A. Hedström, P.-F. Larsson, C. Johansson, P.-O. Norrby. Mechanistic Investigation of Iron-Catalyzed Coupling Reactions. *ChemCatChem* **2009**, *1*, 152–161.

[20] B. Scheiper, M. Bonnekessel, H. Krause, A. Fürstner. Selective Iron-Catalyzed Cross-Coupling Reactions of Grignard Reagents with Enol Triflates, Acid Chlorides, and Dichloroarenes. *J. Org. Chem.* **2004**, *69*, 3943–3949.

[21] R. B. Bedford, P. B. Brenner, E. Carter, P. M. Cogswell, M. F. Haddow, J. N. Harvey, D. M. Murphy, J. Nunn, C. H. Woodall. TMEDA in Iron-Catalyzed Kumada Coupling: Amine Adduct versus Homoleptic "ate" Complex Formation. *Angew. Chem. Int. Ed.* **2014**, *53*, 1804–1808.

[22] J. Kleimark, P.-F. Larsson, P. Emamy, A. Hedström, P.-O. Norrby. Low Temperature Studies of Iron-Catalyzed Cross-Coupling of Alkyl Grignard Reagents with Aryl Electrophiles. *Adv. Synth. Catal.* **2012**, *354*, 448–456.

[23] Q. Ren, S. Guan, F. Jiang, J. Fang. Density Functional Theory Study of the Mechanisms of Iron-Catalyzed Cross-Coupling Reactions of Alkyl Grignard Reagents. *J. Phys. Chem.* **2013**, *117*, 756–764.

[24] A. R. Leach, *Molecular Modelling: Principles and Applications*, Pearson Education, Harlow, **2001**.

[25] F. Jensen, *Introduction to Computational Chemistry*, Wiley, West Sussex, **2006**.

[26] W. Koch, M. C. Holthausen, *A Chemist's Guide to Density Functional Theory*, Wiley-VCH, Weinheim, **2001**.

[27] A. Szabo, N. S. Ostlund, *Modern Quantum Chemistry*, Dover, Mineola, **1996**.

[28] D. Hartree. The Wave Mechanics of an Atom with a Non-Coulomb Central Field. Part I: Theory and Methods. *Math. Proc. Cambridge Philos. Soc.* **1928**, *24*, 89–110.

[29] D. Hartree. The Wave Mechanics of an Atom with a Non-Coulomb Central Field. Part II. *Math. Proc. Cambridge Philos. Soc.* **1928**, *24*, 111–132.

[30] V. Fock. Näherungsmethoden zur Lösung des quantenmechanischen Mehrkörperproblems. *Z. Phys.* **1930**, *61*, 126–148.

[31] C. C. J. Roothaan. New Developments in Molecular Orbital Theory. *Rev. Mod. Phys.* **1951**, *23*, 69–89.

[32] G. G. Hall. The Molecular Orbital Theory of Chemical Valency VIII. A Method for Calculating Ionisation Potentials. *Proc. Roy. Soc. A* **1951**, *205*, 541–552.

[33] W. Weber, W. Thiel. Orthogonalization Corrections for Semiempirical Methods. *Theor. Chem. Acc.* **2000**, *103*, 495–506.

[34] J. A. Pople, D. P. Santry, G. A. Segal. Approximate Self-Consistent Molecular Orbital Theory. I. Invariant Procedures. *J. Chem. Phys.* **1965**, *43*, S129–S135.

[35] A. Koslowski, M. E. Beck, W. Thiel. Implementation of a General Multireference Configuration Interaction Procedure with Analytic Gradients in a Semiempirical Context Using the Graphical Unitary Group Approach. *J. Comput. Chem.* **2003**, *24*, 714–726.

[36] J. C. Tully. Molecular Dynamics with Electronic Transitions. *J. Chem. Phys.* **1990**, *93*, 1061–1071.

[37] P. Hohenberg, W. Kohn. Inhomogeneous Electron Gas. *Phys. Rev. B* **1964**, *136*, 864–871.

[38] W. Kohn, L. J. Sham. Self-Consistent Equations Including Exchange and Correlation Effects. *Phys. Rev. A* **1965**, *140*, 1133–1138.

[39] A. D. Becke. Density-Functional Exchange-Energy Approxmation with Correct Asymptotic Behavior. *Phys. Rev. A* **1988**, *38*, 3098–3100.

[40] J. P. Perdew, J. A. Chevary, S. H. Vosko, K. A. Jackson, M. R. Pederson, D. J. Singh, C. Fiolhais. Atoms, Molecules, Solids, and Surfaces: Applications of the Generalized Gradient Approximation for Exchange and Correlation. *Phys. Rev. B* **1992**, *46*, 6671–6687.

[41] A. D. Becke. Density Functional Thermochemistry. III. The Role of Exact Exchange. *J. Chem. Phys.* **1993**, *98*, 5648–5652.

[42] S. Grimme. Density Functional Theory with London Dispersion Corrections. *WIREs Comput. Mol. Sci.* **2011**, *1*, 211–228.

[43] S. Grimme, J. Antony, S. Ehrlich, H. Krieg. A Consistent and Accurate *ab initio* Parameterization of Density Functional Dispersion Correction (DFT-D) for the 94 Elements H-Pu. *J. Chem. Phys.* **2010**, *132*, 154104.

[44] E. K. U. Gross, W. Kohn. Time-Dependent Density-Functional Theory. *Adv. Quantum Chem.* **1990**, *21*, 255–291.

[45] F. Furche, K. Burke. Time-Dependent Density Functional in Quantum Chemistry in *Annual Reports Computational Chemistry*, D. Spellmeyer (Ed.), Elsevier, Amsterdam, **2005**, pp. 19–30.

[46] J. Tomasi, B. Mennucci, R. Cammi. Quantum Mechanical Continuum Solvation Models. *Chem. Rev.* **2005**, *105*, 2999–3093.

[47] H. M. Senn, W. Thiel. QM/MM Methods for Biological Systems. *Top. Curr. Chem.* **2007**, *268*, 173–290.

[48] H. M. Senn, W. Thiel. QM/MM Methods for Biomolecular Systems. *Angew. Chem. Int. Ed.* **2009**, *48*, 1198–1229.

[49] D. Bakowies, W. Thiel. Hybrid Models for Combined Quantum Mechanical and Molecular Mechanical Approaches. *J. Phys. Chem.* **1996**, *100*, 10580–10594.

[50] P. Sherwood, A. H. de Vries, M. F. Guest, G. Schreckenbach, C. R. A. Catlow, S. A. French, A. A. Sokol, S. T. Bromley, W. Thiel, A. J. Turner, S. Billeter,

F. Terstegen, S. Thiel, J. Kendrick, S. C. Rogers, J. Casci, M. Watson, F. King, E. Karlsen, M. Sjvoll, A. Fahmi, A. Schäfer, C. Lennartz. QUASI: A General Purpose Implementation of the QM/MM Approach and its Application to Problems in Catalysis. *J. Mol. Struct. (Theochem.)* **2003**, *632*, 1.

[51] S. Metz, J. Kästner, A. A. Sokol, T. W. Keal, P. Sherwood. ChemShell - a Modular Software Package for QM/MM Simulations. *WIREs Comput. Mol. Sci.* **2014**, *4*, 101–110.

[52] W. Thiel. MNDO. **2007**, MNDO program, version 6.1, Mülheim.

[53] W. L. Jorgensen, J. Chandrasekhar, J. D. Madura, R. W. Impey, M. L. Klein. Comparison of Simple Potential Functions for Simulating Liquid Water. *J. Chem. Phys.* **1983**, *79*, 926–935.

[54] Z. Lan, E. Fabiano, W. Thiel. Photoinduced Nonadiabatic Dynamics of 9H-Guanine. *ChemPhysChem* **2009**, *10*, 1225–1229.

[55] S. Yamazaki, W. Domcke, A. L. Sobolewski. Nonradiative Decay Mechanisms of the Biologically Relevant Tautomer of Guanine. *J. Phys. Chem. A* **2008**, *112*, 11965–11968.

[56] M. Barbatti, J. J. Szymczak, A. J. A. Aquino, D. Nachtigallová, H. Lischka. The Decay Mechanism of Photoexcited Guanine - A Nonadiabatic Dynamics Study. *J. Chem. Phys.* **2011**, *134*, 014304.

[57] M. Parac, M. Doerr, C. M. Marian, W. Thiel. QM/MM Calculation of Solvent Effects on Absorption Spectra of Guanine. *J. Comput. Chem.* **2010**, *31*, 90–106.

[58] V. Karunakaran, K. Kleinermanns, R. Improta, S. A. Kovalenko. Photoinduced Dynamics of Guanosine Monophophate in Water from Broad-Band Transient Absorption Spectroscopy and Quantum-Chemical Calculations. *J. Am. Chem. Soc.* **2009**, *131*, 5839–5850.

[59] H. Chen, S. Li. Ab Initio Study on Deactivation Pathways of excited 9H-Guanine. *J. Chem. Phys.* **2006**, *124*, 154315.

[60] T. Fujiwara, Y. Kamoshida, R. Morita, M. Yamashita. Temporally-separated Ultrafast-emission Dynamics of Neutral and Cationic Molecules in Guanine and its Derivative Aqueous Solution. *J. Photochem. Photobiol. B* **1997**, *41*, 114–121.

[61] J. P. Perdew. Density-Functional Approximations for the Correlation Energy of the Inhomogeneous Electron Gas. *Phys. Rev. B* **1986**, *33*, 8822–8824.

[62] F. Weigend, R. Ahlrichs. Balanced Basis Sets of Split Valence, Triple Zeta Valence and Quadruple Zeta Valence Quality for H to Rn: Design and Assessment of Accuracy. *Phys. Chem. Chem. Phys.* **2005**, *7*, 3297–3305.

[63] D. Andrae, U. Haeussermann, U. Dolg, H. Stoll, H. Preuss. Energy-adjusted ab initio Pseudopotentials for the Second and Third Row Transition Elements. *Theor. Chim. Acta* **1990**, *77*, 123–141.

[64] TURBOMOLE, V6.3. **2011**, a development of University of Karlsruhe and Forschungszentrum Karlsruhe GmbH, 1989–2007, TURBOMOLE GmbH, since 2007; available from www. turbomole.com.

[65] M. J. Frisch, G. W. Trucks, H. B. Schlegel, G. E. Scuseria, M. A. Robb, J. R. Cheeseman, G. Scalmani, V. Barone, B. Mennucci, G. A. Petersson, H. Nakatsuji, M. Caricato, X. Li, H. P. Hratchian, A. F. Izmaylov, J. Bloino, G. Zheng, J. L. Sonnenberg, M. Hada, M. Ehara, K. Toyota, R. Fukuda, J. Hasegawa, M. Ishida, T. Nakajima, Y. Honda, O. Kitao, H. Nakai, T. Vreven, J. J. A. Montgomery, J. E. Peralta, F. Ogliaro, M. Bearpark, J. J. Heyd, E. Brothers, K. N. Kudin, V. N. Staroverov, T. Keith, R. Kobayashi, J. Normand, K. Raghavachari, A. Rendell, J. C. Burant, S. S. Iyengar, J. Tomasi, M. Cossi, N. Rega, J. M. Millam, M. Klene, J. E. Knox, J. B. Cross, V. Bakken, C. Adamo, J. Jaramillo, R. Gomperts, O. Y. R. E Stratmann, A. J. Austin, R. Cammi, C. Pomelli, J. W. Ochterski, R. L. Martin, K. Morokuma, V. G. Zakrzewski, G. A. Voth, P. Salvador, J. J. Dannenberg, S. Dapprich, A. D. Daniels, O. Farkas, J. B. Foresman, J. V. Ortiz, J. Cioslowski, D. J. Fox. Gaussian 09. *Gaussian, Inc., Wallingford CT* **2010**.

[66] G. te Velde, F. M. Bickelhaupt, E. J. Baerends, C. F. Guerra, S. J. A. van Gisbergen, J. G. Snijders, Z. T. Chemistry with ADF. *J. Comput. Chem.* **2001**, *22*, 931–967.

[67] E. D. Glendening, C. R. Landis, F. Weinhold. Natural Bond Orbital Methods. *WIREs Comput. Mol. Sci.* **2012**, *2*, 1–42.

[68] R. F. W. Bader. Atoms in Molecules. *Acc. Chem. Res.* **1985**, *18*, 9–15.

[69] R. Ditchfield, W. J. Hehre, J. A. Pople. Self-Consistent Molecular Orbital Methods. IX. An Extended Gaussian-Type Basis for the Molecular-Orbital Studies of Organic Molecules. *J. Chem. Phys.* **1971**, *54*, 724728.

[70] M. J. Frisch, J. A. Pople. Self-Consistent Molecular Orbital Methods 25. Supplementary Functions for Gaussian Basis Sets. *J. Chem. Phys.* **1984**, *80*, 3265–3269.

[71] T. P. M. Goumans, A. W. Ehlers, K. Lammertsma, E.-U. Würthwein, S. Grimme. Improved Reaction and Activation Energies of [4+2] Cycloadditions, [3,3] Sigmatropic Rearrangements and Electrocyclizations with the Spin-Component-Scaled MP2 Method. *Chem. Eur. J.* **2004**, *10*, 6468–6475.

[72] S. M. Bachrach, *Computational Organic Chemistry*, John Wiley & Sons, Hoboken, **2007**.

[73] P. von Ragué Schleyer, C. Maerker, A. Dransfeld, H. Jiao, N. J. R. van Eikema Hommes. Nucleus-Independent Chemical Shift: A Simple and Efficient Aromaticity Probe. *J. Am. Chem. Soc.* **1996**, *118*, 6317–6318.

[74] J. Rodríguez-Otero, E. M. Cabaleiro-Lago. Criteria for the Elucidation of the Pseudopericyclic Character of the Cyclization of (Z)-1,2,4,6-Heptatetraene and Its Heterosubstituted Analogues: Magnetic Properties and Natural Bond Orbital Analysis. *Chem. Eur. J.* **2003**, *9*, 1837–1843.

[75] E. M. Cabaleiro-Lago, J. Rodríguez-Otero, S. M. Varela-Varela, A. P. na Gallego, J. M. Hermida-Ramón. Are Electrocyclisation Reactions of (3Z)-1,3,5-Hexatrienone and Nitrogen Derivatives Pseudopericyclic? A DFT Study. *J. Org. Chem.* **2005**, *70*, 3921–3928.

[76] J. P. Snyder. Perturbed Pericyclic Reactions: Stereochemical Consequences of Hetersubstitution. A Qualitative Mechanistic Model Based on the Non-preservation of Orbital Topology. *J. Org. Chem.* **1980**, *45*, 1341–1344.

[77] K. Gilmore, I. V. Alabugin. Cyclizations of Alkynes: Revisiting Baldwin's Rules for Ring Closure. *Chem. Rev.* **2011**, *111*, 6513–6556.

[78] J. Ichikawa, G. Lapointe, Y. Iwai. Nucleophilic 5-*endo-trig* Cyclizations of *N*-Homoallylic Sulfonamides: A Facile Method for the Construction of Pyrrolidine Rings. *Chem. Commun.* **2007**, 2698–2700.

[79] J. P. Perdew, K. Burke, M. Ernzerhof. Generalized Gradient Approximation Made Simple. *Phys. Rev. Lett.* **1996**, *77*, 3865–3868.

[80] A. J. Cohen, N. C. Handy. Dynamic Correlation. *Mol. Phys.* **2001**, *99*, 607–615.

[81] R. Krishnan, J. S. Brinkley, R. Seeger, J. A. Pople. Self-Consistent Molecular Orbital Methods. XX. A Basis Set for Correlated Wave Functions. *J. Chem. Phys.* **1980**, *72*, 650–654.

[82] T. H. Dunning, P. J. Hay. Gaussian Basis Sets for Molecular Calculations in *Modern Theoretical Chemistry, Vol. 3*, I. H. F. Schaefer (Ed.), Plenum, New York, **1977**, pp. 1–27.

[83] P. J. Hay, W. R. Wadt. *Ab Initio* Effective Core Potentials for Molecular Calculations. Potentials for K to Au Including the Outermost Core Orbitals. *J. Chem. Phys.* **1985**, *82*, 299–310.

[84] P. J. Hay, W. R. Wadt. *Ab Initio* Effective Core Potentials for Molecular Calculations. Potentials for the Transition Metal Atoms Sc to Hg. *J. Chem. Phys.* **1985**, *82*, 270–283.

[85] C. J. Cramer, D. G. Truhlar. Density Functional Theory for Transition Metals and Transition Metal Chemistry. *Phys. Chem. Chem. Phys.* **2009**, *11*, 10757–10816.

[86] M. Swart, A. W. Ehlers, K. Lammertsma. Performance of the OPBE Exchange-Correlation Functional. *Mol. Phys.* **2004**, *102*, 2467–2474.

[87] O. Salomon, M. Reiher, B. A. Hess. Assertion and Validation of the Performance of the B3LYP* Functional for the First Transition Metal Row and G2 Test Set. *J. Chem. Phys.* **2002**, *117*, 4729–4737.

[88] Y. Zhao, D. G. Truhlar. Density Functionals with Broad Applicability in Chemistry. *Acc. Chem. Res.* **2008**, *41*, 157–167.

[89] R. Valero, R. Costa, I. de P. R. Moreira, D. G. Truhlar, F. Illas. Performance of the M06 Family of Exchange-Correlation Functionals for Predicting Magnetic Coupling in Organic and Inorganic Molecules. *J. Chem. Phys.* **2008**, *128*, 114103.

[90] K. P. Jensen. Bioinorganic Chemistry Modeled with the TPSSh Density Functional. *Inorg. Chem.* **2008**, *47*, 10357–10365.

[91] Y. Zhao, D. G. Truhlar. The M06 Suite of Density Functionals for Main Group Thermochemistry, Thermochemical Kinetics, Noncovalent Interactions, Excited States, and Transition Elements: Two New Functionals and Systematic Testing of Four M06-Class Functionals and 12 Other Functionals. *Theor. Chem. Acc.* **2008**, *120*, 215–241.

[92] C. Lee, W. Yang, R. G. Parr. Development of the Colle-Salvetti Correlation-Energy Formula into a Functional of the Electron Density. *Phys. Rev. B* **1988**, *37*, 785–789.

[93] J. M. Tao, J. P. Perdew, V. N. Staroverov, G. E. Scuseria. Climbing the Density Functional Ladder: Nonempirical meta-generalized Gradient Approximation Designed for Molecules and Solids. *Phys. Rev. Lett.* **2003**, *91*, 146401.

[94] M. Dolg, U. Wedig, H. Stoll, H. Preuss. Energy-adjusted ab initio pseudopotentials for the first row transition elements. *J. Chem. Phys.* **1987**, *86*, 866–872.

[95] G. T. de Jong, D. P. Geerke, A. Diefenbach, M. Solá, F. M. Bickelhaupt. Oxidative Addition of the Ethane C-C Bond to Pd. An *Ab initio* Benchmark and DFT Validation Study. *J. Comput. Chem.* **2005**, *26*, 1006–1020.

[96] A. Kazaryan, E. J. Baerends. Assessment of Density Functional Methods for Reaction Energetics: Iridium-catalyzed Water Oxidation as Case Study. *J. Comput. Chem.* **2013**, *34*, 870–878.

Appendix A

Nonadiabatic Decay Dynamics of 9*H*-Guanine in Aqueous Solution

Berit Heggen, Zhenggang Lan and Walter Thiel

Phys. Chem. Chem. Phys., **2012**, 14, 8137 – 8146.

Carried out and analyzed all the calculations in the paper.

PCCP

Cite this: *Phys. Chem. Chem. Phys.*, 2012, **14**, 8137–8146

www.rsc.org/pccp

PAPER

Nonadiabatic decay dynamics of 9*H*-guanine in aqueous solution†

Berit Heggen,[a] Zhenggang Lan*[b] and Walter Thiel*[a]

Received 31st January 2012, Accepted 10th April 2012
DOI: 10.1039/c2cp40300e

The nonadiabatic decay of the biologically relevant guanine tautomer (9*H*-guanine) in aqueous solution has been investigated by trajectory surface hopping simulations in a quantum mechanical–molecular mechanical (QM–MM) framework. The QM part (9*H*-guanine) was treated at the semiempirical OM2/MRCI level, while the MM part (water) was described by the TIP3P force field. The optimized geometries for the relevant minima and conical intersections are qualitatively similar for 9*H*-guanine in the gas phase and in aqueous solution, while there are notable solvent-induced shifts in the computed vertical excitation energies (up to about 0.4 eV). Overall, the results from the static OM2/MRCI-based calculations are in reasonable agreement with the available *ab initio* and experimental data. The dynamics simulations show ultrafast nonradiative decay for 9*H*-guanine in water that is even slightly faster than in the gas phase, with time constants of 20 fs and around 0.3 ps for the $S_2 \rightarrow S_1$ and $S_1 \rightarrow S_0$ internal conversions, respectively. They predict a change in the $S_1 \rightarrow S_0$ decay mechanism when going from the gas phase to aqueous solution: the major pathway for 9*H*-guanine in water involves a conical intersection with an out-of-plane distortion of the carbonyl oxygen atom, which does not play any significant role in the gas phase, where the decay mainly proceeds *via* two other conical intersections characterized by ring distortions and out-of-plane displacement of the amino group, respectively. Possible reasons for this change in the mechanism are analyzed.

1 Introduction

The deexcitation mechanisms in nucleobases are of great interest as they are relevant for the photostability of DNA.[1–6] Actually, the nucleobases strongly absorb in the UV region (200 to 300 nm), right in the range of sunlight. Already in early experimental work, the quantum yield of fluorescence was found to be very low in the nucleobases.[7–9] This was attributed to very fast deexcitation by nonradiative decay, both in gas phase and in aqueous solution. More recent investigations with modern laser techniques reported decay rates in the picosecond and subpicosecond range.[2,3,10,11] There is consensus that these ultrafast processes in nucleobases involve conical intersections between different potential energy surfaces that are characterized by distorted aromatic systems.[2,12,13]

In this article, we focus on the biologically relevant tautomer of the nucleobase guanine, 9*H*-guanine (in short GUA). In the gas phase, an excited-state lifetime of 0.8 ps was measured in early experimental work on GUA,[14] while a later study using highly resolved pump–probe spectroscopy reported bi-exponential decay with time constants of 148 fs and 360 fs.[11] More data are available for the ultrafast nonadiabatic dynamics of GUA and its derivatives in aqueous solution. Already more than a decade ago, Fujiwara *et al.* observed picosecond decay in water at pH = 7 for GUA (5 ps), guanosine (GUO, 4 ps) and guanosine monophosphate (GMP, 4 ps), which was ascribed to $S_1 \rightarrow S_0$ internal conversion;[15] they also found decay constants on a much longer time scale (hundreds of picoseconds), which were assumed to correspond to solvent cooling after internal conversion.[15] With the advances in laser technology, more refined measurements of the S_1 lifetime became possible: Pecourt *et al.* obtained decay times of 0.46 ps for GUO in water by transient absorption spectroscopy.[16,17] Fluorescence up-conversion experiments by Peon and Zewail gave S_1 lifetimes of 0.69 ps and 0.86 ps for GUO and GMP, respectively.[18] A similar method was applied by Gustavsson, Markovitsi and their co-workers to explore the decay of 2′-deoxyguanosine (dGUO) and 2′-deoxyguanosine-5′-monophosphate (dGMP) in aqueous solution: they found two sub-ps decay time constants in both cases (dGUO: 0.16 ps and 0.78 ps, dGMP: 0.20 ps and 0.89 ps).[19,20] Such bi-exponential decay behavior was recently also reported for GMP by Karunakaran *et al.* using femtosecond transient absorption spectroscopy.[21] By combining their experimental

---

[a] *Max-Planck-Institut für Kohlenforschung, Kaiser-Wilhelm-Platz 1, 45470 Mülheim an der Ruhr, Germany. E-mail: thiel@mpi-muelheim.mpg.de*
[b] *Qingdao Institute of Bioenergy and Bioprocess Technology, Chinese Academy of Sciences, Qingdao, 266101, P. R. China. E-mail: lanzg@qibebt.ac.cn*

† Electronic supplementary information (ESI) available: A plot of the theoretical absorption spectrum, tables with additional gas-phase results, overlays of computed gas-phase structures, a survey of literature results, data on hydrogen bonding, and Cartesian coordinates of the optimized geometries. See DOI: 10.1039/c2cp40300e

observations with theoretical calculations of the underlying potential energy surfaces (PES), they arrived at the following detailed scenario for the nonadiabatic decay of GMP: after an ultrafast $S_2 \rightarrow S_1$ deexcitation (within 100 fs), GMP explores the rather flat S_1 PES near the Franck–Condon region, with a pseudo-planar S_1 minimum, before it reaches the proper nonplanar S_1 minimum through ring distortion; this process is assumed to correspond to the first measured time constant of 0.2 ps, and the decay from the nonplanar S_1 minimum to the ground state *via* a conical intersection then corresponds to the second measured time constant of 0.9 ps.[21]

On the theoretical side, several studies were performed to explore the excited states and deexcitation mechanisms of GUA in the gas phase.[22–32] All these studies support the existence of direct decay pathways on the S_1 PES (L_a state) from the Franck–Condon region to the conical intersection with the ground state (gs). Two minimum-energy structures on this L_a–gs conical intersection seam were located at the CASSCF, MRCI, and semiempirical OM2/MRCI levels,[26,28–32] one of them with a strong puckering of the six-membered ring and the other with a pronounced out-of-plane motion of the amino group. They were considered responsible for the ultrafast nonadiabatic decay of GUA.[29,30] A third conical intersection with an out-of-plane displacement of the carbonyl oxygen atom was also found at different levels of theory.[26,28–32] Finally, a fourth reaction channel was identified at higher excitation energies, which involves the stretching of one NH bond and leads to hydrogen dissociation *via* a repulsive $\pi\sigma^*$ state that crosses the initially populated bright excited state and the ground state.[30]

In addition to the static PES explorations, there are three published surface-hopping dynamics simulations that aim at elucidating the role of the different reaction channels in the excited-state dynamics of GUA in the gas phase.[31,32] At the OM2/MRCI level, Lan *et al.* found two such channels with time constants of 0.19 ps and 0.4 ps, with the hopping events occurring in the vicinity of the two L_a–gs conical intersections that are associated with the puckering of the six-membered ring in an envelope fashion (60%) and with the out-of-plane motion of the amino group (40%), respectively (see above).[31] At the *ab initio* MRCIS/6-31G* level, Barbatti *et al.* computed lifetimes of <20 fs and 0.22 ps for the nonadiabatic decay of the S_2 and S_1 state, respectively. They also found that the $S_1 \rightarrow S_0$ deactivation mainly proceeds *via* two L_a–gs conical intersection regions, with branching ratios of 67% (ring deformation) and 28% (out-of-plane motion of NH_2), plus a minor contribution of 5% from a third channel (out-of-plane motion of carbonyl oxygen).[32] While there are differences between the OM2/MRCI and MRCIS/6-31G* structures of the dominant L_a–gs conical intersection (ring deformation),[32] both share a similar topology, and there is reasonable agreement for the other two conical intersection structures and the overall dynamics scenario (see ESI† for more detailed comparisons). In this sense, the semiempirical OM2/MRCI and *ab initio* MRCIS/6-31G* approaches yield consistent results for gas phase GUA.[31,32] A third surface-hopping study on isolated GUA employed nonadiabatic *ab initio* molecular dynamics (na-AIMD) in combination with a restricted open-shell Kohn–Sham (ROKS) description of the two lowest singlet states (BLYP functional).[36] A mono-exponential fit to the time-dependent S_1 ensemble population (16 trajectories) gave an $S_1 \rightarrow S_0$ decay constant of 0.8 ps,[36] which is larger than the MRCIS/6-31G* and OM2/MRCI values of 0.22 and 0.4 ps, respectively.

The published theoretical studies on GUA in aqueous solution have focused on the calculation of absorption and emission spectra.[21,24,25,33–35] In most cases, the solvent was treated either explicitly using hybrid quantum mechanical–molecular mechanical (QM–MM) methods or implicitly by polarizable continuum models (PCM). In several studies, the influence of nearby water molecules and their hydrogen bonds was taken into account through supermolecular QM calculation on GUA–water clusters, sometimes combined with a PCM treatment of the surrounding bulk solvent.[21,24,25,35] One such example is the TDDFT/PCM calculations of GUA–water clusters that helped explain the pump–probe experiments on GMP.[21] On the dynamics side, there is one na-AIMD investigation (ROKS-BLYP) on the decay of GUA embedded in 60 water molecules, which reports the S_1 lifetime in aqueous solution being "roughly twice as long as for the gas phase", on the basis of 6 trajectories, which are considered insufficient by the authors "to obtain a meaningful statistically averaged result".[36]

In this article, we study the nonadiabatic dynamics of GUA in aqueous solution by surface-hopping simulations using a QM–MM approach. The QM–MM setup allows an explicit quantum mechanical treatment of the GUA molecule while the surrounding water molecules are represented by a classical force field. The nonadiabatic dynamics are followed using Tully's surface hopping method,[37] which is well established for studying molecules in a condensed phase or a biological environment.[38–42] The QM region is described by the OM2 orthogonalization-corrected semiempirical Hamiltonian[43] and multireference configuration interaction (MRCI).[44] The water molecules are modeled at the TIP3P level.[45] This setup has already been successfully applied for investigating the deexcitation of adenine in water.[46] Here, we have chosen to study 9*H*-guanine as the biologically most relevant tautomer of guanine.[28] It should be noted that the results from this work cannot necessarily be generalized to other GUA tautomers or derivatives, which may show different photoinduced dynamics.[27,28,30,47–53]

2 Computational details

The initial preparation of a GUA molecule embedded in its solvation sphere was done iteratively with the use of the CHARMM simulation package.[54] To start, a GUA molecule was placed at the center of an equilibrated sphere (radius 40 Å) of TIP3P water molecules.[45] All water molecules closer than 2.8 Å to the nucleobase were removed, and the radius of the water sphere was reduced to 30 Å by removing all more distant molecules. The system was then relaxed by a classical molecular dynamics (MD) run of 50 ps. This procedure was repeated five times to reach equilibrium. Finally, the radius of the solvation sphere was reduced to 20 Å, and water molecules further than 16 Å from the center were frozen. The active region thus included a GUA molecule (16 atoms) and 641 water molecules (1923 atoms), while all remaining water molecules (1359 atoms) were kept at fixed positions.

In the next step, the whole system was handled at the QM–MM level. The QM part (GUA) was treated by the semiempirical OM2/MRCI method, using the orthogonalization-corrected OM2 Hamiltonian[43] and multireference configuration interaction (MRCI) in the framework of the graphical unitary group approach (GUGA).[44] The options for the OM2/MRCI calculation were the same as in our previous work on gas-phase GUA,[31] with an active space built from five occupied and four unoccupied orbitals and with three reference configurations (MRCI). The self-consistent-field calculations were performed using the restricted open-shell Hartree–Fock formalism. The MM part (all water molecules) was described at the molecular mechanics level (TIP3P force field). The QM–MM interactions included standard van-der-Waals interactions (Lennard-Jones potentials) and electrostatic interactions (electronic embedding).[55] The QM–MM electronic Hamiltonian was used to calculate energies, gradients, and nonadiabatic couplings for the lowest singlet states. For this purpose, a development version of the simulation package ChemShell[56] was employed, which provides an adapted interface to the MNDO99 semiempirical code.[57]

The technical details of QM–MM surface-hopping calculations were completely analogous to those in our recent study on adenine in water (as documented in ref. 46). Briefly, a ground-state Born–Oppenheimer MD (BOMD) run was performed at 300 K for initial sampling. From this BOMD trajectory, 200 snapshots were chosen as input structures for computing the absorption spectrum from the corresponding vertical excitation energies and oscillator strengths. For the QM–MM surface-hopping dynamics, the selection of initial configurations was guided by the concept of obtaining an adequate approximate sampling of the absorption band, with the number of trajectories starting from a given configuration and excited state being determined from the corresponding oscillator strength.[46] In each QM–MM surface-hopping dynamics run, the nuclear trajectory was propagated for 6000 steps with a time step of 0.2 fs. The fewest switches algorithm[37,58] was employed to determine the hopping probabilities.

Two different sets of surface-hopping calculations were analyzed independently. In the first run (set A), 122 snapshots were selected by the initial sampling and excited to the first excited state (S_1). In the second run (set B), 100 snapshots were chosen and excited to the second excited state (S_2). A number of trajectories terminated during the propagation for technical reasons. The remaining 97 and 84 successful trajectories were taken into account for the analysis of the dynamics starting from the S_1 and S_2 state, respectively.

All relevant geometries (ground-state and excited-state minima, conical intersections) were optimized at the QM–MM level with the DL-FIND optimizer[59] implemented in ChemShell. Cartesian coordinates of optimized structures are given in the ESI.† It is well known[46] that the total energy of the full system is strongly influenced by the orientation of the surrounding water molecules, even if the optimized geometries of the QM part are similar. Therefore, a number of different snapshots (typically 5–20) were selected for optimization to take solvent fluctuations into account. For a given snapshot, all energies were evaluated relative to the ground-state minimum energy of that snapshot, and it was checked that the relevant optimized structures were linked to each other by continuous pathways. This meant in practice that excited-state minima were searched starting from optimized ground-state geometries and that ground-state optimizations starting from an optimized conical intersection structure were required to establish the associated ground-state geometry. The applied procedures are described in more detail in ref. 46.

3 Results

3.1 Potential energy surfaces

In the snapshots considered, the solvated GUA nucleobase is almost planar at the optimized ground-state minimum $(S_0)_{\min}$, with a very slight pyramidalization of the amino group (see Fig. 1). This is in good agreement with calculated gas-phase geometries[26,28] and with structures obtained for solvated GUA models.[35]

At the ground-state minima of different snapshots, the computed vertical excitation energies typically lie between 4.40–4.53 eV, 4.74–4.82 eV, and 5.73–5.80 eV for the first three transitions, see Table 1. These QM(OM2/MRCI)–MM values are roughly in the range of the vertical excitation energies calculated for GUA in water with a similar QM–MM setup, but in combination with high-level QM methods (TD-DFT and DFT/MRCI).[35] For example, the most reliable DFT/MRCI calculations with the largest basis set (TZVP + Ryd) yield mean values (50 snapshots) of 4.42, 4.98, and 5.37 eV, respectively, with standard deviations of 0.14–0.16 eV.[35] The differences between the

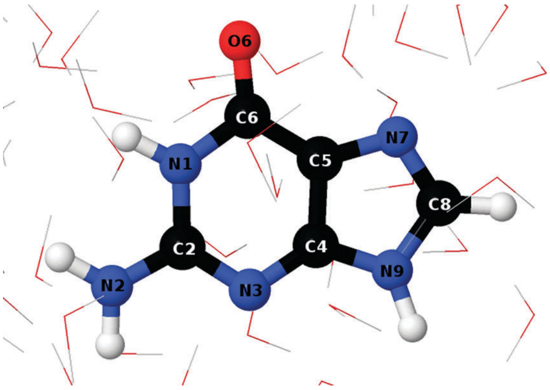

Fig. 1 Representative optimized geometry of the ground state of solvated GUA (with atom labels).

Table 1 Vertical excitation energies and oscillator strengths (in parentheses) at selected ground-state minima

Entry	State	ΔE_{vert}/eV (o.s.)	Character
1	S_1	4.44 (0.228)	L_a ($\pi\pi^*$)
	S_2	4.76 (0.294)	L_b ($\pi\pi^*$)
2	S_1	4.40 (0.231)	L_a ($\pi\pi^*$)
	S_2	4.75 (0.314)	L_b ($\pi\pi^*$)
3	S_1	4.46 (0.241)	L_a ($\pi\pi^*$)
	S_2	4.78 (0.272)	L_a ($\pi\pi^*$)
4	S_1	4.53 (0.219)	L_a ($\pi\pi^*$)
	S_2	4.82 (0.299)	L_b ($\pi\pi^*$)
5	S_1	4.53 (0.206)	L_a ($\pi\pi^*$)
	S_2	4.82 (0.294)	L_b ($\pi\pi^*$)
6	S_1	4.45 (0.233)	L_a ($\pi\pi^*$)
	S_2	4.74 (0.316)	L_b ($\pi\pi^*$)

OM2/MRCI and DFT/MRCI results are around 0.1–0.2 eV for the first two transitions and rise to about 0.4 eV for the third one (excitation to the dark nπ* state); this latter discrepancy is not so relevant at present, because our dynamics simulations (see below) will involve only the two lowest singlet excited states that are reasonably well described by OM2/MRCI. The calculated vertical excitation energies are also close to the experimental maxima of the first two bands at 4.51 and 5.04 eV.[15]

At the $(S_0)_{min}$ geometries, the S_1 and S_2 states are of ππ* L_a and ππ* L_b character, respectively. According to previous high-level work,[35] both these ππ* transitions of GUA are bright, in the gas phase as well as in aqueous solution, with the second one carrying notably more oscillator strength. The same qualitative trend is seen in the QM(OM2/MRCI)–MM oscillator strengths for the six selected snapshots in Table 1, with average values of 0.226 and 0.298 for the first two transitions. On this basis, one would expect the second absorption band to be somewhat stronger than the first one, as has indeed been observed in the experimental spectra of GUA in water[15] and GMP in water.[21] This is however not borne out by the theoretical QM(OM2/MRCI)–MM absorption spectrum generated from 200 snapshots of a ground-state MD run (see Fig. S1 of ESI†), which shows the expected double peak behavior, but with a somewhat stronger first band. This unexpected outcome may reflect the insufficient statistical sampling of only six snapshots in Table 1 and also the rather broad distribution of excitation energies of the bright S_2 state, which contributes to the intensity of the first band. We refrain from further analysis, since the precise profile of the absorption spectrum is not a central issue of this work.

Starting from the optimized ground-state S_0 geometries of different snapshots, we performed geometry optimizations for the first excited singlet state (S_1). In about 50% of the cases, we obtained geometries characterized by some ring distortion and a strong out-of-plane motion of the carbonyl oxygen atom, see panel a of Fig. 2 ($S_{1\alpha}$). The other half resulted in structures with more pronounced pure ring distortions, showing a more or less boat-like conformation of the six-membered ring, see panel b of Fig. 2 ($S_{1\beta}$). The optimized minimum-energy geometries $(S_0)_{min}$, $(S_{1\alpha})_{min}$, and $(S_{1\beta})_{min}$ mainly differ in certain key dihedral angles, which are close to 0° or 180° in the essentially planar ground state and may adopt quite different values in the nonplanar excited state. For example, the dihedral angles O6C6C5C4 and C6N1C2N2 (see Fig. 1 for atom labels) are normally around 110° and −15° for $(S_{1\alpha})_{min}$, and the dihedral angles N3C4C5C6 and C6N1C2N3 are typically around 20° and up to −50° for $(S_{1\beta})_{min}$. The latter structure $(S_{1\beta})_{min}$ is similar to the optimized gas-phase geometry of the first excited state previously obtained from OM2/GUGA-CI[31] as well as CASSCF[26] calculations. At both excited-state minima, the S_1 state is of L_a ππ* character, whereas the S_2 state is of mixed character (nπ* and different ππ* contributions).

We also tried to optimize the geometry of the second excited state (S_2) of GUA in water, starting from the optimized S_0 geometries of different snapshots. All these attempts were unsuccessful: the optimizations either did not converge or ended up at the S_1–S_2 conical intersection (CI_{12}).

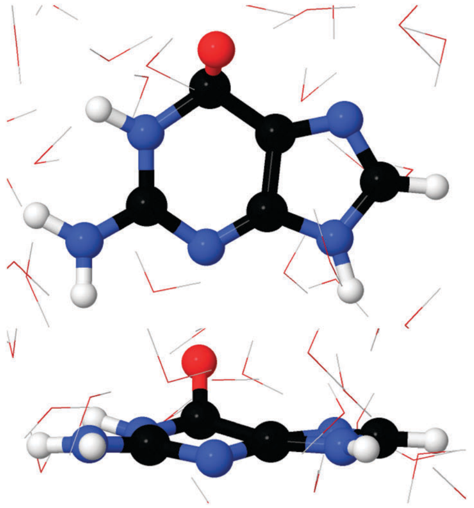

(a) $S_{1\alpha}$

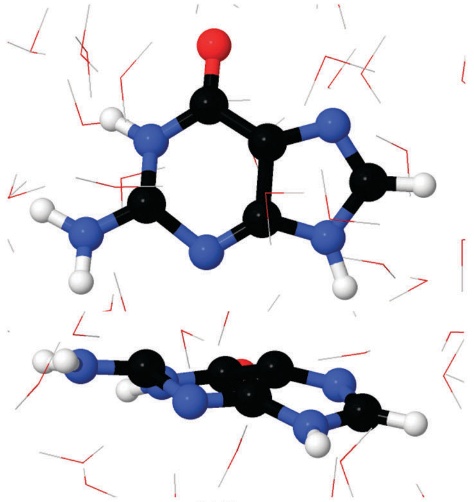

(b) $S_{1\beta}$

Fig. 2 Representative optimized geometries of the $S_{1\alpha}$ minimum (a) and the $S_{1\beta}$ minimum (b).

Three types of minimum-energy S_0–S_1 conical intersections (CI_{01}) could be located by optimizations starting from hopping structures obtained in the nonadiabatic dynamics simulations (see below). For each type, one representative optimized geometry is shown in Fig. 3. The $CI_{01\alpha}$ structures are characterized by a boat-like conformation of the six-membered ring. The $CI_{01\beta}$ geometries show a strong out-of-plane motion of the amino group, while the characteristic feature of $CI_{01\gamma}$ is a pronounced out-of-plane displacement of the carbonyl oxygen. In the latter two cases, essentially equivalent out-of-plane distortions are possible, either upwards or downwards. Ground-state geometry optimizations starting from the optimized CI_{01} structures led to the corresponding ground-state minimum in the case of $CI_{01\beta}$ and $CI_{01\gamma}$, which established their energy relative to the ground-state minimum (see Table 2). Analogous optimizations did not succeed for $CI_{01\alpha}$, and hence its relative energy could not be determined in this manner (thus missing in Table 2).

The same three types of S_0–S_1 conical intersections (CI_{01}) have been found in our previous OM2/MRCI study of GUA in the gas phase.[31] Likewise, three such types of conical

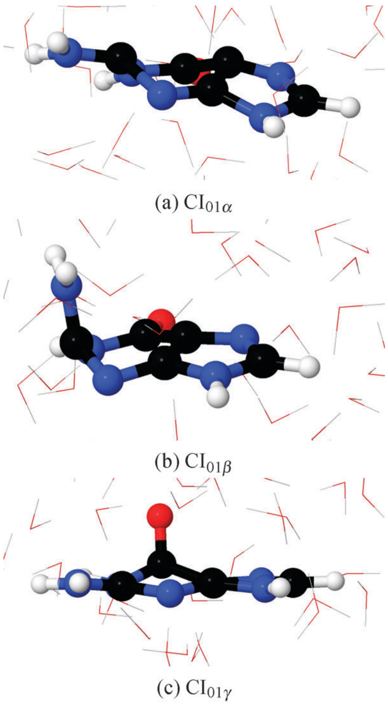
(a) $CI_{01\alpha}$

(b) $CI_{01\beta}$

(c) $CI_{01\gamma}$

Fig. 3 Representative optimized geometries for the three types of conical intersections connecting the ground and the first excited state (CI_{01}).

Table 2 Energies of optimized conical intersection structures (CI_{01} and CI_{12}) for different snapshots, relative to the corresponding ground-state energy minimum

Structure	State	Energies/eV
$CI_{01\beta}$	S_0/S_1	3.26, 3.53, 3.85
$CI_{01\gamma}$	S_0/S_1	3.32, 3.50, 3.59
CI_{12}	S_1/S_2	4.41, 4.41, 4.66

intersections have also been identified in a recent *ab initio* MRCIS/6-31G* investigation.[32] The optimized OM2/MRCI and MRCIS/6-31G* geometries in the gas phase appear to be quite similar for $CI_{01\beta}$, while those for $CI_{01\alpha}$ and $CI_{01\gamma}$ share the same qualitative features but are less distorted in the ring at the OM2/MRCI level (see ESI† for a more detailed comparison including graphical overlays of the optimized structures).

Comparing the three conical intersections (CI_{01}) with the ground-state minimum of GUA in water, the main changes in the optimized OM2/MRCI geometries are as follows. In $CI_{01\alpha}$ there is a distinct elongation of the C2–N3 bond by around 0.4 Å, and the dihedral angle C6N1C2N3 increases to around 50°. In $CI_{01\beta}$ the out-of-plane motion of the amino group causes a drastic change of the dihedral angle C6N1C2N2 to almost ±80°. In $CI_{01\gamma}$ there is a general shortening of bond lengths and widening of bond angles, but the most characteristic feature is the change of the dihedral angle O6C6C5C4 from around 180° to around ±90°.

The S_1–S_2 conical intersection CI_{12} can be reached by optimizations on the S_2 PES starting either from S_0 minimum structures or from $S_2 \rightarrow S_1$ hopping geometries. Both kinds of optimizations result in similar CI_{12} structures (see Fig. 4), which generally have a slightly distorted six-membered ring (most often in a boat-like fashion), sometimes accompanied by a slight out-of-plane motion of the amino group and/or carbonyl oxygen. The adiabatic energies of CI_{12} are generally close to the vertical energies of the S_1 state at the ground-state minimum geometries, see Tables 1 and 2.

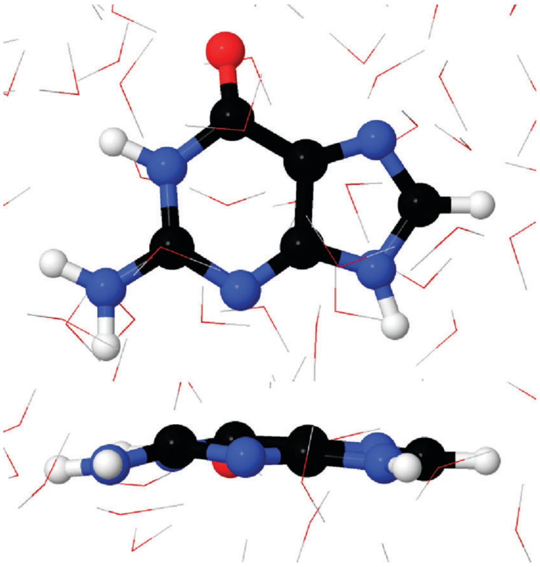
Fig. 4 Representative optimized geometry of the conical intersection between the first and second excited state (CI_{12}).

3.2 Nonadiabatic dynamics

No matter whether the surface hopping dynamics simulations in aqueous solution are started from the S_1 or S_2 state, we find ultrafast internal conversion to the electronic ground state of GUA. Fig. 5 shows the average occupation of the adiabatic states as a function of time.

For the nonadiabatic dynamics starting from the S_1 state (set A), the deexcitation can be described as an exponential decay:

$$f(t) = f_0 + (1 - f_0)e^{-\frac{t-t_0}{\tau}} \qquad (1)$$

where f_0 is the fraction of the population remaining in the S_1 state at the end of the simulation, t_0 is the time when the exponential decay sets in, and τ is the corresponding decay constant. The fitting results in t_0 = 37 fs and τ = 277 fs. Hence the lifetime of the S_1 state is 314 fs (the sum of t_0 and τ). After 1.2 ps there is still a fraction of about 6% in the S_1 state.

For the nonadiabatic dynamics starting from the S_2 state (set B), the two subsequent decays can be described by

$$f(t) \propto \frac{\tau_2}{\tau_1 - \tau_2}\left(e^{-\frac{t}{\tau_1}} - e^{-\frac{t}{\tau_2}}\right) \qquad (2)$$

where τ_1 and τ_2 refer to the decay constants for the deexcitation from S_2 to S_1 and τ_2 from S_1 to S_0, respectively. The fitting yields τ_1 = 20 fs and τ_2 = 248 fs. The decay from the S_2 state is completed within 60 fs, and after 1.2 ps only 1% of the population remains in the S_1 state.

The overall deexcitation to the ground state is obviously slightly faster when starting from the S_2 rather than the S_1 state. This can be attributed to the higher initial energy that is available after excitation to the S_2 state, which results in faster nuclear motion and allows the molecule to reach the S_0–S_1

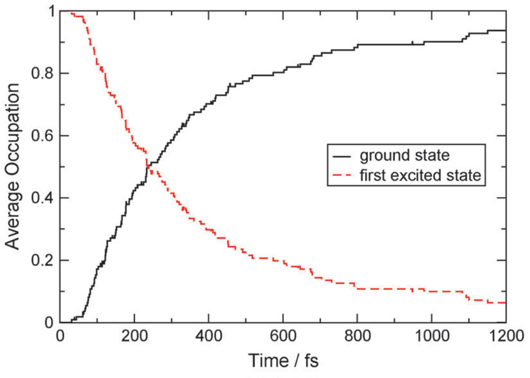

(a) Set A

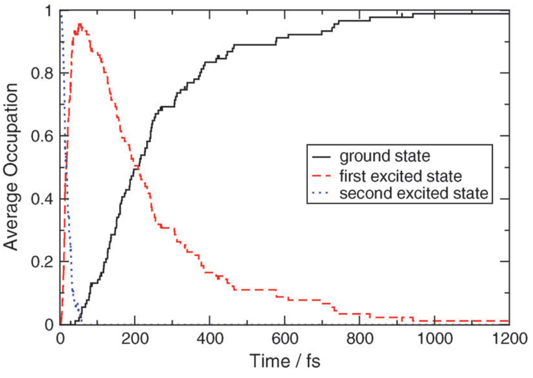

(b) Set B

Fig. 5 Occupation of the low-lying adiabatic states after initial excitation to the S_1 state (set A) and the S_2 state (set B) as a function of simulation time.

conical intersection more quickly. In addition, the higher nuclear velocity enhances the nonadiabatic coupling term (the dot product between the nonadiabatic coupling vector and the nuclear velocity vector) and thus leads to a higher hopping probability for the nonadiabatic $S_1 \rightarrow S_0$ transition.

The average $S_2 \rightarrow S_1$ hopping time is computed to be 21 fs. The geometries at the hopping event are almost planar with slight distortions of the ring system, sometimes in a boat-like conformation or with a slight out-of-plane motion of the amino group and/or the carbonyl oxygen. Five of these hopping structures were selected for geometry optimization on the S_2 PES, which yielded CI_{12} geometries quite similar to the initial hopping structures.

Regardless of whether the nonadiabatic dynamics were started in the S_1 or S_2 state (sets A and B), four groups of hopping structures were found for the $S_1 \rightarrow S_0$ internal conversion. The characteristic features of these four groups are (a) the distortion of the six-membered ring in a boat-like manner, (b) the out-of-plane motion of the amino group, (c) the out-of-plane displacement of the carbonyl oxygen, and (d) the overall distortion of the aromatic ring system. One representative example of each group is displayed in Fig. 6. The corresponding average hopping times are given in Table 3 for both sets separately.

Around a dozen hopping structures of each group from set A (in total 50) were chosen as input for CI_{01} geometry optimization. More than half of these (28) converged to a conical intersection structure. As already mentioned above, three types of minimum-energy conical intersections were found in this manner for GUA in water (see Fig. 3). When starting from hopping structures with a distorted boat-like six-membered ring, the optimization either failed or reached $CI_{01\alpha}$. Optimizations of hopping structures with an out-of-plane amino group or carbonyl oxygen most often succeeded and arrived at the corresponding conical intersection, *i.e.*, $CI_{01\beta}$ or $CI_{01\gamma}$, respectively. Optimizations of hopping structures from the last group (with distorted rings) mostly crashed or led to $CI_{01\gamma}$, *i.e.* no fourth type of conical intersection geometry could be identified in this manner.

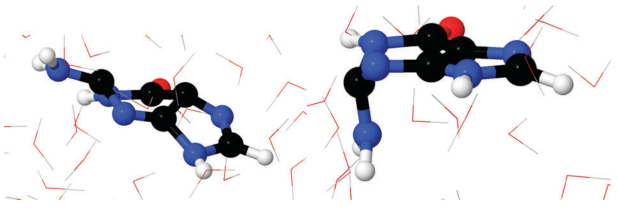

(a) boat conformation (b) NH_2 oop

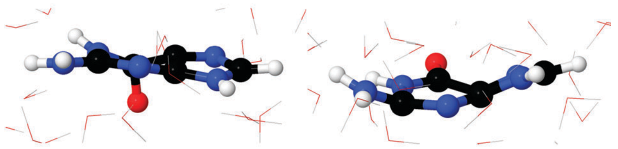

(c) O oop (d) plane distorted

Fig. 6 Representative examples for the four groups of $S_1 \rightarrow S_0$ hopping structures for GUA in water.

Table 3 Characteristics, occurrences, and average hopping times of different types of $S_1 \rightarrow S_0$ hopping structures for GUA in water

	Set A		Set B	
Characteristics	Occ.	Hopping time/fs	Occ.	Hopping time/fs
Boatlike ($CI_{01\alpha}$)	26	343	8	395
NH_2 oop ($CI_{01\beta}$)	13	441	6	517
O oop ($CI_{01\gamma}$)	41	265	60	216
Distortion of rings	17	224	10	140

4 Discussion

4.1 Solvent effects on static properties

At the OM2/MRCI level, the ground-state geometry of GUA is completely planar in the gas phase,[31] while a slight pyramidalization of the amino group occurs in aqueous solution. The presence of the solvent does not change the electronic character of the three lowest-lying singlet excited states of GUA in OM2/MRCI ($L_a < L_b < n\pi^*$), but there are some shifts in the computed vertical excitation energies. For the first electronic excited state (L_a), the gas-phase value[31] of 4.26 eV is blue-shifted by about 0.2 eV in aqueous solution, see Table 1. For the second state (L_b), OM2/MRCI gives a vertical excitation energy of 4.99 eV in the gas phase, which is reduced by about 0.2 eV in solution. In OM2/MRCI, the L_a–L_b energy gap thus becomes smaller for solvated GUA, but it remains sizable (around 0.3 eV), and there is no strong mixing of electronic character. For the third state ($n\pi^*$), OM2/MRCI predicts a strong blue shift of about 0.4 eV, from 5.33 eV in the gas phase to 5.73–5.80 eV for solvated GUA. This high-lying dark $n\pi^*$ state is not considered at all in the present dynamics simulations, which cover only the two lowest singlet excited states. The solvent-induced shifts of the vertical excitation energies from OM2/MRCI may be compared with those obtained with higher-level QM methods in our previous work:[35] the DFT/MRCI-based calculations afford shifts of the same direction and of similar magnitude in the case of the L_b and $n\pi^*$ states, but a red rather than a blue shift for the L_a state. According to our previous analysis,[35] various counteracting factors influence these shifts, and it is thus difficult to pinpoint the reasons for the discrepancies in the L_a case. We do not attempt to do this here because the shifts are not in the focus of our present work.

In our standard procedure, geometry optimizations of the S_1 state always start from ground-state minimum-energy geometries. In the gas phase, this invariably leads to a GUA minimum ($S_{1\beta}$) with a boat-like distortion of the six-membered ring.[31] In water, only half of the optimizations reach this minimum, while the others end up at a different minimum ($S_{1\alpha}$) with a notable out-of-plane motion of the oxygen atom, see Fig. 2. This strongly suggests that the out-of-plane motion of the carbonyl oxygen may be involved in the excited-state dynamics of GUA in water. Re-optimizing an $S_{1\alpha}$ structure obtained in aqueous solution without the solvent molecules yields a similar second S_1 minimum also in the gas phase, which is structurally and energetically close to the corresponding conical intersection ($CI_{01\gamma}$) in the gas phase, with an energy gap between the lowest singlet states of only 0.04 eV at this S_1 minimum geometry. Hence, an S_1 minimum with an out-of-plane carbonyl oxygen exists on the OM2/MRCI surface both in the gas phase and in aqueous solution, with a similar structure and in both cases close to the related conical intersection.

4.2 Solvent effects on the dynamics

Our previous OM2/MRCI work on the nonadiabatic dynamics of GUA in the gas phase revealed two distinct $S_1 \rightarrow S_0$ decay pathways *via* $CI_{01\alpha}$ and $CI_{01\beta}$ with average hopping times of 190 fs and 400 fs, respectively.[31] The current QM(OM2/MRCI)–MM simulations show that the overall internal conversion becomes slightly faster for GUA in aqueous solution (see Table 3). More important than this slight acceleration measured in aqueous solution using the semiempirical setup is the observation that the decay mechanism is modulated by the water environment. In the gas phase, the conical intersections $CI_{01\alpha}$ and $CI_{01\beta}$ dominate the nonadiabatic dynamics of GUA.[31,32] In contrast, in aqueous solution, the $CI_{01\alpha}$ channel is much less important, and the $CI_{01\beta}$ channel is also suppressed to a certain degree, while a new deexcitation pathway *via* $CI_{01\gamma}$ emerges and actually becomes dominant (see Table 3).

To examine the reason for this change in the decay mechanism, we have checked the gradient of the S_1 state in the Franck–Condon (FC) region for all initial geometries of the nonadiabatic dynamics trajectories. The gradient components perpendicular to the molecular plane at the N2 and O6 atoms are indicative for the propensity to out-of-plane motion towards $CI_{01\beta}$ and $CI_{01\gamma}$, respectively. Their norms are plotted in Fig. 7 and average values are given in Table 4 for 85 trajectories of GUA both in the gas phase and in water. In the gas phase, the S_1 gradient is larger at the N2 atom than at the O6 atom (on average by 35%), consistent with the observed dynamic preference for out-of-plane motion of the N2 atom (amino group).[31] In water, the S_1 gradient remains almost unchanged at the N2 atom (rising on average by 10%) but increases strongly at the O6 atom (typically by a factor of 2), thus favoring the out-of-plane motion of the carbonyl oxygen towards $CI_{01\gamma}$. It is plausible that this increase in the S_1 gradient in the FC region is responsible for the slightly faster overall decay dynamics in our simulations and the emergence of the new dominant decay channel *via* $CI_{01\gamma}$. Hydrogen bonding in aqueous solution may well cause these differences, since one would expect qualitatively that the O6 atom will form strong hydrogen bonds with water molecules above and below the molecular plane, which could assist the out-of-plane distortion of the O6 atom towards $CI_{01\gamma}$. We have tried to find quantitative evidence to support this notion, for example by tracking the minimum distance from O6 to the closest hydrogen atom in the surrounding water molecules during the trajectories and at the surface hopping events as well as at the excited-state minima and the conical intersections, but the resulting differences seem too small to be conclusive (see ESI† for detailed data).

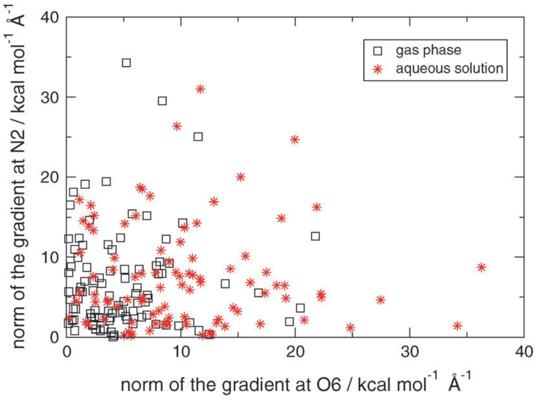

Fig. 7 Norms of the S_1 gradient components perpendicular to the molecular plane at atoms O6 and N2, respectively, for GUA in the gas phase (squares) and in aqueous solution (stars).

Table 4 Norms of the S_1 gradient components perpendicular to the molecular plane at atoms O6 and N2, respectively, for GUA in the gas phase and in aqueous solution, given in kcal mol^{-1} Å^{-1}

Gradient at	Gas phase	Aqueous solution
N2	6.77	7.47
O6	5.00	10.25

4.3 Accuracy issues

Since the current work is based on the semiempirical OM2/MRCI method, it is worthwhile to comment on its accuracy and reliability. This has already been done in some detail in our recent work on adenine in water,[46] and therefore we only present some brief remarks here on the general performance of

OM2/MRCI in excited-state calculations, before addressing the present target system (GUA in water).

We have performed extensive benchmark calculations on the electronically excited states of medium-sized organic molecules to examine the performance of various state-of-the-art electronic structure methods.[60–63] These studies show that it is very difficult to accurately describe the excited-state properties of such molecules. Compared with our theoretical best estimates for vertical excitation energies, standard published CASPT2 calculations gave mean absolute deviations (MAD) of about 0.3 eV.[60,63] The errors of the TDDFT results depended on the chosen functional, of course, with MAD values typically in the range of 0.3–0.5 eV.[61] Among the tested semiempirical methods, the orthogonalization-corrected approaches such as OM2/MRCI showed the best performance, with MAD values of 0.4–0.5 eV, while being orders of magnitude faster than standard *ab initio* and TDDFT methods.[62] Generally speaking, OM2/MRCI thus seems to provide a balanced compromise between accuracy and computational cost, which justifies its application in excited-state work on medium- and large-sized molecules. Of course, it is always advisable to perform a specific validation for the target system at hand; this has already been achieved in our previous study on GUA in the gas phase, which showed the relevant OM2/MRCI geometries and energies to be consistent with those from high-level calculations.[31]

Considering our present target, GUA in water, we note that our QM–MM results (QM = OM2/MRCI) for the vertical excitation energies compare reasonably well with the values obtained from higher-level QM–MM approaches (QM = TDDFT, DFT/MRCI) and from calculations with continuum solvation models (see Section 3.1).[25,33,35] There is also reasonable agreement with experiment: for typical snapshots, the first two transitions are computed to lie between 4.40–4.53 eV and 4.74–4.82 eV, respectively, while the experimental band maxima are reported at 4.51 and 5.04 eV.[15] Moreover, the influence of the solvent on the oscillator strength is qualitatively well reproduced at the QM–MM (QM = OM2/MRCI) level. For gas-phase GUA, the oscillator strength of the S_1 state (L_a) is much larger than that of the S_2 state (L_b).[31,32] In aqueous solution, this is reversed since the S_2 state (L_b) now has the larger transition dipole moment, as shown by the present and previous calculations[33,35] as well as by experiment.[21]

For the excited-state dynamics, conical intersections are of crucial importance. Here we can compare the OM2/MRCI results for GUA only with other computational results in the gas phase. Both OM2/MRCI and the applied *ab initio* methods identify three minimum-energy S_1–S_0 conical intersection structures (see Section 3.1). $CI_{01\beta}$ is always characterized by an out-of-plane amino group, with the OM2/MRCI geometry closely resembling the structures found at the CASSCF/CASPT2 and MRCIS levels.[26,28–32] In the case of $CI_{01\gamma}$, all computational methods predict a strong out-of-plane displacement of the carbonyl oxygen atom; the high-level methods also give a significant distortion of the six-membered ring,[26,28–30,32] more so than OM2/MRCI where this ring is closer to planarity. At the OM2/MRCI level, $CI_{01\alpha}$ shows a boat-like distortion of the six-membered ring, with rather weak deformations of the ring and the amino group,[31] whereas there are more pronounced distortions at the CASSCF/CASPT2 and MRCIS levels.[29,30,32] Overall, there are thus a number of common qualitative features in the computed S_1–S_0 conical intersection structures, but also some distinct quantitative differences (see ESI† for detailed data and graphical overlays of optimized structures).

A similar assessment is reached when we compare the results from our OM2/MRCI dynamics simulations for gas-phase GUA with those from a subsequent *ab initio* MRCIS/6-31G* study.[32] Both investigations agree that there is an ultrafast S_1–S_0 internal conversion, with time constants of a few hundred femtoseconds, and that the decay occurs mainly through the $CI_{01\alpha}$ and $CI_{01\beta}$ channels, which accounts for 95–100% of the population transfer. Not surprisingly, there are however also some quantitative deviations in the computed time constants and branching ratios for gas-phase GUA (see Section 3.2).

On the basis of these comparisons, we believe that OM2/MRCI provides a realistic description of the excited states of GUA and of the topology of the relevant potential energy surfaces. We note in this context that the QM–MM ground-state optimizations of GUA in aqueous solution yield minima with 6–7 water molecules hydrogen-bonded to GUA, in reasonable agreement with recent ground-state AIMD (BLYP) simulations of GUA in water[64] (for more details see ESI†). We believe that OM2/MRCI is capable of capturing the effects of the surrounding solvent water molecules on the excited-state dynamics of GUA in a QM–MM framework, in analogy to our previous work on adenine in water.[46] Technically, we can afford to treat the nonadiabatic dynamics of such large solvated systems, using extensive sampling of phase space and a large number of trajectory calculations, because of the high computational efficiency of the OM2/MRCI method (also in a QM–MM framework).

4.4 Comparison with experimental lifetimes

There is only one experimental study on the nonadiabatic dynamics of GUA in aqueous solution,[15] probably because of the low solubility of GUA in water, which reports excited-state lifetimes of GUA and its derivatives GUO and GMP between 4 and 5 ps.[15] These rather long lifetimes reflect the limitations of laser technology in earlier years so that it would be misleading to compare them with our current results.

More recently, several groups have examined the nonadiabatic dynamics of GUA derivatives in water using advanced pump–probe laser systems.[16–21] These studies targeted ribose and monophosphate derivatives such as GUO,[16–18] GMP,[18,21] dGUO,[19,20] and dGMP[19,20] (see Table S4 of ESI† for a detailed survey). They arrived at sub-picosecond S_1 lifetimes (0.4 ps–0.9 ps) that are somewhat longer than our calculated average value for GUA in water (0.31 ps), but still of the same order of magnitude. The discrepancy might partly be due to the substituents at the N9 atom that are present in the experimental work. We note in this context that gas-phase na-AIMD (ROKS) calculations on the dynamics of 9-methyl-substituted guanine gave lifetimes that are longer than those obtained with the same technique for unsubstituted GUA[50–52] (see also Table S4 of ESI†). Furthermore, upon introduction of a monophosphate group (*i.e.* when going from GUO to GMP or from dGUO to dGMP), the experimentally observed lifetimes increase by about 0.1–0.2 ps.[18,19] In view of such substituent effects, we consider our calculated value for the S_1 lifetime of GUA in water as a reasonable estimate. Future theoretical studies of substituent effects are desirable.

Finally, we mention again that na-AIMD (ROKS) simulations of GUA embedded in 60 water molecules indicate that the S_1 lifetime of GUA in aqueous solution is "roughly twice as long as for the gas phase" (*i.e.* of the order of 2 ps),[36] which is significantly larger than the present OM2/MRCI value of 0.31 ps and the quoted recent experimental values of 0.4 ps–0.9 ps (see above). Since the na-AIMD (ROKS) estimate is based on only 6 trajectories and thus statistically not meaningful,[36] we refrain from further comparisons.

5 Conclusion

We have investigated the nonadiabatic dynamics of 9*H*-GUA in aqueous solution using a semiempirical QM–MM approach (QM = OM2/MRCI, MM = TIP3P). We performed geometry optimizations on a large number of snapshots to locate the relevant ground-state and excited-state minima as well as the conical intersections connecting them. Surface hopping trajectory simulations were carried out to examine the deexcitation mechanisms for returning to the ground state in detail.

The optimized geometries of GUA in water closely resemble those in the gas phase, both for the minima and the conical intersections. The electronic characters of the first three excited singlet states do not change much at the OM2/MRCI level when going from the gas phase to aqueous solution, although there are notable solvent-induced shifts in the computed vertical excitation energies (up to about 0.4 eV). Overall, the results from these static OM2/MRCI-based calculations are in reasonable agreement with the available *ab initio* and experimental data.

In the dynamics simulations, we find ultrafast nonradiative decay for GUA in water. The excited-state lifetime is 0.31 ps for the trajectories starting from the S_1 state. When starting from the S_2 state, the $S_2 \rightarrow S_1$ and $S_1 \rightarrow S_0$ internal conversions take place with time constants of around 20 fs and 0.25 ps, respectively. Compared with GUA in the gas phase, the overall decay is slightly faster in water. More importantly, the $S_1 \rightarrow S_0$ internal conversion is predicted to proceed *via* different channels. In the gas phase, the dominant pathways pass through the region of the conical intersections $CI_{01\alpha}$ (ring distortion) and $CI_{01\beta}$ (out-of-plane displacement of the amino group), while $CI_{01\gamma}$ (out-of-plane motion of the carbonyl oxygen atom) does not play any significant role. In aqueous solution, in contrast, the latter channel becomes dominant according to our simulations, while the two former ones are both suppressed and contribute less. This change in the mechanistic scenario has been analyzed in terms of the topology of the excited-state surface and the influence of the solvent water molecules.

Acknowledgements

This work has been supported by the Volkswagenstiftung. The authors thank Dr Mario Barbatti, You Lu, and Dr Oliver Weingart for many helpful discussions. ZL is grateful for the partial support from the 100 Talent Project of CAS, from NSFC (No. 21103213) and from the Director Innovation Foundation of the QIBEBT of CAS.

References

1 P. R. Callis, *Annu. Rev. Phys. Chem.*, 1983, **34**, 329–357.
2 C. E. Crespo-Hernández, B. Cohen, P. M. Hare and B. Kohler, *Chem. Rev.*, 2004, **104**, 1977–2019.
3 H. Saigusa, *J. Photochem. Photobiol., C*, 2006, **7**, 197–210.
4 C. T. Middleton, K. de La Harpe, C. Su, Y. K. Law, C. E. Crespo-Hernández and B. Kohler, *Annu. Rev. Phys. Chem.*, 2009, **60**, 217–239.
5 B. Kohler, *J. Phys. Chem. Lett.*, 2010, **1**, 2047–2053.
6 T. Gustavsson, A. Banyasz and D. Markovitsi, *J. Phys.: Conf. Ser.*, 2011, **261**, 012009.
7 M. Daniels and W. Hauswirth, *Science*, 1971, **171**, 675–677.
8 D. N. Nikogosyan, D. A. Angelov and A. A. Oraevsky, *Photochem. Photobiol.*, 1982, **35**, 627–635.
9 J.-P. Ballini, M. Daniels and P. Vigny, *J. Lumin.*, 1983, **27**, 389–400.
10 T. Häupl, C. Windolph, T. Jochum, O. Brede and R. Hermann, *Chem. Phys. Lett.*, 1997, **280**, 520–524.
11 C. Canuel, M. Mons, F. Piuzzi, B. Tardivel, I. Dimicoli and M. Elhanine, *J. Chem. Phys.*, 2005, **122**, 074316.
12 *Conical Intersections: Electronic Structure, Dynamics and Spectroscopy*, ed. W. Domcke, D. R. Yarkony and H. Köppel, World Scientific Publishing Co, 2004.
13 *Radiation Induced Molecular Phenomena in Nucleic Acids: A Comprehensive Theoretical and Experimental Analysis*, ed. M. Shukla and J. Leszczynski, Springer Verlag, 2008.
14 H. Kang, K. T. Lee, B. Jung, Y. J. Ko and S. K. Kim, *J. Am. Chem. Soc.*, 2002, **124**, 12958–12959.
15 T. Fujiwara, Y. Kamoshida, R. Morita and M. Yamashita, *J. Photochem. Photobiol., B*, 1997, **41**, 114–121.
16 J.-M. L. Pecourt, J. Peon and B. Kohler, *J. Am. Chem. Soc.*, 2000, **122**, 9348–9349.
17 J.-M. L. Pecourt, J. Peon and B. Kohler, *J. Am. Chem. Soc.*, 2001, **123**, 10370–10378.
18 J. Peon and A. H. Zewail, *Chem. Phys. Lett.*, 2001, **348**, 255–262.
19 D. Onidas, D. Markovitsi, S. Marguet, A. Sharonov and T. Gustavsson, *J. Phys. Chem. B*, 2002, **106**, 11367–11374.
20 F.-A. Miannay, T. Gustavsson, A. Banyasz and D. Markovitsi, *J. Phys. Chem. A*, 2010, **114**, 3256–3263.
21 V. Karunakaran, K. Kleinermanns, R. Improta and S. A. Kovalenko, *J. Am. Chem. Soc.*, 2009, **131**, 5839–5850.
22 M. P. Fülscher, L. Serrano-Andrés and B. O. Roos, *J. Am. Chem. Soc.*, 1997, **119**, 6168–6176.
23 R. Santamaria and A. Vázquez, *J. Comput. Chem.*, 1994, **15**, 981–996.
24 M. K. Shukla and J. Leszczynski, *J. Biomol. Struct. Dyn.*, 2007, **25**, 93–118.
25 M. K. Shukla and J. Leszczynski, *J. Phys. Chem. B*, 2008, **112**, 5139–5152.
26 H. Chen and S. Li, *J. Chem. Phys.*, 2006, **124**, 154315.
27 H. Langer and N. L. Doltsinis, *J. Chem. Phys.*, 2003, **118**, 5400–5407.
28 C. M. Marian, *J. Phys. Chem. A*, 2007, **111**, 1545–1553.
29 L. Serrano-Andrés, M. Merchán and A. C. Borin, *J. Am. Chem. Soc.*, 2008, **130**, 2473–2484.
30 S. Yamazaki, W. Domcke and A. L. Sobolewski, *J. Phys. Chem. A*, 2008, **112**, 11965–11968.
31 Z. Lan, E. Fabiano and W. Thiel, *ChemPhysChem*, 2009, **10**, 1225–1229.
32 M. Barbatti, J. J. Szymczak, A. J. A. Aquino, D. Nachtigallová and H. Lischka, *J. Chem. Phys.*, 2011, **134**, 014304.
33 B. Mennucci, A. Toniolo and J. Tomasi, *J. Phys. Chem. A*, 2001, **105**, 7126–7134.
34 K. Kowalski and M. Valiev, *Res. Lett. Phys. Chem.*, 2007, **2007**, 1–5.
35 M. Parac, M. Doerr, C. M. Marian and W. Thiel, *J. Comput. Chem.*, 2009, **31**, 90–106.
36 N. L. Doltsinis, P. R. L. Markwick, H. Nieber and H. Langer, Ultrafast Radiationless Decay in Nucleic Acids: Insights from

Nonadiabatic *ab initio* Molecular Dynamics, in *Radiation Induced Molecular Phenomena in Nucleic Acids*, ed. M. K. Shukla and J. Leszczynski, Springer, 2008, pp. 265–299.
37 J. C. Tully, *J. Chem. Phys.*, 1990, **93**, 1061–1071.
38 H. M. Senn and W. Thiel, *Angew. Chem., Int. Ed.*, 2009, **48**, 1198–1229.
39 G. Groenhof, L. V. Schäfer, M. Boggio-Pasqua, M. Goette, H. Grubmüller and M. A. Robb, *J. Am. Chem. Soc.*, 2007, **129**, 6812–6819.
40 P. Cattaneo, M. Persico and A. Tani, *Chem. Phys.*, 1999, **246**, 315–322.
41 M. Persico, G. Granucci, S. Inglese, T. Laino and A. Toniolo, *THEOCHEM*, 2003, **621**, 119–126.
42 M. Barbatti, *Wiley Interdiscip. Rev.: Comput. Mol. Sci.*, 2011, **1**, 620–633.
43 W. Weber and W. Thiel, *Theor. Chem. Acc.*, 2000, **103**, 495–506.
44 A. Koslowski, M. E. Beck and W. Thiel, *J. Comput. Chem.*, 2002, **24**, 714–726.
45 W. L. Jorgensen, J. Chandrasekhar, J. D. Madura, R. W. Impey and M. L. Klein, *J. Chem. Phys.*, 1983, **79**, 926–935.
46 Z. Lan, Y. Lu, E. Fabiano and W. Thiel, *ChemPhysChem*, 2011, **12**, 1989–1998.
47 M. Mons, I. Dimicoli, F. Piuzzi, B. Tardivel and M. Elhanine, *J. Phys. Chem. A*, 2002, **106**, 5088–5094.
48 K. Seefeld, R. Brause, T. Häber and K. Kleinermanns, *J. Phys. Chem. A*, 2007, **111**, 6217–6221.
49 M. K. Shukla and J. Leszczynski, *Chem. Phys. Lett.*, 2006, **429**, 261–265.
50 H. Langer and N. L. Doltsinis, *Phys. Chem. Chem. Phys.*, 2003, **5**, 4516.
51 H. Langer and N. L. Doltsinis, *Phys. Chem. Chem. Phys.*, 2004, **6**, 2742.
52 H. Langer, N. L. Doltsinis and D. Marx, *ChemPhysChem*, 2005, **6**, 1734–1737.
53 S. Yamazaki and W. Domcke, *J. Phys. Chem. A*, 2008, **112**, 7090–7097.
54 B. R. Brooks, R. E. Bruccoleri, B. D. Olafson, D. J. States, S. Swaminathan and M. Karplus, *J. Comput. Chem.*, 1983, **4**, 187–217.
55 J. Kästner, S. Thiel, H. M. Senn, P. Sherwood and W. Thiel, *J. Chem. Theor. Comput.*, 2007, **3**, 1064–1072.
56 P. Sherwood, A. H. de Vries, M. F. Guest, G. Schreckenbach, C. R. A. Catlow, S. A. French, A. A. Sokol, S. T. Bromley, W. Thiel, A. J. Turner, S. Billeter, F. Terstegen, S. Thiel, J. Kendrick, S. C. Rogers, J. Casci, M. Watson, F. King, E. Karlsen, M. Sjvoll, A. Fahmi, A. Schäfer and C. Lennartz, *THEOCHEM*, 2003, **632**, 1.
57 W. Thiel, *MNDO program, version 6.1*, Mülheim, 2007.
58 E. Fabiano, T. W. Keal and W. Thiel, *Chem. Phys.*, 2008, **349**, 334–347.
59 J. Kästner, J. M. Carr, T. W. Keal, W. Thiel, A. Wander and P. Sherwood, *J. Phys. Chem. A*, 2009, **113**, 11856–11865.
60 M. Schreiber, M. R. da Silva-Junior, S. P. A. Sauer and W. Thiel, *J. Chem. Phys.*, 2008, **128**, 134110.
61 M. R. da Silva-Junior, M. Schreiber, S. P. A. Sauer and W. Thiel, *J. Chem. Phys.*, 2008, **129**, 104103.
62 M. R. da Silva-Junior and W. Thiel, *J. Chem. Theor. Comput.*, 2010, **6**, 1546–1564.
63 M. R. da Silva-Junior, M. Schreiber, S. P. A. Sauer and W. Thiel, *J. Chem. Phys.*, 2010, **133**, 174318.
64 A. Furmanchuk, O. Isayev, O. V. Shishkin, L. Gorb and J. Leszczynski, *Phys. Chem. Chem. Phys.*, 2010, **12**, 3363–3375.

Appendix B

Excited-States Dynamics of Guanosine in Aqueous Solution Revealed by Time-Resolved Photoelectron Spectroscopy: Experiment and Theory

Franziska Buchner, **Berit Heggen**, Hans-Hermann Ritze, Walter Thiel and Andrea Lübcke

Phys. Chem. Chem. Phys., **2015**, 17, 31978 – 31987.

Carried out and analyzed the calculations of 9*H*-guanine in aqueous solution for the evaluation of the ionization potential along the decay pathways.

PCCP

PAPER

View Article Online
View Journal | View Issue

Cite this: *Phys. Chem. Chem. Phys.*, 2015, **17**, 31978

Received 27th July 2015,
Accepted 2nd November 2015

DOI: 10.1039/c5cp04394h

www.rsc.org/pccp

Excited-state dynamics of guanosine in aqueous solution revealed by time-resolved photoelectron spectroscopy: experiment and theory†

Franziska Buchner,[a] Berit Heggen,[b] Hans-Hermann Ritze,[a] Walter Thiel[b] and Andrea Lübcke*[a]

Time-resolved photoelectron spectroscopy is performed on aqueous guanosine solution to study its excited-state relaxation dynamics. Experimental results are complemented by surface hopping dynamic simulations and evaluation of the excited-state ionization energy by Koopmans' theorem. Two alternative models for the relaxation dynamics are discussed. The experimentally observed excited-state lifetime is about 2.5 ps if the molecule is excited at 266 nm and about 1.1 ps if the molecule is excited at 238 nm. The experimental probe photon energy dependence of the photoelectron kinetic energy distribution suggests that the probe step is not vertical and involves a doubly-excited autoionizing state.

1 Introduction

Although DNA bases strongly absorb UV light, they are astonishingly photostable, which is the basis for the photostability of DNA, itself. The key to this photostability is their ultrafast, radiationless excited-state decay, which involves non-adiabatic processes at conical intersections. This general picture is widely accepted, although the detailed relaxation processes of individual DNA bases are not yet fully resolved. The excited-state relaxation of guanine (Gua) or its derivatives has been investigated experimentally both in the gas phase and the solution phase. In the gas phase, photoelectron imaging[1] and photoionization[2,3] were used, while in the solution phase transient absorption[4] and fluorescence up-conversion[5,6] were the techniques of choice. With the recent development of time-resolved liquid jet photoelectron spectroscopy, a new technique is at hand for investigating the solution phase excited-state dynamics. We have recently applied this technique to study the excited-state dynamics of adenine and adenosine (Ade/Ado)[7] as well as thymine and thymidine (Thy/Thd)[8] and demonstrated the potential of this technique for investigation of the excited-state dynamics of solvated molecules. In the present work, we investigate the excited-state dynamics of guanosine (Guo), the nucleoside of Gua, by time-resolved liquid jet photoelectron spectroscopy. The chemical structures of the relevant species are given in Fig. 1.

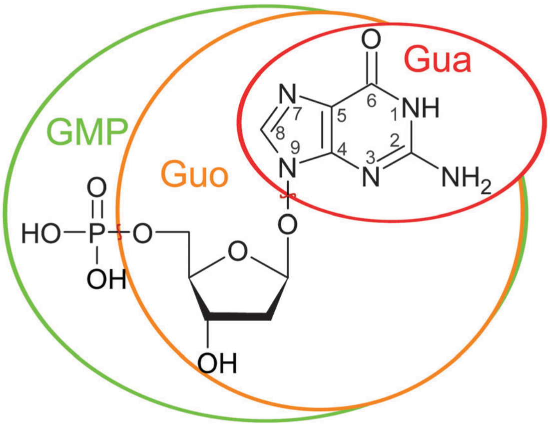

Fig. 1 Chemical structure of the DNA base guanine (Gua), its nucleoside guanosine (Guo), and its nucleotide guanosine monophosphate (GMP). In Gua and Guo, the missing groups are replaced by a hydrogen atom.

The optical absorption spectrum of Gua is dominated by two bright $\pi\pi^*$ transitions usually labeled as L_a and L_b. There are two dark states close to L_b in the gas phase, one of $n\pi^*$ character and one of $\pi\sigma^*$ character. There is quite large variation between different theoretical methods in describing how hydration affects the individual electronic states (see ref. 9–11 and ref. therein). Altogether, one can say that L_a is stabilized under hydration, whereas the $n\pi^*$ state is strongly destabilized. Most methods predict L_b to be only weakly affected by hydration.

Several theoretical studies explored the excited-state dynamics of Gua in the gas phase. All of these studies support the existence of a barrierless pathway connecting the Franck–Condon (FC) region and the conical intersection between S_1 and S_0. Several minimum

---

[a] *Max-Born-Institut für nichtlineare Optik und Kurzzeitspektroskopie, Max-Born-Straße 2A, 12489 Berlin, Germany. E-mail: luebcke@mbi-berlin.de; Fax: +49 30 6392 1329; Tel: +49 30 6392 1318*

[b] *Max-Planck-Institut für Kohlenforschung, 45470 Mülheim/Ruhr, Germany*

† Electronic supplementary information (ESI) available. See DOI: 10.1039/c5cp04394h

energy structures were located at conical intersection seams for the gas phase at different levels of theory.[12–15] At the OM2/MRCI level, one conical intersection (CI_α) connecting the ground state with the first excited state is found at 3.52 eV and has an $^2\mathrm{E}$ envelope puckered structure of the six-membered ring with the C2 atom being displaced out-of-plane (oop) and an increased C4–C5 bond length[15] (labelling of atoms according to Fig. 1). A similar structure was found in ref. 14. In the second $\mathrm{S}_0/\mathrm{S}_1$ CI, which is located at 2.8 eV at the OM2/MRCI level (CI_β), the NH_2 group is strongly displaced out of plane. The third $\mathrm{S}_0/\mathrm{S}_1$ CI located at 3.20 eV is characterized by a strong oop displacement of the O6 atom (CI_γ).[15] Similar structures were found at different levels of theory.[12–14] The same CIs with very similar structures were also found in aqueous solution.[9] The $\mathrm{CI}_\alpha^{\mathrm{hyd}}$ is characterized by a pronounced C2–N3 bond length elongation by 0.4 Å, $\mathrm{CI}_\beta^{\mathrm{hyd}}$ by an oop displacement of the NH_2 group by 80° and $\mathrm{CI}_\gamma^{\mathrm{hyd}}$ by an oop displacement of the carbonyl oxygen by 90°. In aqueous solution OM2/MRCI locates both $\mathrm{CI}_\beta^{\mathrm{hyd}}$ and $\mathrm{CI}_\gamma^{\mathrm{hyd}}$ at 3.5 eV. No value for $\mathrm{CI}_\alpha^{\mathrm{hyd}}$ could be provided.

Surface hopping dynamics simulations in the gas phase showed that relaxation proceeds mainly *via* CI_α and CI_β. Lan *et al.* found 60% of the excited-state population to electronically relax at CI_α (190 fs lifetime) and 40% at CI_β (400 fs lifetime).[15] Barbatti *et al.* found also CI_γ contributing to the excited-state decay: 5% of the excited-state population follows this relaxation path, while 67% undergo internal conversion at a CI associated with a pronounced ring deformation and 28% at a CI associated with an oop displacement of the amino group, similar to CI_β.[16]

The situation is significantly different in aqueous solution: Heggen *et al.*[9] showed that the relaxation path connecting the FC region with $\mathrm{CI}_\gamma^{\mathrm{hyd}}$ becomes the most important one associated with a lifetime of 265 fs or 216 fs for dynamics starting on S_1 or S_2, respectively. In contrast, internal conversion through $\mathrm{CI}_\alpha^{\mathrm{hyd}}$ and $\mathrm{CI}_\beta^{\mathrm{hyd}}$ becomes suppressed. Hopping times associated with those CIs are 343 fs (395 fs) and 441 fs (517 fs) for excitation of S_1 (S_2), respectively. If S_2, *i.e.* L_b, is excited, internal conversion to S_1 takes on average 21 fs. Due to the dominant relaxation at $\mathrm{CI}_\gamma^{\mathrm{hyd}}$, the average excited-state lifetime of Gua is slightly shorter in solution than in the gas phase.[9] In solution, the excited-state potential energy surface along the path toward the conical intersection exhibits a very steep gradient in the FC region, followed by a flat plateau. In these potential energy regions, the molecule possesses an almost planar purine ring structure. The flat plateau is connected to the conical intersection by a barrierless pathway. Along this reaction path, the molecule loses its planarity.[4]

Due to the non-volatility and the low solubility of Gua, there are only very few experimental studies on Gua both in the gas phase and in solution. For isolated Gua molecules, the time-dependent photoion signal was measured by two groups. Kang *et al.* found a monoexponential decay with a lifetime of 0.8 ps[2] and Canuel *et al.* found a biexponential excited-state decay with lifetimes of 150 fs and 360 fs.[3] The longer lifetime was corrected to 2.3 ps in a later work of the same group.[17] The situation of Gua is complicated as isolated Gua can exist in different rotameric and tautomeric forms at room temperature. The biologically relevant form is 9*H*-1*H*-amino-oxo guanine (1,9*H*-Gua) as shown in Fig. 1. In the gas phase, only about 32% of the Gua molecules are of this canonical form. Overall, there are four different tautomers with abundances >1% in the gas phase.[18] The above-mentioned experiments were not tautomer-selective and therefore, the lifetimes correspond to the mixture of excited-state relaxation of different tautomers. There are also two very recent studies on Guo[19] and deprotonated dGMP^-.[1] Also here, several tautomers are present. In dGMP^- two contributions were found with lifetimes of 50 fs and 600 fs, respectively. Both lifetimes are assigned to dynamics on the initially excited $\mathrm{S}_1(\pi\pi^*)$ state. The fast timescale is due to wave packet motion away from the FC region and the second contribution is then assigned to internal conversion. De Camillis *et al.* measured the time-resolved photoion yield and focused on the different dynamics of nucleosides compared to isolated DNA bases.[19] They found biexponential behaviour with the faster timescale being in agreement with previous measurements on DNA bases.[3] Interestingly, the longer lifetime was found to be a factor of 2 smaller in the nucleosides than in the corresponding DNA bases for adenosine, thymidine and cytidine. This was explained by an additional relaxation path in the nucleosides opened by a proton transfer through a sugar to base hydrogen bond. Unfortunately, the data on Guo suffered from high noise and the existence of several tautomers and rotamers and the retrieved lifetimes for this molecule did not follow the general trend of the other nucleosides. Instead, lifetimes of 230 fs and 2.3 ps were found, which are both in agreement with lifetimes reported for isolated Gua.[3,17] Hydration strongly affects the tautomeric distributions of Gua and Guo. In aqueous solution of Guo, only one considerably abundant tautomer, the canonical 1,9*H*-Guo form, is found.[20] The presence of the sugar moiety is not expected to influence the energetics or dynamics of the molecule, significantly.[21,22]

In the solution phase, the excited-state dynamics of Guo and GMP was investigated by transient absorption and fluorescence up-conversion.[4–6,23] In transient absorption experiments, Karunakaran *et al.*[4] found three different lifetimes after excitation at 266 nm and 289 nm: 0.2 ps, 0.9 ps and 2.5 ps. At 289 nm excitation is predominantly into S_1, while at 266 nm S_1 and S_2 are excited to approximately equal fractions. S_2, however, is discussed to decay to S_1 much faster than within 100 fs in line with simulations.[9] Also, the motion of the prepared wave packet away from the FC region is discussed to be unresolved, *i.e.* occurring faster than on a ≈100 fs timescale. The fastest lifetime is assigned to the movement of the wave packet between two regions on the potential energy surface, a planar plateau containing a planar pseudominimum and the non-planar minimum. The 0.9 ps lifetime is assigned to internal conversion between the non-planar minimum of S_1 and S_0, while the long lifetime has been ascribed to vibrational cooling of the ground state.[4]

Miannay *et al.* investigated the time-dependent fluorescence upon excitation at 266 nm and found complex dynamics with significant emission wavelength dependence. A global fit revealed also three different lifetimes of 0.16 ps, 0.67 ps and 2.0 ps.[6] These lifetimes are assigned to complex non-exponential dynamics on the S_1 potential energy surface, *i.e.* the longest observed lifetime is not due to vibrational cooling of the ground state. The strong emission wavelength dependence of the fluorescence dynamics was very surprising and has not been observed in any other DNA base, before.[6]

2 Experimental

A 1 mM aqueous solution of Guo, buffered at pH 8 (1 mM tris(hydroxymethyl)-aminomethane (TRIS) and hydrochloric acid (HCl)) is investigated in a liquid jet of about 10 μm diameter. At this pH value, Guo is neutral and the canonical form is the only significantly abundant tautomer present in solution. 30 mM sodium chloride (NaCl) is added to prevent electrokinetic charging of the liquid jet.[24] The experimental setup has been described in great detail elsewhere.[25] Briefly, a regeneratively amplified Ti:Sa laser system delivers 40 fs pulses at 800 nm. One part of the laser output is used to generate 266 nm (4.66 eV) pulses by sum frequency generation in BBO crystals. The remaining part of the laser output is used to pump an optical parametric amplifier (TOPAS, Light Conversion) which delivers pulses between 238 and 248 nm (5.21 and 5.00 eV, respectively). The UV pulses are attenuated to 80–95 nJ for the pump–probe experiment. Guo absorbs strongly at all wavelengths used in the experiment. While at 266 nm, both states, L_a and L_b are excited to about the same extent, at 238–248 nm we excite mainly into the L_b band.[4] However, our temporal resolution (200 fs cross-correlation width) is not sufficient to observe the sub-100 fs transition from L_b to L_a. Hence, the observed dynamics should be dominated by the relaxation on the L_a surface. Due to the ability to excite the molecule at both, the pump and probe wavelength, we expect to observe dynamics in both temporal directions.

The pulses are focused onto the liquid jet to focal spot sizes of about 100 μm. A chopper in each beam allows us to measure the one-color multi-photon signals separately (pump-only and probe-only) and subtract them from the two-color signal on a pulse-to-pulse basis.

Photoelectrons are collected and analyzed by a magnetic-bottle type time-of-flight spectrometer.

Guo and TRIS were purchased from Sigma-Aldrich Co. and sodium chloride from Merck. All substances were used without further purification. The sample solution was prepared using demineralized water (residual conductivity 0.25 $\mu S\ cm^{-1}$). At the given pulse intensities, sodium chloride does not contribute significantly to the photoelectron spectra.[7]

3 Computational

Starting from the trajectories described in ref. 9 we evaluated the time evolution of the ionization potential of 9*H*-Gua in water after excitation of the lowest excited singlet state (S_1). As in our former dynamics study, we used the semi-empirical OM2/MRCI method[26,27] as implemented in MNDO99.[28] Details regarding the computational method are given in ref. 9. The present calculation of the ionization potential is based on Koopmans' theorem, *i.e.* neglecting orbital relaxation and correlation effects (see ESI† for details and justification). We performed restricted open-shell OM2-SCF calculations for the lowest open-shell singlet state (S_1) of 9*H*-Gua in water (two singly occupied orbitals). The first ionization potential was determined from the energy of the highest singly occupied orbital (with appropriate two-electron corrections). In total, 130 trajectories from our previous dynamics investigations were suitable for detailed analysis of the ionization potential. In time steps of 10 fs, single-point calculations were performed for each trajectory and the ionization potential was computed as indicated above. As the ionization potential of the S_1 state is relevant for comparison with experiment, no further single-point calculations were done when the system had hopped to the ground state. Therefore the number of trajectories considered for the computation of the ionization potential declines with time. In the previous study, two different setups were chosen to start the excited-state decay dynamics: the system was either directly excited to the first excited state or to the second excited state (which then very quickly decays to the first excited state). 47 (83) trajectories correspond to the former (latter) case.

As we will show in the results section, our data provide evidence for a non-vertical probe transition. To estimate the accessibility of doubly-excited electronic states in Gua we carried out CASSCF calculations on representative geometries obtained from surface hopping dynamic simulations of Gua in aqueous solution[9] followed by the MRCI procedure. For these estimates, the solvent molecules were omitted. We used the aug-cc-pVTZ basis set. In principle, an accurate description of doubly excited states embedded in the ionization continuum is not possible, because they are coupled to the neighboring ionized states – leading to a decay of the former. As we will not attempt to determine the lifetime of the autoionizing states, we artificially reduce the active space of the CASSCF calculations to avoid the penetration of ionized states. Thus, the active space of the state-averaged CASSCF treatment consists of the HOMO, LUMO and LUMO+1 orbitals (two electrons in three orbitals) ensuring that the four lowest states were S_0, S_1, S_2 and the lowest doubly excited state. We have also tested the inclusion of the HOMO−1 orbital into the active space, but in this very expensive treatment the results did not change, remarkably. Further test calculations show that the next higher doubly excited state is energetically too high to be reached by a one-photon probe step. Consequently, we can restrict ourselves to the lowest doubly excited state.

4 Results

In Fig. 2A–C (colormap), the measured time-resolved photoelectron spectra of Guo are shown for different pump and probe wavelengths. At positive delay times the molecule is excited by 266 nm pulses (4.66 eV) and the probe wavelength is 248 nm (A, 5.0 eV), 243 nm (B, 5.1 eV) or 238 nm (C, 5.2 eV).

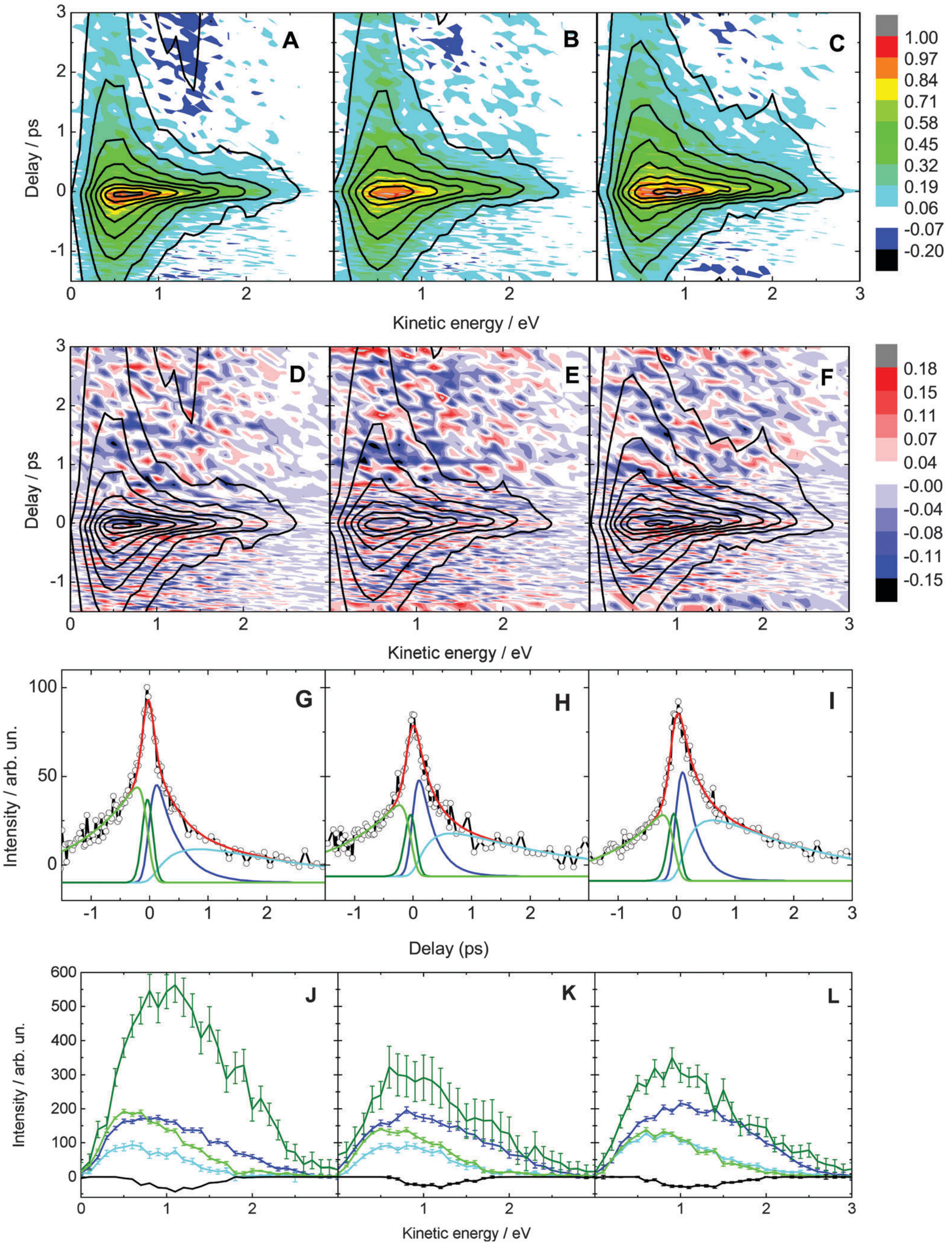

Fig. 2 Time-resolved photoelectron spectra of Guo excited and ionized at different photon energies: A, D, G, J: 4.66 eV + 5.0 eV, B, E, H, K: 4.66 eV + 5.1 eV, C, F, I, L: 4.66 eV + 5.2 eV. A, B, C: raw data (color map) and fit (contour lines); one-color signal has been subtracted. D, E, F: residuals (color map) and fit (contour lines). G, H, I: population dynamics obtained from the global fit. Dots mark energy-integrated raw data. The red line is the sum of the individual population dynamics. J, K, L: decay-associated spectra (same color code as for the population dynamics). Provided error bars are retrieved from the χ^2 fitting procedure.

For negative delays, the pulse sequence is opposed. At first glance, the plots look quite indifferent: in all cases, we observe a broad photoelectron distribution at time zero peaking at about 0.7 eV and covering the full energy range between 0 and 2.5 eV. With increasing delays, this broad distribution seems to shift toward about 0.5 eV and becomes more narrow. At longer delays, also negative pump probe signal is observed which we assign to dead time effects of the MCP detector. Very surprisingly, photoelectron distributions at negative delays nearly mirror those at positive delays (see Fig. S1, ESI†[29]). This is in contradiction to expecting a shift of the photoelectron distributions toward lower kinetic energies according to the probe photon energy difference. A similar behaviour as in Guo has not been observed in any other system we have studied so far and deserves a detailed discussion subsequent to the description of the experimental and theoretical results.

Following previous experimental observations of Guo in aqueous solution,[4,6] we performed a global analysis of the time-dependent photoelectron spectra, assuming a sequential population of different regions on the S_1 surface followed by internal conversion to the ground state. This model involves two rate constants. However, we want to stress that we do not have certain defined states in mind but rather use this bi-exponential description to model a continuous evolution of the wave packet on S_1. We did not consider dynamics on S_2 because we expect this higher excited state to decay to S_1 within our temporal resolution. Therefore, the dynamics of two populations in either delay direction are considered: one is exponentially decreasing at rate k_1, the other one exponentially growing at rate k_1 and decaying at rate k_2. We have introduced a factor γ in the rate equation accounting for structure-dependent ionization cross-sections, *i.e.* different probabilities to ionize the excited molecule in the two different regions of the S_1 surface. On the other hand, the factor γ may also account for a branching of the relaxation path, *i.e.* one part of the excited population returns to the ground state with a rate k_1 while the remaining part of the population persists longer in the excited state. This might be the case, if, depending on the initial geometries, only part of the wave packet gets close to the conical intersection at first instance, while the trajectories of the remaining part are more extended until they also encounter the conical intersection. The rate equations and their solution is given in the ESI.†[29] The cross-correlation width (200 fs fwhm) and the temporal origin t_0 were independently determined from nonresonant two-color photoelectron signal of gaseous nitric oxide (NO) and buffer solution. The amplitudes of the two exponentials for every kinetic energy determine the decay-associated spectra (DAS). Details on the fitting procedure are given in the ESI.†[29]

The resulting fit is shown as contour lines on top of the data in Fig. 2A–C. The corresponding residuals of these fits are shown in Fig. 2D–F (colormap). For comparison, the fit contour lines are displayed on top of the residuals, too. The model fits the data very well, no systematic residuals are apparent. Nevertheless, we note that the data can be equally well fitted by assuming a model with a parallel relaxation path. The population dynamics (G–I) and DAS (J–L) retrieved from the global fit are displayed as well.

The fit results are summarized in Table 1. For dynamics in positive delay direction, we find a shorter lifetime of about 290 fs and a longer one of about 2.3 ps. In negative delay direction, faster dynamics are observed: the shorter lifetime is about 50 fs, the longer one is about 1.1 ps.

For all pump and probe wavelength combinations, we find $\gamma \approx 0.3$. As already discussed before, this might be due to structure-dependent ionization cross section, *i.e.* ionization of the excited molecule is initially about 3 times more likely than at later times. On the other hand, it may also indicate that there is a branching in the relaxation path and 70% of the population decays to the ground state with rate k_1 and only 30% remain in the excited state for longer. From the comparison of signal at negative and positive delay times, conclusions on the wavelength dependent ionization cross-sections are possible. The signal ratio is given by

Table 1 Retrieved timescales for the excited-state relaxation of aqueous Guo obtained for different pump and probe photon energies. Additionally, the relative intensity γ of the fast and slow contributions is given. Provided uncertainties are retrieved from the χ^2 fitting procedure

	Pump/eV	Probe/eV	τ_{fast}/fs	τ_{slow}/ps	$\gamma = A_{\text{slow}}/A_{\text{fast}}$
Positive delays	4.66	5.00	380 ± 40	2.4 ± 0.3	0.32
	4.66	5.10	260 ± 60	2.3 ± 0.4	0.34
	4.66	5.21	250 ± 20	2.1 ± 0.1	0.42
Negative delays	5.00	4.66	40 ± 10	1.1 ± 0.1	0.24
	5.10	4.66	60 ± 30	1.1[a]	0.34
	5.21	4.66	60 ± 10	1.0 ± 0.1	0.29

[a] This lifetime was kept constant.

$$\frac{A_+}{A_-} = \frac{\alpha_{\text{GS}}(4.66\ \text{eV})}{\alpha_{\text{GS}}(5.0-5.2\ \text{eV})}\frac{\alpha_{\text{ES}}(5.0-5.2\ \text{eV})}{\alpha_{\text{ES}}(4.66\ \text{eV})}, \qquad (1)$$

where α_{GS} is the absorption coefficient of the ground state molecule and α_{ES} is the absorption coefficient of the excited molecule. The ground state absorption of Guo is well known.[30] We have evaluated only the signal associated with the slower decay because this is less sensitive to the particular fit parameters. For the individual photon energy combinations we find A_+/A_- to be 0.46 (4.66 eV/5.0 eV), 0.7 (4.66 eV/5.1 eV) and 1.04 (4.66 eV/5.2 eV) and deduce excited-state absorption coefficient ratios α_{ES}(4.66 eV)/α_{ES}(5.0–5.2 eV) of 1.7 (5.0 eV) and 1.3 (5.1–5.2 eV).

The DAS are presented in Fig. 2J–L. In addition, we compare the normalized DAS obtained for the different pulse sequences at different wavelength combinations in the ESI,† Fig. S1. As already evident from the data we find also the DAS to be nearly independent of the pulse sequence. Any differences between the spectra associated with a given decay obtained with a given photon energy combination are much smaller than the probe photon energy difference, *i.e.* 0.34–0.54 eV. There are some differences for the spectra associated with the fast decay which we mainly assign to limits of the global fitting and inaccuracy of the independent determination of cross-correlation width and temporal overlap.

Fig. 3 shows the time-dependent ionization energies calculated from Koopmans' theorem averaged over all different trajectories for Gua. No significant difference was observed for different groups of trajectories (as characterized by the respective hopping geometries). We observe that the average ionization potential of the S_1 state quickly rises from an initial value of about 3–4 eV to a value in the range of 5–6 eV, typically within 50 fs. We attribute this to fast initial dynamics in the S_1 state, with concomitant stabilization. An association with the steep gradient of the S_1 surface in the FC region seems obvious. At $t = 0$, we find a S_1 ionization energy of 3.54 eV which can be used for calibration against experimental data. With an applied shift of −1 eV we find very good agreement with our experimental data (*cf.* Fig. 3b).

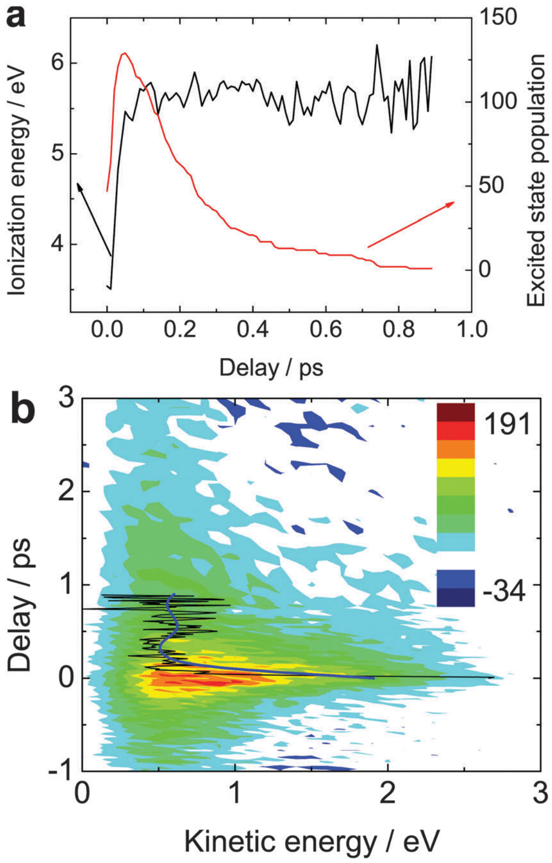

Fig. 3 (a) Time-dependent ionization energy of the S_1 state calculated from Koopmans' theorem (black) and S_1 state population (red). (b) Comparison between computational and experimental results (4.66 eV + 5.2 eV). Computational results (black) were shifted by −1.0 eV to match the experimental values (contour plot). To account for the limited time resolution, the time-dependent calculated ionization energies were convolved with a Gaussian of 200 fs FWHM (blue).

Besides the time-dependent ionization energies we also retrieve the time-dependent population of the S_1 state from our calculations, which is also shown in Fig. 3a. The computed lifetime is 314 fs for Gua which is significantly shorter than the experimentally observed ps lifetime for Guo. In a previous work, these deviations were suggested to be due to the different substituents at the N9 position.[9]

5 Discussion

In the following we suggest two alternative interpretations of the observed dynamics. One follows the interpretation of recent experimental work on aqueous Guo or GMP:[4,6] The first component is ascribed to the wave packet in the FC region that quickly relaxes due to initial dynamics on the S_1 surface concomitant with a fast rise of ionization energy. The second component is assigned to the wave packet evolving from the flat plateau to the conical intersection. In this region, no significant dependence of the ionization energy on the reaction coordinate (or time) is observed. We assign the decay of this component to the internal conversion to the ground state at the conical intersection. The S_1 lifetime is therefore ∼2.1–2.4 ps for excitation at 4.66 eV and 1.0–1.1 ps for excitation at 5.2 eV.

However, our finding that only 30% of the initially excited population is observed in the longer-lived signal allows also an alternative interpretation. As already indicated before, it is conceivable that (depending on the initial geometries) only a part of the wave packet (70%) quickly encounters the conical intersection (with rate $k_1 = (290\ \text{fs})^{-1}$), while the remaining part is too far away in phase space and needs more time to explore the potential energy surface and to find the conical intersection (rate $k_2 \sim (2.3\ \text{ps})^{-1}$). Further indirect support comes from the recent work of De Camillis *et al.*[19] in conjunction with our simulation. They found significantly faster dynamics in the nucleosides with respect to the bases for adenine, thymine and cytosine. Their guanine results however suffered from more noisy data and the presence of different tautomers in the gas phase. If we nevertheless presume a general mechanism for all DNA bases, *i.e.* a charge-transfer state opening a new relaxation route, the dynamics should be faster (not slower) in Guo than in Gua. Therefore the simulation results should represent an upper limit for the excited state lifetime of Guo. Indeed, the observed lifetime in the simulation of 314 fs is in very good agreement with rate k_1.

It is interesting to compare the observed dynamics in water with those of isolated molecules. De Camillis *et al.* retrieved lifetimes which are in very good agreement with our results, both for the fast and slow component, indicating that the solvent environment does not have a huge influence in this case and dynamics is governed by internal degrees of freedom.[19] However the error bars are quite large and the sample was a tautomeric and rotameric mixture in their work. For this reason, a direct comparison of the two different experiments is difficult. Chatterley *et al.* performed similar experiments as we did on isolated $dGMP^-$, *i.e.* they measured photoelectron spectra. They observed somewhat faster dynamics (50 fs/600 fs) than we did (290 fs/2300 fs), but the interpretation is very similar to the first interpretation that we suggested: the fast timescale is due to wave packet motion away from the FC region, while the second component is due to internal conversion. This assignment was motivated by the similarity of timescales as observed for hydrated $dGMP^-$. Nevertheless, a branching of the trajectories can likewise explain the observations.

In the following we will further discuss our data in the frame of the first interpretation provided for the observed dynamics (no branching). We emphasize, however, that the second interpretation would lead to the same conclusions. We will now turn the discussion to the nearly identical decay associated spectra for the different pulse sequences. As discussed in the literature,[4,9] we expect to observe dynamics in the S_1 state for either pump pulse. For vertical ionization we do expect to observe photoelectron kinetic energy distributions that reflect the differences in probe photon energy. This is apparently not the case here. Assuming, that the ionization cross section does not depend on the probe photon energy in a very peculiar way, the results suggest that either dynamics is observed in different states (*i.e.* S_1 and S_2) or the transition in the probe step is not vertical for at least one of the two pulse sequences. There is no reason to question the interpretation from previous experiments and simulations that there is an ultrafast population transfer from S_2 to S_1 within a few tens of fs. Therefore, we have to refuse that the probe photon absorption is accompanied by a vertical transition to the ionic state. We suggest the existence of a metastable electronic state, embedded in the ionization continuum. According to our hypothesis, the same vibronic levels of this electronic state are populated, irrespective of the sequence of the two light pulses. We suppose that this metastable state is a doubly excited one, characterized by a simultaneous excitation of two valence electrons, $(\pi^*)^2$, decaying vertically to the ionic ground state D_0, where the kinetic energy of the ejected photoelectrons is given by the difference of the doubly-excited-state potential energy and the ground-state ion potential energy.

These two situations, ionization *via* a doubly-excited state and direct ionization are sketched in Fig. 4. The pump pulse of a given photon energy prepares the molecule in the electronically excited S_1 state with a certain amount of kinetic energy stored in different vibrational modes. This excess energy can be distributed among further vibrational modes *via* intramolecular vibrational redistribution (IVR) or released to the solvent *via* intermolecular energy transfer (IET). There is not much known about the vibrational cooling dynamics in the excited S_1 state of neutral Guo, because it is superimposed by the very fast internal conversion to the ground state. However, in protonated GMP vibrational cooling dynamics in S_1 takes about 3 ps.[31] We can assume, that this dynamics is similar in the neutral molecule, *i.e.* slower than internal conversion, and that there is no significant redistribution of excess vibrational energy in the course of excited-state relaxation. Transition to the doubly-excited state cannot be vertical for both pulse sequences. The vibrational energy distribution of the molecule in the doubly-excited state is not necessarily the same as for the molecule in the S_1 state. If the doubly-excited state was not involved, the photoinduced transition to the ionic ground state would be vertical and the vibrational energy distribution of the molecule in the S_1 state would remain in the ion. The photoelectron kinetic energy is then the difference of absorbed probe photon energy and the potential energy difference between the S_1 and D_0 state. On the basis of a simple model (one- and three-dimensional harmonic oscillator), the behaviour of the photoelectron spectrum is compared for auto- and direct ionization in the ESI.†[29] Our *ab initio* calculations show that, except for $t = 0$, in all investigated geometries the lowest doubly excited state is located in an accessible energy range above S_1 and is nearly parallel to it (deviations not larger than 0.5 eV). Investigating the electron configuration of this doubly excited state, we found that for all geometries the predominant contribution ($>95\%$) is of $(\pi^*)^2$ character. In the ESI,†[29] this orbital is shown and compared with the HOMO. The transition dipole moment for the excitation of the doubly excited state from S_1 is comparable to or even larger than that of the S_0–S_1 transition. This means that, in principle, the cross section for excitation of the doubly-excited state is sufficiently high. Of course, in a more detailed probe absorption treatment, interference effects between discrete and continuum states have to be considered, leading to Fano spectral features.[32] Such fingerprints of the doubly-excited state were not observed in our experiments, presumably, because of the remarkable spectral broadening due to vibronic substructure and the water environment. In most cases the doubly-excited state is energetically located ~ 0.5–1.5 eV above the ionization limit, *i.e.* explaining the observed photoelectron kinetic energies. Detailed results of the calculations are provided in the ESI.†[29]

If ionization occurs *via* the doubly-excited state as we suggest, the observed kinetic energies are given by the difference between the doubly-excited and the ionic state. The binding energy of the initially excited S_1 state is generally not reflected in the data. So, the question arises, why the calculated S_1 ionization

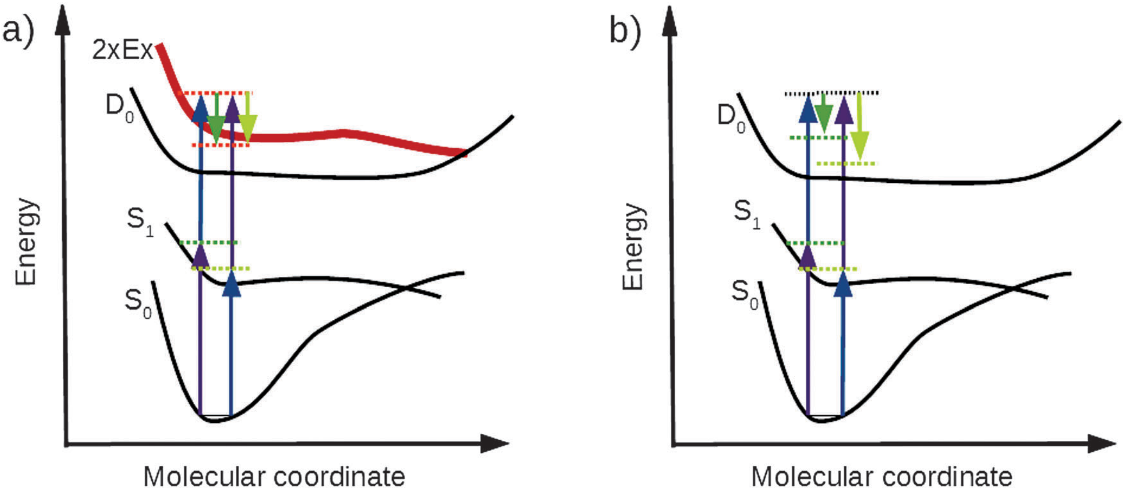

Fig. 4 One-dimensional sketch of potential energy surfaces and the photoionization processes in the presence of a doubly-excited state 2xEx (a) and in its absence (b). Blue and violet arrows represent the two different photon energies. Different green arrows represent photoelectron kinetic energies for the two different pulse sequences.

energies are fitting the data so nicely. From our calculations we suggest that the doubly-excited-state potential energy depends similarly on the reaction coordinate as the S_1 state, *i.e.* the S_1 binding energy differs from the difference of doubly-excited and ionic potential only by a nearly constant value.

While the kinetic energy distribution may not contain direct information about the S_1 potential energy surface, the time-dependent photoelectron signal clearly reflects excited-state population dynamics together with structure dependent excited-state absorption cross-sections. We found faster dynamics when the molecule was excited at 5.0–5.2 eV than at 4.66 eV. This can be discussed in different ways:

(a) Accelerated dynamics due to higher excess energy

Excitation at higher photon energies prepares the excited state with higher vibrational energy. This generally leads to faster dynamics. For pump wavelengths of 266 nm and 287 nm, however, no significant difference in the dynamics was observed.[4] Nevertheless, the situation may be different at 238 nm, which is also indicated by surface hopping dynamics simulations. They yielded slightly faster excited-state decays after initial excitation of S_2 than of S_1.[9]

(b) Faster dynamics due to accessibility of additional relaxation pathways

Due to the higher excess energies in the excited state, new relaxation pathways may open.[6]

(c) Limited FC windows for ionization

At negative delays the excited state is probed with 4.66 eV photons, *i.e.* at lower energy than at positive delays. If the energy gap between excited and ionic state increases above the probe photon energy, the excited state becomes invisible for the probe pulse in photoelectron spectroscopy. This point is reached faster for a smaller probe photon energy, *i.e.* the observed dynamics seem to be faster.

In the presence of the doubly-excited state, point c is not relevant, because the accessibility of the final state is only given by the total absorbed photon energy.

Our retrieved timescales compare well with timescales found in transient absorption and fluorescence up-conversion.[4,6] However, in contrast to fluorescence up-conversion and transient absorption we only need two components to satisfactorily describe our data. We want to stress that we do not intend to assign these two lifetimes to defined states on the S_1 potential energy surface but rather use them to describe a continuous evolution of the excited wave packet. We also want to note that in agreement with fluorescence up-conversion our data suggest that the longest observed timescale is due to dynamics in the S_1 state, most likely related to S_1 population decay due to internal conversion, and does not reflect ground state cooling.

It is interesting to investigate the DAS in more detail. At first glance it is striking, that the photoelectron spectrum is initially very broad (FWHM of the first component is 1.5 eV) and becomes significantly more narrow at later times (FWHM of the second component is 1.0 eV). This may at first be surprising since the wave packet is expected to spread out on the flat S_1 surface which could be expected to transfer into very broad photoelectron spectra. However, we will show that the particular potential energy landscape for Guo/Gua readily explains this observation. The wave packet in S_1 is prepared by the pump pulse where the vibrational ground state wavefunction is projected onto S_1. In the FC region, the S_1 potential energy surface possesses a very steep gradient and we suggest that this is also the case for the doubly-excited state; *i.e.* in this region, ionization energies of S_1 as calculated from Koopmans' theorem and potential energy differences between the doubly-excited and the ionic ground state have very different values. This transfers into a very broad distribution of resulting photoelectron kinetic energies. This very steep potential gradient in the FC region of the S_1 state leads to a very fast stabilization of the excited state within about 290 fs (in case of 4.66 eV excitation). This is sketched in Fig. 5. On the other hand, our calculations show, that after this initial stabilization the ionic potential along the reaction coordinate is parallel to the S_1 and the doubly-excited-state potential. Therefore, even a strongly broadened wave packet will lead to a narrow photoelectron band. The observed width of 1 eV is typical for hydrated species and mainly caused by inhomogeneous broadening due to very different local solvation structures.[33,34]

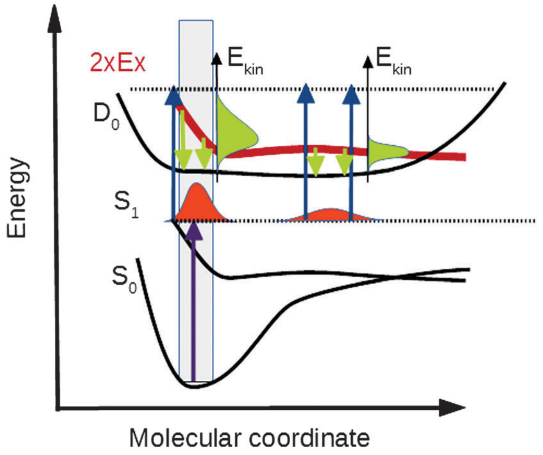

Fig. 5 Schematic potential energy curves of Guo in water. The pump pulse launches an excited-state wave packet (orange) in the Franck–Condon region (grey) of the populated S_1 or S_2 (not shown) state. The S_2 state decays within the time resolution into S_1. The time-dependent S_1 ionization energy (along the relaxation path) is nearly constant besides a sharp initial rise, leading to the sketched ionic potential curve D_0. Around the temporal overlap of both pulses, the steep gradient of the excited state in the FC region is mapped into a very broad photoelectron kinetic energy distribution (light green). With increasing delays, the wave packet dephases and spreads on the excited-state potential. Ionization in the flat region of the S_1 potential leads to a more narrow distribution of photoelectrons due to the parallelity of the doubly-excited 2xEx state and D_0.

6 Conclusion

We have investigated the excited-state relaxation in aqueous Guo by time-resolved photoelectron spectroscopy. Dynamics were initiated by pulses at 266 nm, 248 nm, 244 nm or 238 nm on the S_1 or S_2 potential energy surface. The $S_2 \rightarrow S_1$ transition was not resolved in our experiments and the data therefore reflects dynamics in the S_1 state. In agreement with our surface hopping dynamic simulations, the photoelectron spectrum rapidly shifts towards smaller kinetic energies until it stabilizes at a kinetic energy of about 0.5 eV. The spectrum also narrows significantly. We have suggested two alternative interpretations of the observed dynamics. The first one follows the interpretation of recent experimental results of hydrated Guo and GMP.[4,6] The fast shift is assigned to initial dynamics in the S_1 state: relaxation from the steep FC region to the rather flat plateau occurs in about 290 fs if dynamics are initiated by 266 nm pulses. This is followed by a slower signal decay within ∼ 2.3 ps which we assign to internal conversion at a conical intersection. We have observed that only 30% of the initially excited population contributes to the signal of the slower decaying component. This might be due to structure-dependent ionization cross section. On the other hand, this finding can also suggest an alternative interpretation: the dominant part (70%) of the initially excited population encounters the conical intersection with the ground state very fast and gives rise for the observed decay rate $k_1 = (290\ \text{fs})^{-1}$ in agreement with the S_1 lifetime observed in our simulation, while the remaining part of the initially excited population (30%) follows more extended trajectories in phase space and needs more time to encounter the conical intersection. This part of the population gives rise to the observed second decay rate $k_2 = (2.3\ \text{ps})^{-1}$. More investigations are needed to decide in favor of one or the other relaxation model. Time-resolved photoelectron imaging experiments allowing to also measure the angular distribution of the photoelectrons may be one promising technique to solve this problem.[35] As it was shown theoretically for NO_2[36] such measurements may allow to obtain a clearer picture of ionization channels near a conical intersection. However, it is currently not possible to apply this technique to highly volatile samples.

Interestingly, our photoelectron kinetic energy distributions show that the probe step is not vertical, *i.e.* the measured photoelectron kinetic energy distributions do not depend on the probe photon energy in the range applied here. We suggest that this is due to population of a doubly-excited state in the probe step which rapidly decays *via* autoionization. These results show that in time-resolved photoelectron spectroscopy the photoelectron kinetic energy distributions can be dominated by intermediate transients even in a one-photon probe step and that the analysis and discussion of such data requires great care. In diatomic molecules, doubly-excited autoionizing states have been investigated and studied in some detail.[37,38] To the best of our knowledge this is not the case for larger molecules.

Acknowledgements

The authors thank F. Noack for his support by providing the laser system in the femtosecond application laboratory of the Max-Born-Institut Berlin. This work was financially supported by Deutsche Forschungsgemeinschaft, Project LU 1638/1-1.

References

1 A. S. Chatterley, C. W. West, V. G. Stavros and J. R. R. Verlet, *Chem. Sci.*, 2014, **5**, 3963.

2 H. Kang, K. T. Lee, B. Jung, Y. J. Ko and S. K. Kim, *J. Am. Chem. Soc.*, 2002, **124**, 12958–12959.

3 C. Canuel, M. Mons, F. Piuzzi, B. Tardivel, I. Dimicoli and M. Elhanine, *J. Chem. Phys.*, 2005, **122**, 074316.

4 V. Karunakaran, K. Kleinermanns, R. Improta and S. A. Kovalenko, *J. Am. Chem. Soc.*, 2009, **131**, 5839–5850.

5 J. Peon and A. H. Zewail, *Chem. Phys. Lett.*, 2001, **348**, 255–262.

6 F.-A. Miannay, T. Gustavsson, A. Banyasz and D. Markovitsi, *J. Phys. Chem. A*, 2010, **114**, 3256.

7 F. Buchner, H.-H. Ritze, J. Lahl and A. Lübcke, *Phys. Chem. Chem. Phys.*, 2013, **15**, 11402.

8 F. Buchner, A. Nakayama, S. Yamazaki, H.-H. Ritze and A. Lübcke, *J. Am. Chem. Soc.*, 2015, **137**, 2931.

9 B. Heggen, Z. Lan and W. Thiel, *Phys. Chem. Chem. Phys.*, 2012, **14**, 8137.

10 R. Improta and V. Barone, *Top. Curr. Chem.*, Springer, Berlin, Heidelberg, 2014, pp. 1–29.

11 M. Parac, M. Doerr, C. M. Marian and W. Thiel, *J. Comput. Chem.*, 2010, **31**, 90.

12 H. Chen and S. Li, *J. Chem. Phys.*, 2006, **124**, 154315.

13 C. M. Marian, *J. Phys. Chem. A*, 2007, **111**, 1545.

14 L. Serrano-Andres, M. Merchan and A. C. Borin, *J. Am. Chem. Soc.*, 2008, **130**, 2473.

15 Z. Lan, E. Fabiano and W. Thiel, *ChemPhysChem*, 2009, **10**, 1225.

16 M. Barbatti, J. J. Szymczak, A. J. A. Aquino, D. Nachtigallova and H. Lischka, *J. Chem. Phys.*, 2011, **134**, 014304.

17 M. Mons, I. Dimicoli and F. Piuzzi, *Isolated Guanine: Tautomerism, Spectroscopy and Excited State Dynamics*, Springer, Dordrecht, London, 2008, pp. 343–367.

18 Y. H. Jang, W. A. G. III, K. T. Noyes, L. C. Sowers, S. Hwang and D. S. Chung, *J. Phys. Chem. B*, 2003, **107**, 344.

19 S. D. Camillis, J. Miles, G. Alexander, O. Ghafur, I. D. Williams, D. Townsend and J. B. Greenwood, *Phys. Chem. Chem. Phys.*, 2015, **17**, 23643.

20 H. T. Miles, F. B. Howard and J. Frazier, *Science*, 1963, **142**, 1458.

21 C. E. Crespo-Hernández, B. Cohen, P. M. Hare and B. Kohler, *Chem. Rev.*, 2004, **104**, 1977.

22 C. T. Middleton, K. de La Harpe, C. Su, Y. K. Law, C. E. Crespo-Hernández and B. Kohler, *Annu. Rev. Phys. Chem.*, 2009, **60**, 217.

23 J.-M. L. Pecourt, J. Peon and B. Kohler, *J. Am. Chem. Soc.*, 2001, **123**, 10370.

24 N. Preissler, F. Buchner, T. Schultz and A. Lübcke, *J. Phys. Chem. B*, 2013, **117**, 2422.

25 F. Buchner, A. Lübcke, N. Heine and T. Schultz, *Rev. Sci. Instrum.*, 2010, **81**, 113107.

26 W. Weber and W. Thiel, *Theor. Chem. Acc.*, 2000, **103**, 495.

27 A. Koslowski, M. E. Beck and W. Thiel, *J. Comput. Chem.*, 2003, **24**, 714.

28 W. Thiel, *MNDO program, version 6.1*, Mülheim, 2007.

29 ESI†.

30 D. Voet, W. B. Gratzer, R. A. Cox and P. Doty, *Biopolymers*, 1963, **1**, 193.

31 Y. Zhang, R. Improta and B. Kohler, *Phys. Chem. Chem. Phys.*, 2014, **16**, 1487.

32 U. Fano, *Phys. Rev.*, 1961, **124**, 1866.

33 C. Schroeder, E. Pluhařová, R. Seidel, W. P. Schroeder, M. Faubel, P. Slavíček, B. Winter, P. Jungwirth and S. E. Bradforth, *J. Am. Chem. Soc.*, 2015, **137**, 201.

34 A. Lübcke, F. Buchner, N. Heine, I. V. Hertel and T. Schultz, *Phys. Chem. Chem. Phys.*, 2010, **12**, 14629.

35 P. Trabs, F. Buchner, M. Ghotbi, A. Lübcke, H.-H. Ritze, M. J. J. Vrakking and A. Rouzée, *J. Phys. B: At., Mol. Opt. Phys.*, 2014, **47**, 124016.

36 Y. Arasaki, K. Takatsuka, K. Wang and V. McKoy, *J. Chem. Phys.*, 2010, **132**, 124307.

37 T. Baumert, M. Grosser, R. Thalweiser and G. Gerber, *Phys. Rev. Lett.*, 1991, **67**, 3753.

38 G. Sansone, F. Kelkensberg, J. F. Pérez-Torres, F. Morales, M. F. Kling, W. Siu, O. Ghafur, P. Johnsson, M. Swoboda, E. Benedetti, F. Ferrari, F. Lépine, J. L. Sanz-Vicario, S. Zherebtsov, I. Znakovskaya, A. L'Hullier, M. Y. Ivanov, M. Nisoli, F. Martín and M. J. J. Vrakking, *Nature*, 2010, **465**, 763.

SUPPORTING INFORMATION

Excited state dynamics of guanosine in aqueous solution revealed by time-resolved photoelectron spectroscopy: experiment and theory

Franziska Buchner,[1] Berit Heggen,[2] Hans-Hermann Ritze,[1] Walter Thiel,[2]
and Andrea Lübcke[1,*]
[1] *Max-Born-Institut für nichtlineare Optik und Kurzzeitspektroskopie,*
Max-Born-Straße 2A, 12489 Berlin, Germany.
[2] *Max-Planck-Institut für Kohlenforschung, Kaiser-Wilhelm-Platz 1, 45470*
Mülheim an der Ruhr, Germany.

Computation of ionization potential

In the present work, we have evaluated the first ionization potential of 9H-Gua in water for several thousand geometries (130 trajectories, up to 90 points per trajectory) in order to compare with the experimental data (see Figure 3 of the main paper). Our guideline in selecting a computational method for this purpose was to be consistent with the approach used to generate the trajectories (OM2/MRCI) and to apply the simplest treatment that is expected to be realistic. Therefore, our first choice was to apply Koopmans' theorem. At this level, the ionization potential is evaluated by molecular orbital (MO) theory assuming that the MOs do not change during ionization. For closed-shell systems, the ionization potential (IP) is then equal to the negative MO energy: IPi $= -\epsilon_i$. For restricted open-shell treatments, the derivation yields additional two-electron terms that must be included for proper application of Koopmans' theorem. In our case (open-shell singlet with two unpaired electrons in MOs i and j, ϵ_i ¿ ϵ_j , half-electron treatment), the appropriate equation is: $\mathrm{IP}_i = -\epsilon_i \mathrm{J}_{ii}/4\mathrm{J}_{jj}/4 + 3\mathrm{K}_{ij}/2$, with J and K denoting the Coulomb and exchange integrals in the MO basis. This is the equation applied in our calculations.

An obvious question is whether this approach is adequate for the purposes of the present work (besides being simple and efficient for the very large number of required IP evaluations). This can be checked by higher-level calculations and by comparison with experiment.

Going beyond Koopmans' theorem at the semiempirical OM2 level can be done in two steps. First, one can carry out separate OM2 SCF calculations for the open-shell singlet excited state (S1) and for the doublet ground state of the cation generated by ionization (D0) to account for orbital relaxation in the cation, which will cause the resulting OM2-ΔSCF value of the ionization potential to be lower than that given by Koopmans' theorem. In a second step, one can perform corresponding OM2/MRCI calculations of the D0–S1 energy difference (using the same active space and the same options as in the trajectory calculations) to include also differences in correlation energy, which will generally raise the computed ionization potential (since ionization removes one electron from the system). The corrections from these two refinements will thus tend to cancel each other this is the reason why ionization potentials determined from Koopmans' theorem (KT)

	IP(t = 0) / eV	IP(t = 100) fs / eV	Difference / eV
OM2-KT	3.57	5.06	1.49
OM2-ΔSCF	3.48	4.87	1.39
OM2/MRCI	3.93	5.24	1.31
B3LYP/TZVP	3.39	4.42	1.03

Table 1: TABLE S1: Calculated ionization potentials of the S1 state of 9H-Gua.

are often more realistic than expected.

For a more quantitative assessment, we have computed the ionization potentials of isolated 9H-Gua for two typical geometries taken from a representative trajectory at time t = 0 and t = 100 fs using the three approaches outlined above (OM2-KT, OM2-ΔSCF, and OM2/MRCI). Those results are summarized in Table S1. For comparison, we have also calculated the D0–S1 energy difference of isolated 9H-Gua at these two geometries by density functional theory (DFT) at the B3LYP/TZVP level (TDDFT for S1, UDFT for D0).

Evidently, all approaches yield ionization potentials of roughly similar magnitude, and they all predict a significant increase within the first 100 fs of the excited-state dynamics.

Experimentally, this increase is clearly observed and is of similar magnitude (see Figure 3 of the main paper). All approaches considered thus agree with experiment in this crucial qualitative aspect. To achieve a more quantitative fit, the OM2-KT values were calibrated against experiment (uniform shift of -1.0 eV, see the main paper) which gave a very satisfactory match with experiment (see Figure 3b of the main paper). To achieve a better quantitative agreement without calibration, it would be necessary to apply significantly more accurate computational methods (DFT at the B3LYP/TZVP would not be sufficient for this purpose, see the results in Table S1). This is beyond the scope of the present computational work, which focuses on a qualitative understanding of the experimental observations. In summary, these considerations and comparisons justify the application of Koopmans' theorem at the OM2 level to compute the time evolution of the ionization potential of 9H-Gua in water during the excited-state dynamics.

Appendix C

Gold Carbenoids: Lessons Learnt from a Transmetalation Approach

Günter Seidel, Barbara Gabor, Richard Goddard, **Berit Heggen**, Walter Thiel and Alois Fürstner

Angew. Chem. Int. Ed., **2014**, 53, 879 – 882.

Performed the theoretical investigations in the paper.

Angewandte
International Edition Chemie

Carbophilic Catalysts Hot Paper

DOI: 10.1002/anie.201308842

Gold Carbenoids: Lessons Learnt from a Transmetalation Approach**

*Günter Seidel, Barbara Gabor, Richard Goddard, Berit Heggen, Walter Thiel, and Alois Fürstner**

***Abstract:** Carbophilic catalysts that are based on Au^I allow a host of different nucleophiles to be added across various π systems.[1–3] Although many of these reactions are thought to proceed via gold carbenoids, the challenge to observe and characterize these putative intermediates has basically been unmet.[4] The current mechanistic interpretation therefore largely relies on indirect evidence and computational data, some of which are subject to debate.[5] In an attempt to fill this gap, we pursued a potential route to gold carbenoids by formal transmetalation of chromium or tungsten Fischer carbene complexes with $[LAu]^+$. Whereas this transformation proceeds with exceptional ease as long as a stabilizing heteroelement is present on the carbene center, it stops half-way in its absence. Rather unusual bimetallic arrays are formed, which allow the charge density to delocalize over several positions. The obvious difficulty of releasing an "unstabilized" gold carbenoid has potential mechanistic implications for the understanding of π-acid catalysis in general.*

Amongst the few pertinent experimental studies on gold carbenoids known in the literature, a recent investigation by Widenhoefer and co-workers is arguably of the highest relevance.[6] For the first time, these authors managed to observe the actual intermediate of a prototype enyne cycloisomerization reaction by NMR spectroscopy; this intermediate resembles the cyclobutenyl resonance extreme **2a**,**b** rather than the cyclopropylmethyl form **2c** (Scheme 1). This observation validates an earlier mechanistic interpretation of π-acid catalysis that implied a build-up of delocalized positive charge density on the organic ligand.[1,7,8]

Other relevant data come from mass spectrometric investigations of (substituted) gold benzylidene species and their reactivity with various types of olefins.[9] Hammett correlations suggest that the resonance form **4a** significantly contributes to their ground-state structure, although a final conclusion as to whether the positive charge resides on carbon or on gold (**4b**) could not be drawn (Scheme 1). These studies also revealed that cyclopropanations of olefins by gold carbenoids, though stereospecific, likely proceed in a stepwise rather than in a concerted manner.

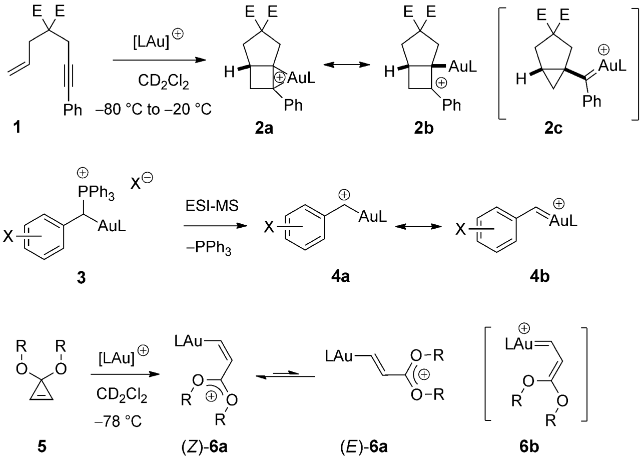

Scheme 1. Experimentally observed "gold carbenoids" pertinent to the mechanistic discussion of π-acid catalysis; for the sake of clarity, the non-coordinating counterions are not depicted; L = two-electron-donor ligand. E = COOMe; R,R = Me,Me or -$(CH_2)_3$-.

In a complementary approach, our group studied the rearrangement of cyclopropene derivatives, which is known to be an excellent entry point into the metal carbene series.[10] On treatment with $[(R_3P)Au]NTf_2$ at −78 °C, substrates of type **5** were transformed into discrete alkenyl gold complexes **6a** that carry a charged ligand (Scheme 1). Surprisingly small rotational barriers indicate that the carbene resonance extreme **6b** hardly contributes to the ground-state structure. We had emphasized that the vinylogous oxygen substituents in **6** might not be innocent, but favor build-up of positive charge density on the ligand.[10,11] Subsequent computational studies that were calibrated against our experimental data confirmed that the carbene resonance extreme becomes more significant as the oxygen substituents are replaced by alkyl groups, and strong ancillary donor ligands L are chosen.[12] Because of a peculiar three-center/four-electron bonding situation, however, increased π-electron back-donation from the metal to the ligand weakens the C−Au σ-bond to the extent that the overall bond order remains close to one.

Herein, we report further efforts to characterize germane gold carbenoids that are devoid of stabilizing heteroelement substituents. As the cyclopropene rearrangement had failed in such cases,[11] a different entry was sought. Attempts at reacting the diazo compound $Ph_2C{=}N_2$ with an appropriate gold precursor were equally unsuccessful, affording only the corresponding azine $Ph_2C{=}N{-}N{=}CPh_2$.[13–15] We then turned our attention to the carbene transfer method that is known to

---

[*] Ing. G. Seidel, B. Gabor, Dr. R. Goddard, Dipl.-Ing. B. Heggen, Prof. W. Thiel, Prof. A. Fürstner
Max-Planck-Institut für Kohlenforschung
45470 Mülheim/Ruhr (Germany)
E-mail: fuerstner@kofo.mpg.de

[**] Generous financial support by the MPG and the Fonds der Chemischen Industrie is gratefully acknowledged. We thank P. Philips and W. Wisniewski for NMR support, J. Rust and H. Schucht for assistance with the X-ray structures, and Dr. Manuel Alcarazo for fruitful discussions.

Supporting information for this article is available on the WWW under http://dx.doi.org/10.1002/anie.201308842.

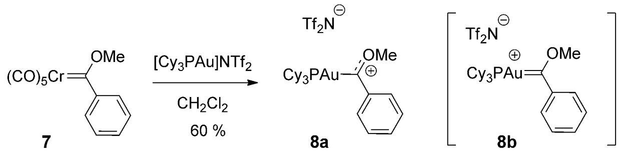

Scheme 2. Preparation of a prototype Fischer gold carbenoid by metal exchange. Cy = cyclohexyl.

work exceedingly well for the preparation of stabilized Fischer-type carbene complexes of gold.[16–18]

Indeed, reaction of **7** with [(Cy$_3$P)Au]NTf$_2$ furnished **8** in good yield (Scheme 2). Although the preparative experiments were carried out at ambient temperature, NMR spectroscopy revealed that this formal transmetalation proceeds even at −50 °C. As expected, the structure of **8** in the solid state (see the Supporting Information)[19] shows that the bond order of the C–Au bond (2.046(5) Å) is very close to one, whereas the C–OMe bond (1.289(6) Å) is notably contracted. This metric implies that the oxocarbenium resonance form **8a** is dominant.[20,21]

The remarkable ease with which this Fischer-type gold carbenoid is formed stands in striking contrast to the outcome of the attempted transmetalation of the diphenylcarbene complexes **9** and **12**, which were thought to provide the same gold carbenoid **11** devoid of stabilizing heteroatom donors. Yet, **11** could never be detected, irrespective of the ancillary ligand L bound to the cationic gold reagent.

In the tungsten series, the only detectable products are heteroleptic *gem*-dimetallic complexes of type **10**, which form rapidly even at −50 °C (Scheme 3). In CD$_2$Cl$_2$ solution, **10** (L = IMes) is stable at ambient temperature for hours before it eventually decomposes,[22] and this complex even persists under a CO atmosphere for more than two hours; the tungsten fragment could not be removed, and hence, free **11** could not be released under any of the chosen conditions.

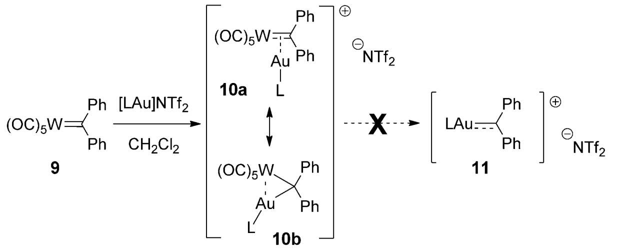

Scheme 3. Attempted transmetalation of a tungsten carbene with [LAu]$^+$ affords hetero-bimetallic complexes **10** rather than the gold carbenoids **11**: 67 % (L = IMes), 93 % (L = PPh$_3$), quant. (by NMR spectroscopy; L = PCy$_3$, PMe$_3$). IMes = 1,3-bis(2,4,6-trimethylphenyl)imidazol-2-ylidene.

Crystals that are suitable for X-ray analysis could be grown for two members of this series. The solid-state structure of **10** (L = IMes) is representative (Figure 1).[19] The C–W bond (2.1996(13) Å) is only slightly longer than that in the starting complex **9** (2.15(2)/2.13(2) Å);[23] the C–Au bond length (2.1445(13) Å) is comparable to that in other *gem*-metalated species.[24] The W···Au contact (2.7751(2) Å) suggests that the unusual hetero-bimetallic structure of **10** is stabilized by an attractive force between the two metal centers that is reminiscent of the well-known aurophilic interactions in homoleptic gold clusters.[25–27]

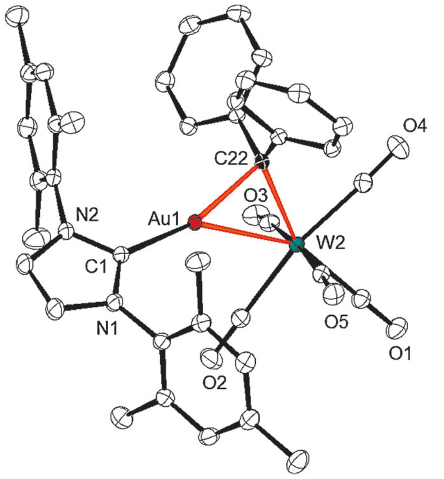

Figure 1. Structure of complex **10** (L = IMes) in the solid state; only the cationic entity is shown, whereas the escorting [NTf$_2$]$^-$ and co-crystallized solvent have been removed for clarity. For the entire structure, see the Supporting Information.

A salient feature of **10** (L = IMes) is the almost planar "carbene" center, even though the C–Au distance of 2.1445(13) Å suggests that this site engages in four (rather than three) bonding interactions. Likewise, the considerable high-field shift of the carbene carbon atom from 326.5 ppm in the tungsten precursor **9** to 262.6 ppm in **10** (L = PPh$_3$), together with a clearly discernible $J_{C,P} = 36$ Hz, indicates that the carbene site interacts with the coordinated gold fragment. To consolidate these data, we assume that the bonding in **10** is best described as a side-on complex of [LAu]$^+$ onto the π bond of the starting tungsten carbene, with moderate back-donation of electron density from gold into the antibonding orbitals of this entity. Overall, the complex seems closer to a tungsten carbene bearing an η^2-bound [LAu]$^+$ unit, as drawn in **10a**, than to the resonance extreme **10b** with a truly bridging carbene site.[28]

The reaction of the corresponding chromium carbene complex **12**[19,29] with [LAu]$^+$ at −50 °C primarily leads to the same type of hetero-bimetallic complex **13**, as deduced from the characteristic spectroscopic signature (Scheme 4).[30] Yet, this product rapidly converts into a more involved species **14** that retains the chromium carbonyl fragment but exhibits only four CO ligands that are magnetically inequivalent.[31] The bridging "carbene" center is strongly shielded [for L = PCy$_3$: 243.1 ppm (d, $J_{P,C} = 47$ Hz)], and the *ipso* carbon atom of one of the two arene rings resonates at unusually high field (93.6 ppm); this latter phenyl group is locked, whereas the second one rotates freely at temperatures ≥ −30 °C.[32]

The unusual constitution is apparent from the structure of complexes **14** (L = PCy$_3$, IMes) in the solid state; the structure of one of them is shown in Figure 2.[19] The Cr–C1 bond length (1.994(3) Å) is almost identical to that of the starting complex **12** (1.9877(12) and 1.9973(13) Å; two independent molecules

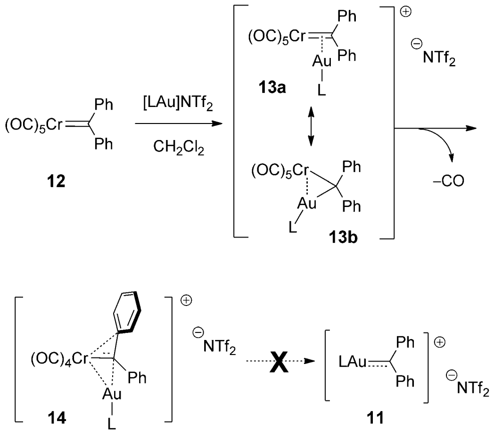

Scheme 4. Attempted transmetalation of **12** with $[LAu]^+$ also affords hetero-bimetallic complexes, even though the chromium entity has to abandon one of the CO ligands; the resulting complex **14** is stabilized by charge delocalization over Cr, Au, the carbene center, and, to a small extent, even one of the arene C_{ipso} positions.

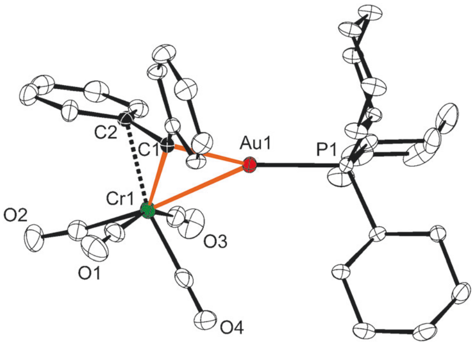

Figure 2. Structure of complex **14** ($L = PCy_3$) in the solid state; only the cationic entity is shown, whereas the escorting $[NTf_2]^-$ has been removed for clarity. For the entire structure, see the Supporting Information.

in the unit cell).[19] The carbene center is only slightly pyramidalized by the additional contact with the gold atom; the C1−Au distance (2.135(3) Å) falls into the range observed in related *gem*-bimetallic arrays.[24,25] The gold fragment is notably slipped away from the chromium center, residing almost perpendicularly over the carbene carbon atom (Cr1–C1–Au1, 82.28(12)°).[33] The rather long Cr⋯Au distance (2.7185(6) Å) speaks for an only weakly attractive interaction between the early- and late-transition-metal atoms.

The most unusual structural aspect of **14** is the contact between the chromium and the *ipso* carbon atom of the phenyl ring, which explains why this position is strongly shielded, and why the arene cannot rotate. Although the Cr1−C2 distance (2.281(10 Å) is too long for an efficient electronic communication, the interaction must be somehow constructive, because it prevents the collapse of the complex with release of the targeted free gold carbenoid **11**, even though one CO ligand has been spontaneously lost at −50 °C.

Qualitatively, this outcome can be rationalized as follows: Side-on coordination of $[LAu]^+$ deprives the Cr=C bond of **12** of a significant amount of electron density that is only partly compensated by back-donation from gold into the antibonding orbital (otherwise, rehybridization expressed by pyramidalization of C1 would be more prominent). The imparted partial positive charge reduces the ability of the chromium center to share its electrons with five electron-withdrawing CO ligands. To counterbalance this deficit, one of them is released and replaced by the best donor in vicinity, which turns out to be the π lobe of the *ipso* carbon atom of the adjacent aromatic ring. Although the electronic gain is likely to be minute,[34] the formation of an unstabilized gold carbenoid must be even less favorable. This interpretation also explains why the reaction of $[LAu]^+$ with the analogous tungsten complex **9**, which has a much higher core electron density, does not result in loss of CO, but stops at the initially formed pentacarbonyl complexes of type **10**.

DFT calculations at the RI-BP86/def2-TZVP + D3 level of theory substantiate the conclusions drawn from the structural and spectral data.[35] The calculated and experimental structures of **10**, **13**, and **14** are in excellent agreement; likewise, the NMR shifts were well reproduced with the B3LYP hybrid functional using an extended basis set and added relativistic corrections. In case of **14** ($L = PCy_3$), fragment molecular orbital analyses show that the LUMO of the gold entity accepts substantial electron density (ca. 0.45 electrons) from the HOMO and HOMO-1 of the $\{(CO)_4Cr{=}CPh_2\}$ fragment; nevertheless, the latter retains true carbene character as evident from simultaneous σ donation and π back-donation. Thus, the overall bonding situation in **14** is in fact best described as a chromium carbene that carries an η^2-bound, but visibly slipped, gold unit. Small Wiberg bond indices suggest that the Au–Cr, Au–C1, and Cr–C2 interactions are feeble. Likewise, natural bond order analysis and the topological characteristics of the electron density confirm that the *ipso* carbon atom, though remarkably shielded, is not engaged in a significant bonding interaction with the metal center.[35]

Our investigations confirm that gold-for-chromium carbene transfer is exceptionally facile, but only in the Fischer carbene series. As soon as stabilization of charge density by an adjacent heteroatom substituent is lacking, the transmetalation derails. Bimetallic complexes are formed instead, which have little in common with the unstabilized gold carbenoids that were invoked in many mechanistic discussions of π-acid catalysis. At this point, such species basically remain elusive from the experimental vantage point, as three of the very best entries into carbene complexes so far failed to deliver these species (diazo decomposition, cyclopropene rearrangement, carbene transfer). Even the cyclobutenyl intermediate **2**,[6] as the example that comes closest to this ideal, benefits from charge delocalization over several positions of a non-classical cation.[1,7] In future studies, we will strive to learn how much stabilization is necessary to enable full characterization of a pertinent donor-free gold carbenoid.

Received: October 10, 2013

Keywords: carbene complexes · chromium · dimetalation · gold · tungsten

[1] a) A. Fürstner, P. W. Davies, *Angew. Chem.* **2007**, *119*, 3478–3519; *Angew. Chem. Int. Ed.* **2007**, *46*, 3410–3449; b) A. Fürstner, *Chem. Soc. Rev.* **2009**, *38*, 3208–3221.

[2] D. J. Gorin, F. D. Toste, *Nature* **2007**, *446*, 395–403.

[3] E. Jiménez-Núñez, A. M. Echavarren, *Chem. Rev.* **2008**, *108*, 3326–3350.

[4] a) A. S. K. Hashmi, *Angew. Chem.* **2010**, *122*, 5360–5369; *Angew. Chem. Int. Ed.* **2010**, *49*, 5232–5241; b) L.-P. Liu, G. B. Hammond, *Chem. Soc. Rev.* **2012**, *41*, 3129–3139; c) H. G. Raubenheimer, H. Schmidbaur, *S. Afr. J. Sci.* **2011**, *107*, 31–43.

[5] For pertinent comments, see: D. A. Dixon, *J. Am. Chem. Soc.* **2011**, *133*, 19257; for the necessity to calibrate the computations, see Ref. [12].

[6] R. E. M. Brooner, T. J. Brown, R. A. Widenhoefer, *Angew. Chem.* **2013**, *125*, 6379–6381; *Angew. Chem. Int. Ed.* **2013**, *52*, 6259–6261.

[7] a) A. Fürstner, H. Szillat, B. Gabor, R. Mynott, *J. Am. Chem. Soc.* **1998**, *120*, 8305–8314; b) A. Fürstner, F. Stelzer, H. Szillat, *J. Am. Chem. Soc.* **2001**, *123*, 11863–11869; c) A. Fürstner, P. W. Davies, T. Gress, *J. Am. Chem. Soc.* **2005**, *127*, 8244–8245.

[8] A. Fürstner, L. Morency, *Angew. Chem.* **2008**, *120*, 5108–5111; *Angew. Chem. Int. Ed.* **2008**, *47*, 5030–5033.

[9] a) A. Fedorov, L. Batiste, A. Bach, D. M. Birney, P. Chen, *J. Am. Chem. Soc.* **2011**, *133*, 12162–12171; b) A. Fedorov, P. Chen, *Organometallics* **2009**, *28*, 1278–1281; c) A. Fedorov, P. Chen, *Organometallics* **2010**, *29*, 2994–3000; for relevant solution chemistry, see: d) D. H. Ringger, P. Chen, *Angew. Chem.* **2013**, *125*, 4784–4787; *Angew. Chem. Int. Ed.* **2013**, *52*, 4686–4689.

[10] G. Seidel, R. Mynott, A. Fürstner, *Angew. Chem.* **2009**, *121*, 2548–2551; *Angew. Chem. Int. Ed.* **2009**, *48*, 2510–2513.

[11] Gold carbenoids that are stable enough for NMR analysis could not be obtained from cyclopropenes devoid of oxygen substituents; only oligomerization was observed.

[12] D. Benitez, N. D. Shapiro, E. Tkatchouk, Y. Wang, W. A. Goddard, F. D. Toste, *Nat. Chem.* **2009**, *1*, 482–486.

[13] For gold diazine complexes from $[(C_6F_5)Au(SC_4H_8)]$ and Ph_2CN_2, see: S. Bordoni, L. Busetto, M. C. Cassani, V. G. Albano, P. Sabatino, *Inorg. Chim. Acta* **1994**, *222*, 267–273.

[14] Diazine formation can occur with and without discrete metal carbene intermediates; see: a) H. Werner, P. Schwab, E. Bleuel, N. Mahr, B. Windmüller, J. Wolf, *Chem. Eur. J.* **2000**, *6*, 4461–4470; b) C. J. Abelt, J. M. Pleier, *J. Am. Chem. Soc.* **1989**, *111*, 1795–1799.

[15] For the conversion of Ph_2CN_2 into mono- and dicopper carbene complexes with a terminal or a bridging carbene ligand, see: X. Dai, T. H. Warren, *J. Am. Chem. Soc.* **2004**, *126*, 10085–10094.

[16] a) R. Aumann, E. O. Fischer, *Chem. Ber.* **1981**, *114*, 1853–1857; b) E. O. Fischer, M. Böck, R. Aumann, *Chem. Ber.* **1983**, *116*, 3618–3623; c) E. O. Fischer, M. Böck, *J. Organomet. Chem.* **1985**, *287*, 279–285.

[17] In their pioneering work (Ref. [16]), Fischer and co-workers used Au(III) as the reagent in the transmetalation step, even though Au(I) carbenes were obtained; the exact cause for the reduction remained unelucidated.

[18] a) M. Fananás-Mastral, F. Aznar, *Organometallics* **2009**, *28*, 666–668; b) C. E. Strasser, E. Stander-Grobler, O. Schuster, S. Cronje, H. G. Raubenheimer, *Eur. J. Inorg. Chem.* **2009**, 1905–1912; c) F. Kessler, N. Szesni, C. Maaß, C. Hohberger, B. Weibert, H. Fischer, *J. Organomet. Chem.* **2007**, *692*, 3005–3018; d) S.-T. Liu, T.-Y. Hsieh, G.-H. Lee, S.-M. Peng, *Organometallics* **1998**, *17*, 993–995; see also: e) M. Gómez-Gallego, M. J. Mancheño, M. A. Sierra, *Acc. Chem. Res.* **2005**, *38*, 44–53.

[19] The solid-state structures of complexes **8**, **10** (L = Ph_3P), **12** ($Ph_2C{=}Cr(CO)_5$), and **14** (L = IMes) together with a complete set of crystallographic abstracts are contained in the Supporting Information. CCDC 963592, 963593, 963594, 963595, 963596, and 963597 contain the supplementary crystallographic data for this paper. These data can be obtained free of charge from The Cambridge Crystallographic Data Centre via www.ccdc.cam.ac.uk/data_request/cif.

[20] For the structure of the closely related complex formulated as $[ClAu{=}C(Ph)(NMe_2)]$, see: U. Schubert, K. Ackermann, R. Aumann, *Cryst. Struct. Comm.* **1982**, *11*, 591–594; we have previously emphasized that this complex might be more adequately viewed as an iminium cation in the coordination sphere of a gold fragment; see Ref. [1,10].

[21] Reference is also made to the carbenoid complex $[(Ph_3P)AuCH_2Cl]$, in which the C–Au distance (2.088(9) Å) falls in the typical range for a single bond, but the C–Cl bond (1.68(1) Å) is unusually short; see: D. Steinborn, S. Becke, R. Herzog, M. Günter, R. Kircheisen, H. Stoeckli-Evans, C. Bruhn, *Z. Anorg. Allg. Chem.* **1998**, *624*, 1303–1307.

[22] The major decomposition products (GC–MS) are tetraphenylethane (45 %) and Ph_2CH_2 (31 %); moreover, small amounts of $Ph_2C{=}CPh_2$ and $Ph_2C{=}O$ could also be identified.

[23] The reported structure contains two independent molecules in the unit cell; see: C. P. Casey, T. J. Burkhardt, C. A. Bunnell, J. C. Calabrese, *J. Am. Chem. Soc.* **1977**, *99*, 2127–2134.

[24] a) G. Seidel, C. W. Lehmann, A. Fürstner, *Angew. Chem.* **2010**, *122*, 8644–8648; *Angew. Chem. Int. Ed.* **2010**, *49*, 8466–8470; b) M. Alcarazo, C. W. Lehmann, A. Anoop, W. Thiel, A. Fürstner, *Nat. Chem.* **2009**, *1*, 295–301; c) M. Alcarazo, K. Radkowski, G. Mehler, R. Goddard, A. Fürstner, *Chem. Commun.* **2013**, *49*, 3140–3142, and references therein.

[25] H. Schmidbaur, *Chem. Soc. Rev.* **1995**, *24*, 391–400.

[26] Computational studies suggest that transmetalation of prototype Fischer chromium carbene complexes with Pd, Cu, or Rh proceeds via hetero-bimetallic intermediates; see: I. Fernández, M. J. Mancheño, R. Vicente, L. A. López, M. A. Sierra, *Chem. Eur. J.* **2008**, *14*, 11222–11230.

[27] For a remotely related bimetallic W/Au complex derived from an anionic alkoxy Fischer carbene, see: H. G. Raubenheimer, M. W. Esterhuysen, A. Timoshkin, Y. Chen, G. Frenking, *Organometallics* **2002**, *21*, 3173–3181.

[28] For the formation of bridging carbenes and carbynes by coordination of a suitable metal fragment onto terminal carbenes, see: "Advances in Metal Carbene Chemistry": F. G. A. Stone in *NATO ASI Ser. Ser. C*, *Vol. 269* (Ed.: U. Schubert), Kluwer Academic Publishers, Dordrecht, **1989**, pp. 11–25.

[29] E. O. Fischer, W. Held, F. R. Kreißl, A. Frank, G. Huttner, *Chem. Ber.* **1977**, *110*, 656–666.

[30] Resonances of the carbene carbon atom: **12**: 397.7 ppm; **13**, L = PCy_3: 307.3 ppm (d, $J_{P,C} = 33$ Hz).

[31] Some $[Cr(CO)_6]$ precipitated from the solution; other by-products could not be identified.

[32] The complex decomposes at RT within a few hours to give tetraphenylethene (89 %) and benzophenone (11 %) as the major products according to GC–MS analysis.

[33] Coordination of $[LAu]^+$ to a polarized π bond results in slippage and accumulation of positive charge density on the organic ligand; see: A. Fürstner, M. Alcarazo, R. Goddard, C. W. Lehmann, *Angew. Chem.* **2008**, *120*, 3254–3258; *Angew. Chem. Int. Ed.* **2008**, *47*, 3210–3214.

[34] A partial phenyl cation character would result in loss of resonance stabilization; the X-ray structure of **14** shows slight perturbations of the locked phenyl ring, in which one of the C_{ipso}–C_{ortho} bonds is notably elongated (C2–C7, 1.431(5) Å).

[35] For detailed information, see the Supporting Information.

Angewandte Chemie
Eine Zeitschrift der Gesellschaft Deutscher Chemiker

Supporting Information

69451 Weinheim, Germany

Gold Carbenoids: Lessons Learnt from a Transmetalation Approach**

*Günter Seidel, Barbara Gabor, Richard Goddard, Berit Heggen, Walter Thiel, and Alois Fürstner**

anie_201308842_sm_miscellaneous_information.pdf

Computational Section

Computational Methods:

Geometry optimizations were carried out using the BP86 functional[1,2] in combination with the def2-TZVP basis set.[3] For the gold atom, the 60 inner-shell core electrons were replaced by an effective core potential (ECP) generated for the neutral atom using quasi-relativistic methods.[4] The remaining explicitly treated electrons were described using the corresponding def2-ECP basis set. Additionally the empirical Grimme-type dispersion corrections were also incorporated using the latest parametrization (D3).[5] The resolution of identity (RI) approximation[6-8] was employed for efficient computation. This computational setup had already proved to be efficient and reliable for the study of gold complexes.[9-11] The located stationary points were characterized as minima by evaluating the harmonic vibrational frequencies computed at the same level (RI-BP86/def2-TZVP+D3). These computations were performed using the TURBOMOLE suite of programs (version 6.3).[12, 13]

In order to get insight into the electronic structure of the complexes, a Natural Population Analysis (NPA) was carried out at RI-BP86/def2-TZVP+D3 level. The Wiberg bond indices for selected bonds were evaluated at BP86/LANL2DZ level using the NBO code version 3.1[14] as implemented in the Gaussian 09 suite of programs.[15] Additionally, a fragment analysis was performed using the Amsterdam Density Functional (ADF) program package.[16-18] In this analysis, the complexes are built from user-defined fragments. The molecular orbitals of the fragments are expanded in terms of Slater-type orbitals (STOs), employing a triple-ζ basis set with one polarization function (TZP). The resulting symmetrized fragment orbitals (SFOs) are used as new basis functions to recompute the electronic structure of the complexes. These calculations were also corrected for relativistic effects using the zero-order regular approximation (ZORA) approach.[19, 20]

The Atoms-in-Molecule (AIM) analysis[21] was performed based on the geometries optimized at the BP86/def2-TZVP level (with an effective core potential for Au as described above). For the generation of the wave function, a single-point Gaussian 09 calculation was run (B3LYP/6-311+G** with SDD basis set and pseudopotential for Au). The AIM calculation itself was done by using AIMAll.[22] The AIM analysis allows the identification of bonds between atoms based on the gradient of the electron density. The characteristic bond critical points are defined as saddle points where the gradient of the electron density is zero in all directions and its second derivatives are negative in two directions and positive in the direction of the bound atoms.[21]

Isotropic chemical shielding constants were computed within the GIAO ansatz.[23] Besides the GGA functional chosen for the optimization (BP86) we also applied the hybrid functional B3LYP as recommended.[24] For calculations performed with Turbomole, a smaller basis had to be applied due to technical reasons (def2-SVP for Au, C, H, O, P; def2-TZVP for Cr and C1, C_{ipso}, C'_{ipso}; corresponding core potential for Au). To include relativistic effects chemical shieldings were calculated using ADF as well (BP86/TZP, no core potentials). To perform calculations with larger basis sets, Gaussian 09 was employed choosing the SDD basis set and potential for Au and the 6-311+G** basis set for all other atoms.

References

1. A. D. Becke, *Phys. Rev. A* **1988**, *38*, 3098-3100.
2. J. P. Perdew, *Phys. Rev. B* **1986**, *33*, 8822-8824.
3. F. Weigend, R. Ahlrichs, *Phys. Chem. Chem. Phys.* **2005**, *7*, 3297-3305.
4. D. Andrae, U. Häussermann, M. Dolg, H. Stoll, H. Preuss, *Theor. Chim. Acta* **1990**, *77*, 123-141.
5. S. Grimme, J. Antony, S. Ehrlich, H. Krieg, *J. Chem. Phys.* **2010**, *132*, 154104.
6. K. Eichkorn, O. Treutler, H. Öhm, M. Häser, R. Ahlrichs, *Chem. Phys. Lett.* **1995**, *242,* 652-660.
7. K. Eichkorn, F. Weigend, O. Treutler, R. Ahlrichs, *Theor. Chem. Acc.* **1997**, *97*, 119-124.
8. F. Weigend, *Phys. Chem. Chem. Phys.* **2002**, *4*, 4285-4291.
9. S. Flügge, A. Anoop, R. Goddard, W. Thiel, A. Fürstner, *Chem. Eur. J.* **2009**, *15*, 8558-8565.
10. M. Alcarazo, T. Stork, A. Anoop, W. Thiel, A. Fürstner, *Angew. Chem. Int. Ed*. **2010**, *49*, 2542-2546.
11. H. Teller, M.Corbet, L. Mantilli, G. Gopakumar, R. Goddard, W. Thiel, A. Fürstner, *J. Am. Chem. Soc.* **2012**, *134*, 15331-15342.
12. R. Ahlrichs, M. Bär, M. Häser, H. Horn, C. Kölmel, *Chem. Phys. Lett.* **1989**, *162*, 165-169.
13. TURBOMOLE V6.3 **2011**, a development of University of Karlsruhe and Forschungszentrum Karlsruhe GmbH, 1989-2007, TURBOMOLE GmbH, since 2007; available from www.turbomole.com
14. NBO Version 3.1, E. D. Glendening, A. E. Reed, J. E. Carpenter, F. Weinhold.
15. Gaussian 09, Revision B.01, M. J. Frisch, G. W. Trucks, H. B. Schlegel, G. E. Scuseria, M. A. Robb, J. R. Cheeseman, G. Scalmani, V. Barone, B. Mennucci, G. A. Petersson, H. Nakatsuji, M. Caricato, X. Li, H. P. Hratchian, A. F. Izmailov, J. Bloino, G. Zheng, J. L. Sonnenberg, M. Hada, M. Ehara, K. Toyota, R. Fukuda, J. Hasegawa, M. Ishida, T. Nakajima, Y. Honda, O. Kitao, H. Nakai, T. Vreven, J. A. Montgomery Jr., J. E. Peralta, F. Ogliaro, M. Bearpark, J. J. Heyd, E. Brothers, K. N. Kudin, V. N. Staroverov, R. Kobayashi, J. Normand, K. Raghavachari, A. Rendell, J. C. Burant, S. S. Iyengar, J. Tomasi, M. Cossi, N. Rega, J. M. Millam, M. Klene, J. E. Knox, J. B. Cross, V. Bakken, C. Adamo, J. Jaramillo, R. Gomperts, R. E. Stratmann, O. Yazyev, A. J. Austin, R. Cammi, C. Pomelli, J. W. Ochterski, R. L. Martin, K. Morokuma, V. G. Zakrzewski, G. A. Voth, P. Salvador, J. J. Dannenberg, S. Dapprich, A. D. Daniels, Ö. Farkas, J. B. Foresman, J. V. Ortiz, J. Cioslowski, D. J. Fox, Gaussian, Inc., Wallingford CT, **2010**.
16. C. Fonseca Guerra, J. G. Snijdres, G. te Velde, E. J. Baerends *Theor. Chem. Acc.* **1998**, *99*, 391-

403.

17. G. te Velde, F. M. Bickelhaupt, E. J. Baerends, C. Fonseca Guerra, S. J. A. van Gisbergen, J. G. Snijders, T. Ziegler, *J. Comput. Chem.* **2001**, *22*, 931-967.

18. ADF 2012.01, SCM, Theoretical Chemistry, Vrije Universiteit Amsterdam, The Netherlands, **2012**; www.scm.com

19. E. van Lenthe, E. J, Baerends, J. G. Snijders, *J. Chem. Phys.* **1994**, *101*, 9783.

20. E. van Lenthe, A. E. Ehlers, E. J. Baerends, *J. Chem. Phys.* **1999**, *110*, 8943.

21. R. F. W. Bader, *Acc. Chem. Res.* **1985**, *18*, 9-15.

22. AIMAll Version 13.05.06, T. A. Keith, TK Gristmill Software, Overland Park KS, USA, **2013**; aim.tkgristmill.com

23. K. Wolinski, J. F. Hinton, P. Pulay, *J. Am. Chem. Soc.* **1990**, *112*, 8251-8260.

24. M. Bühl, T. van Mourik, *WIREs Comput. Mol. Sci.* **2011**, *1*, 634-647.

Computational Results:

We have applied Density Functional Theory (DFT) to study the electronic structure of complexes **13** and **14** (see main paper). The optimized geometries of these complexes are illustrated in Figures S-7 and S-8, respectively. They are in good agreement with the X-ray structures, as can be seen from the comparison of selected calculated and experimental geometrical parameters in Tables S-3 and S-4.

Table S-3. Selected bond lengths in complex **14** [experimental (X-ray structure) vs. calculated (RI-BP86/def2-TZVP+D3)].

bond	bond length in Å experimental	bond length in Å calculated
Au-P	2.331	2.340
Au-C1	2.136	2.171
Au-Cr	2.718	2.720
C1-Cr	1.993	1.979
C1-C_{ipso}	1.469	1.470
C1-C'_{ipso}	1.476	1.460
Cr-C_{ipso}	2.272	2.330

Table S-4. Selected bond angles in complexes **13** and **14** at the RI-BP86/def2-TZVP+D3 level.

angle	13	14
P-Au-Cr	151.1	158.3
P-Au-C1	157.7	155.7
C1-Au-Cr	51.2	46.1
Cr-C1-O	172.6	175.9
CO-Cr-CO	169.3	85.7
C_{ipso}-C1-C'_{ipso}	113.3	121.8
Cr-C1-C_{ipso}	127.1	83.6

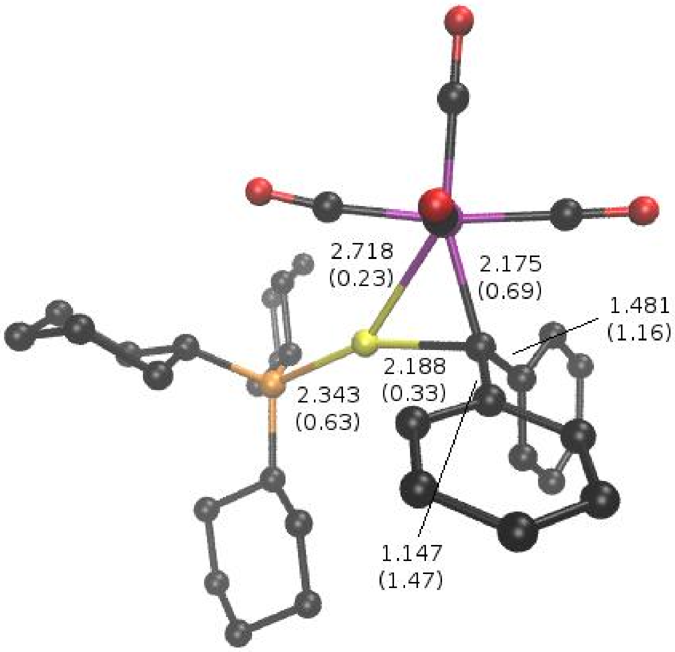

Figure S-7 Optimized geometry of complex **13** at RI-BP86/def2-TZVP+D3 level. The hydrogen atoms are omitted for clarity (color code: black=carbon, violet=chromium, yellow=gold, red=oxygen, orange=phosphorous). Selected bond length (Å) and Wiberg bond indices (in parentheses) are also given.

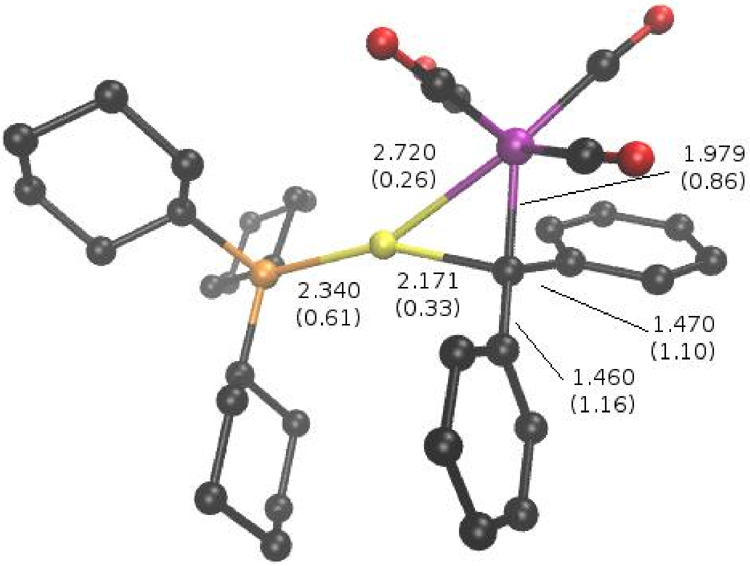

Figure S-8 Optimized geometry of complex **14** at RI-BP86/def2-TZVP+D3 level. The hydrogen atoms are omitted for clarity (color code: black=carbon, violet=chromium, yellow=gold, red=oxygen, orange=phosphorous). Selected bond length (Å) and Wiberg bond indices (in parentheses) are also given.

Fragment analysis. In order to gain insight into the electronic structure of the complexes, a fragment molecular orbital analysis has been performed. In this analysis, the molecule is built from user-defined fragments. For each of them, fragment orbitals (FOs) are calculated starting from atomic orbitals (AOs). These FOs are used as new basis functions to recompute the molecular orbitals (MOs) of the full complexes. We have adopted two different fragment analysis schemes for complexes **13** and **14**. In the first one (fragmentation A), the complex after full geometry optimization is divided into a $[P(Cy)_3Au]^+$ fragment and a $[C(Ph)_2Cr(CO)_n]$ fragment. In the second scheme (fragmentation B), the complex is divided into a $[Cr(CO)_n]$ fragment and a $[C(Ph)_2P(Cy)_3Au]^+$ fragment (see Scheme S-1). MOs are generated for each of these fragments, and the total electronic structure is then recomputed based on the fragment orbitals. In this way it is possible to determine the contributions of the fragment orbitals to the MOs of the corresponding complex.

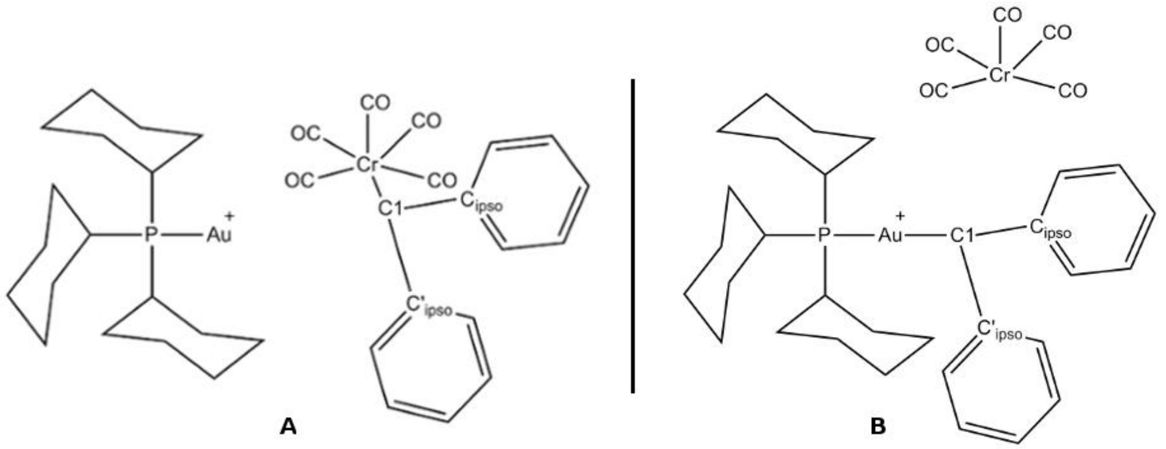

Scheme S-1 Representation of the two fragmentation schemes adopted for complex **13**.

Fragmentation A. The gross populations of the FOs (from LUMO+1 to HOMO-3) in complexes **13** and **14** are listed in Tables S-5 and S-6, respectively, and the shapes of selected FOs of complex **14** are represented in Figure S-9. We adopted the selection criterion that the population of the FO had to change by at least ±0.1 electrons upon recombination. The lowest unoccupied molecular orbital (LUMO) of the gold fragment, which has a large contribution from the 6s atomic orbital of the metal atom ($\%s_{Au}$=44), receives 0.51 and 0.45 electrons in case of complex **13** and **14**, respectively. The charge is donated mainly from the HOMO-1 of the $[C(Ph)_2Cr(CO)_5]$ fragment in case of complex **13**, and from the HOMO and HOMO-1 of the $[C(Ph)_2Cr(CO)_4]$ fragment in case of complex **14** (see Tables S-5 and S-6). The main contributions from FOs (single contribution larger than 0.1) to the orbitals LUMO to HOMO-3 are given in Table S-7 for both complexes. Please note that the MOs resulting from the interaction of fragment orbitals have large contributions from the $[C(Ph)_2Cr(CO)_5]$ fragment.

In case of complex **13**, HOMO-1 and HOMO-3 of the [C(Ph)$_2$Cr(CO)$_5$] fragment contribute 48% and 17%, respectively, while there are only minor contributions from the HOMO-2 (8%) and the LUMO (6%) of the [P(Cy)$_3$Au]$^+$ fragment. In case of complex **14**, HOMO-1 and HOMO of the [C(Ph)$_2$Cr(CO)$_4$] fragment contribute 43% and 11%, respectively, while there is only 7% contribution from the LUMO of the [P(Cy)$_3$Au]$^+$ fragment. Hence, as there is no strong orbital mixing between the [P(Cy)$_3$Au]$^+$ and [C(Ph)$_2$Cr(CO)$_n$] fragments, the bonding situation can be described as a chromium-carbene complex with a weakly coordinating gold unit (η^2 binding mode). This is also well reflected in the very low Wiberg bond indices derived for these bonds (see Figures S-7 and S-8).

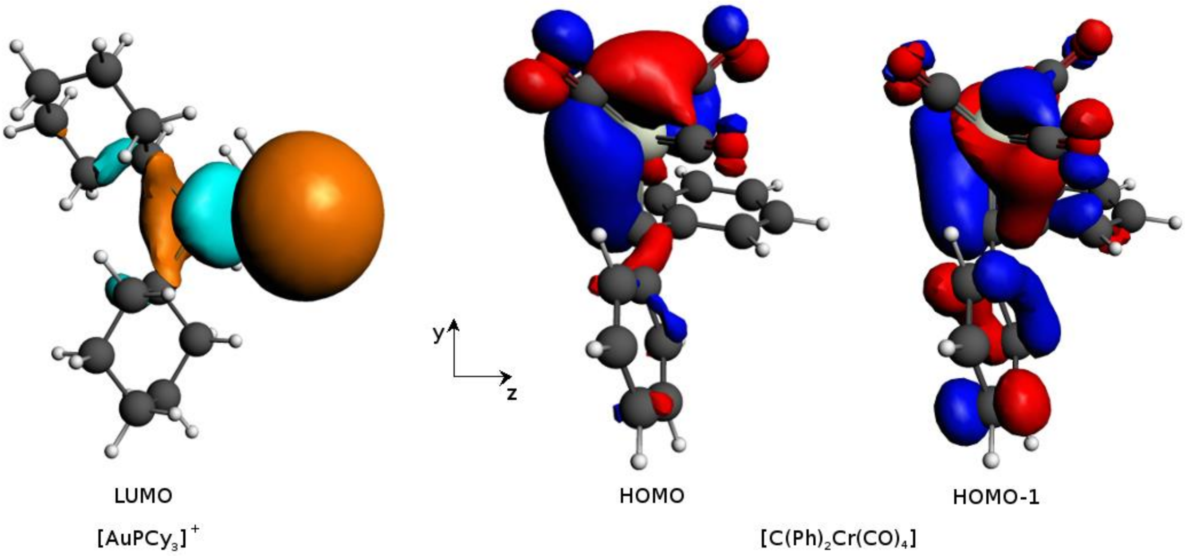

Figure S-9 Shape of selected fragment orbitals (fragmentation A) of complex **14** at BP86/TZP(ZORA) level. The local axis frame chosen for the analysis is also specified in the figure.

Table S-5. Fragment analysis of complex **13** (fragmentation A). The gross populations (summation over all MOs) of frontier fragment orbitals are given at BP86/TZP(ZORA) level. The dominant AO contributions are mentioned if they are mainly localized at Au, Cr or C1.

Orbitals of [AuPCy$_3$]$^+$ fragment	SFO gross populations	Orbitals of [C(Ph)$_2$Cr(CO)$_5$] fragment	SFO gross populations
LUMO+1 (6p$_y$)	0.06	LUMO+1	0.02
LUMO (6s)	0.51	LUMO (C1 2p$_y$)	0.15
HOMO	2.00	HOMO (Cr 3d$_{xz}$)	1.98
HOMO-1	1.99	HOMO-1 (π)	1.70
HOMO-2 (6s/5d)	1.92	HOMO-2 (Cr 3d$_{x2-z2}$)	1.99
HOMO-3	2.00	HOMO-3 (σ)	1.96

Table S-6. Fragment analysis of complex **14** (fragmentation A). The gross populations (summation over all MOs) of frontier fragment orbitals are given at BP86/TZP(ZORA) level. The main AO contributions are mentioned if they are mainly localized at Au, Cr or C1.

Orbitals of $[AuPCy_3]^+$ fragment	FO gross populations	Orbitals of $[C(Ph)_2Cr(CO)_4]$ fragment	FO gross populations
LUMO+1 ($6p_y$)	0.05	LUMO+1	0.03
LUMO (6s)	0.45	LUMO (C1 $2p_y$)	0.11
HOMO	2.00	HOMO (Cr $3d_{xz}$)	1.82
HOMO-1	1.99	HOMO-1 (π)	1.85
HOMO-2 (6s/5d)	1.96	HOMO-2 (Cr $3d_{x2-y2}$)	1.99
HOMO-3	2.00	HOMO-3 (σ)	1.97

Table S-7. Contributions of fragment orbitals (fragmentation scheme A, contributions larger than 0.1) to molecular orbitals of both complexes, respectively.

molecular orbital	complex 13	complex 14
LUMO	0.86 LUMO $[C(Ph)_2Cr(CO)_5]$	0.85 LUMO $[C(Ph)_2Cr(CO)_4]$
HOMO	0.95 HOMO $[C(Ph)_2Cr(CO)_5]$	0.66 HOMO, 0.27 HOMO-1 $[C(Ph)_2Cr(CO)_4]$
HOMO-1	0.48 HOMO-1, 0.17 HOMO-3 $[C(Ph)_2Cr(CO)_5]$	0.87 HOMO-2 $[C(Ph)_2Cr(CO)_4]$
HOMO-2	0.86 HOMO-2 $[C(Ph)_2Cr(CO)_5]$	0.47 HOMO-1, 0.11 HOMO $[C(Ph)_2Cr(CO)_4]$
HOMO-3	0.61 HOMO-3, 0.11 HOMO-1 $[C(Ph)_2Cr(CO)_5]$	0.40 HOMO-2 $[AuPCy_3]^+$, 0.23 HOMO-3, 0.15 HOMO-6 $[C(Ph)_2Cr(CO)_4]$

Fragmentation B. The gross populations of the frontier FOs (LUMO+1 through HOMO-3) in complexes **13** and **14** are listed in Tables S-8 and S-9, respectively, and the shapes of selected FOs of complexes **13** and **14** are represented in Figures S-10 and S-11, respectively. Again, we include all fragment frontier orbitals with a change of population of at least ±0.1 electrons upon recombination to form the MOs of the full complexes. The LUMO of fragment $[AuPCy_3C(Ph)_2]^+$ has large contributions from the $2p_z$ orbital of C1 (39% and 44% in complex **13** and **14**, respectively). Additionally, the LUMO+1 of this fragment has small contributions from the 2p orbital of both ipso carbon atoms (around 10% each for C2 and C8). In the case of complex **13**, the HOMO of the $[AuPCy_3C(Ph)_2]^+$ fragment has large contributions from the $2p_y$ orbital located at C1 (20%) with a minor contribution from the $5d_{xz}$ orbital at Au (5%). Correspondingly, for complex **14** the main contributions to the HOMO arise from a $2p_y$ orbital located at C1 (19%) complemented by minor contributions from the 6s orbital located at Au (7%). For both complexes, the HOMO-1 is mainly localized around Au, with main contributions from 6s (23-26%) and 5d (14-19%). In both complexes, this fragment receives electrons from the HOMO of the $[Cr(CO)_n]$ fragment, and at the same time there is a considerable amount of back-donation to the LUMO of the latter fragment (cf. Tables S-8 and S-9). The resulting MOs have contributions from both fragments. The main contributions (larger than 0.1) of FOs to the orbitals LUMO up to HOMO-3 are listed in Table S-10 for both complexes. The HOMO-1 of complex **13** has the following contributions from the respective FOs: 39% from the HOMO of the $[Cr(CO)_5]$ fragment, 15% from the LUMO of the $[AuPCy_3C(Ph)_2]^+$ fragment. Similarly the HOMO-3 of complex **13** has main contributions from the HOMO of the $[AuPCy_3C(Ph)_2]^+$ fragment (65%) and from the LUMO and the HOMO-1 of the chromium fragment (4% each).

For complex **14**, the LUMO has the following contributions from the respective FOs: 49% from the LUMO of $[AuPCy_3C(Ph)_2]^+$ fragment, 24% from the HOMO of the chromium fragment. The HOMO-2 of complex **14** has mainly contributions from the HOMO and HOMO-2 of $[Cr(CO)_4]$ (25% and 24%, respectively) and the LUMO+1 of $[AuPCy_3C(Ph)_2]^+$ (19%). This clearly indicates σ-bonding/π-backbonding interactions between the chromium and carbene units in both complexes, which are also reflected in the electron transfers between these fragments (Tables S-8 and S-9). The Wiberg bond indices (Figures S-7 and S-8) also suggest strong bonding interactions between Cr and C1. By contrast, according to the orbital interaction analysis and the Wiberg bond indices (WBI), there are no significant bonding interactions between Cr and C_{ipso} in complex **13** (WBI = 0.02) and also not in complex **14** (WBI=0.15) despite the fact that the C_{ipso} atom is much closer to Cr in complex **14**.

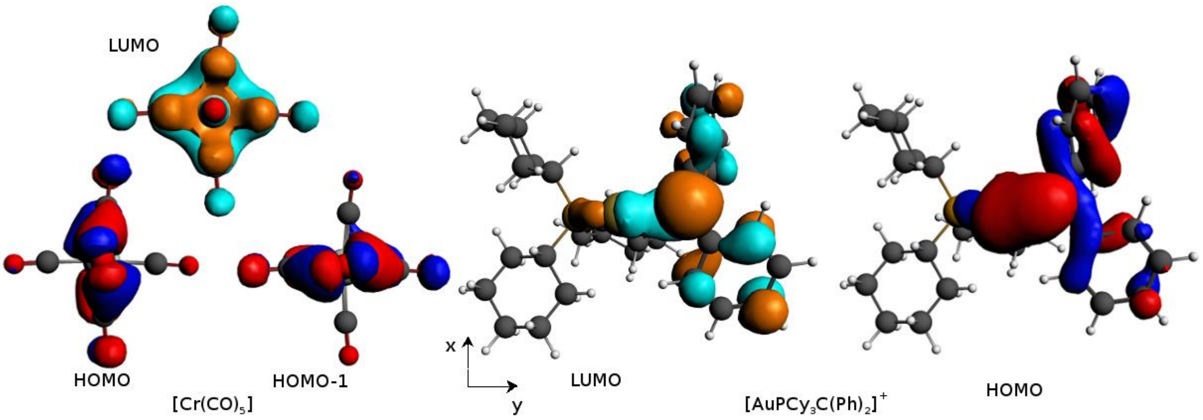

Figure S-10 Shape of selected fragment orbitals (fragmentation B) of complex **13** at BP86/TZP(ZORA) level. The local axis frame chosen for the analysis is also specified in the figure.

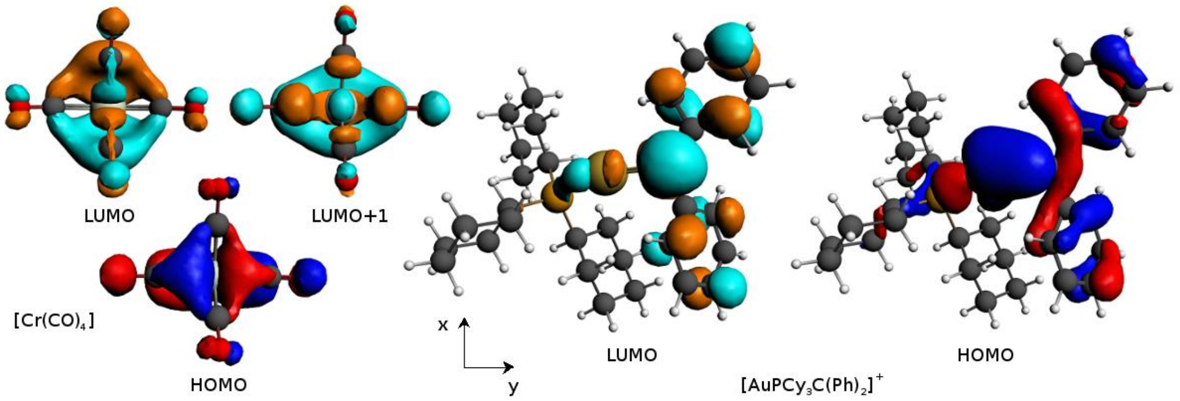

Figure S-11 Shape of selected fragment orbitals (fragmentation scheme B) of complex **14** at BP86/TZP(ZORA) level. The local axis frame chosen for the analysis is also specified in the figure.

Table S-8. Fragment analysis (fragmentation scheme B) of complex **13**: The gross populations (summed over all MOs) of frontier fragment orbitals are given at BP86/TZP level.

Orbitals of $[AuPCy_3C(Ph)_2]^+$ fragment	FO gross populations	Orbitals of $[Cr(CO)_5]$ fragment	FO gross populations
LUMO+1	0.00	LUMO+1	0.01
LUMO (C1 $2p_z$)	0.49	LUMO ($3d_{z2}$)	0.40
HOMO (C1 $2p_y$)	1.73	HOMO ($3d_{xz}$)	1.59
HOMO-1 (Au 6s/5d)	1.96	HOMO-1 ($3d_{yz}$)	1.86
HOMO-2	2.00	HOMO-2 ($3d_{xy}$)	1.99
HOMO-3	2.00	HOMO-3	1.99

Table S-9. Fragment analysis (fragmentation B) of complex **14**: The gross populations (summation over all MOs) of frontier fragment orbitals are given at BP86/TZP level.

Orbitals of $[AuPCy_3C(Ph)_2]^+$ fragment	FO gross populations	Orbitals of $[Cr(CO)_4]$ fragment	FO gross populations
LUMO+1	0.04	LUMO+1 ($3p_z$)	0.25
LUMO (C1 $2p_z$)	0.71	LUMO ($3d_{xy}$)	0.39
HOMO (C1 $2p_y$)	1.63	HOMO ($3d_{xz}$)	1.28
HOMO-1 (Au 6s/5d)	1.98	HOMO-1 ($3d_{x2-y2}$)	1.96
HOMO-2	2.00	HOMO-2 ($3d_{yz}$)	1.96
HOMO-3	1.99	HOMO-3	1.99

Table S-10. Contributions of fragment orbitals (fragmentation B, contributions larger than 0.1) to molecular orbitals of both complexes.

molecular orbital	complex 13	complex 14
LUMO	0.64 LUMO $[AuPCy_3C(Ph)_2]^+$, 0.14 HOMO $[Cr(CO)_5]$	0.49 LUMO $[AuPCy_3C(Ph)_2]^+$, 0.24 HOMO $[Cr(CO)_4]$
HOMO	0.75 HOMO-1, 0.12 HOMO $[Cr(CO)_5]$	0.91 HOMO-1 $[Cr(CO)_4]$
HOMO-1	0.39 HOMO, 0.14 HOMO-2 $[Cr(CO)_5]$, 0.15 LUMO $[AuPCy_3C(Ph)_2]^+$	0.61 HOMO-2, 0.15 HOMO $[Cr(CO)_4]$
HOMO-2	0.76 HOMO-2 $[Cr(CO)_5]$	0.25 HOMO, 0.24 HOMO-2 $[Cr(CO)_4]$, 0.19 LUMO $[AuPCy_3C(Ph)_2]^+$
HOMO-3	0.65 HOMO $[AuPCy_3C(Ph)_2]^+$	0.69 HOMO-1 $[AuPCy_3C(Ph)_2]^+$

Dissociation energies. The energies required to separate the complexes **13** and **14** into the respective fragments are listed in Table S-11 for fragmentation schemes A and B. The energy of the fragments was computed at the geometry that they adopt in the complex (no relaxation). For complex **13**, the computed energies are similar for fragmentation schemes A and B, while there are considerable differences in the case of complex **14** where the dissociation of the Cr-C1 bond (*i.e.,* fragmentation B) into frozen fragments requires more energy than that of the Au-Cr/C1 bond. This implies a strong Cr-C1 bonding interaction in complex **14**.

Table S-11. Dissociation energies(kcal/mol) of the complexes into frozen fragments (no relaxation) at BP86/TZP(ZORA) level.

	fragmentation A	**fragmentation B**
complex 13	42.44	39.09
complex 14	49.44	63.76

AIM analysis. For further characterization of the bonding, we performed a topological analysis of the electron density distribution using the Atoms-in-Molecules (AIM) method. This method identifies bonds between atoms through so-called bond critical points (*i.e.*, saddle points of the electron density, where the gradient is zero in all directions while the second derivatives are positive along the bond and negative in the two other orthogonal directions). The resulting bond network (with bond critical points indicated as green dots) and the associated density contour maps are shown in Figures S-12 and S-13 for complex **13** and in Figures S-14 and S-15 for complex **1**, respectively.

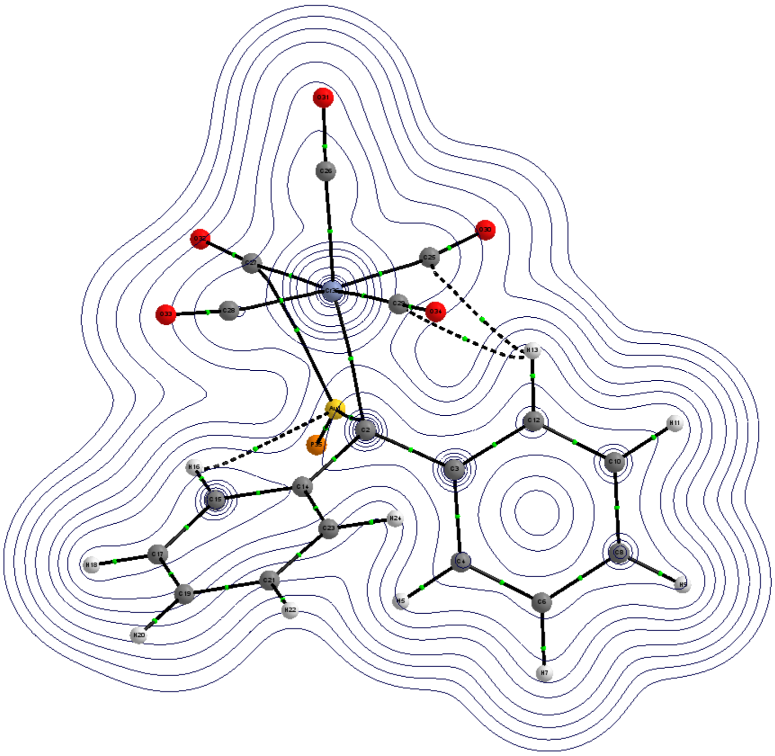

Figure S-12 Graphical representation of bond critical points (green dots) and the electron density contour map in the plane C1, Cr, C_{ipso} as obtained by the AIM method for complex **13**. The ligands at phosphorous are left out for clarity.

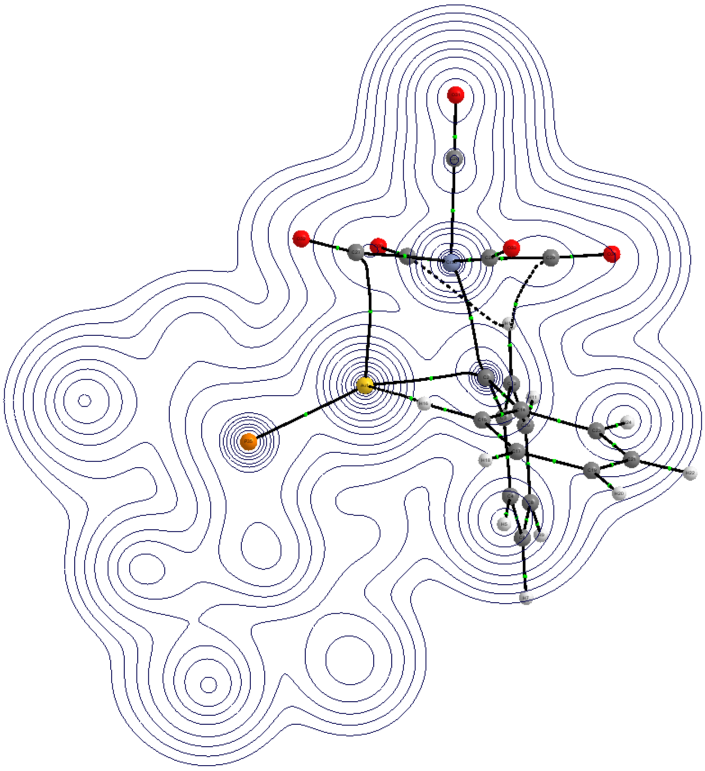

Figure S-13 Graphical representation of bond critical points (green dots) and the electron density contour map in the plane Au, C1, Cr as obtained by the AIM method for complex **13**. The ligands at phosphorous are left out for clarity.

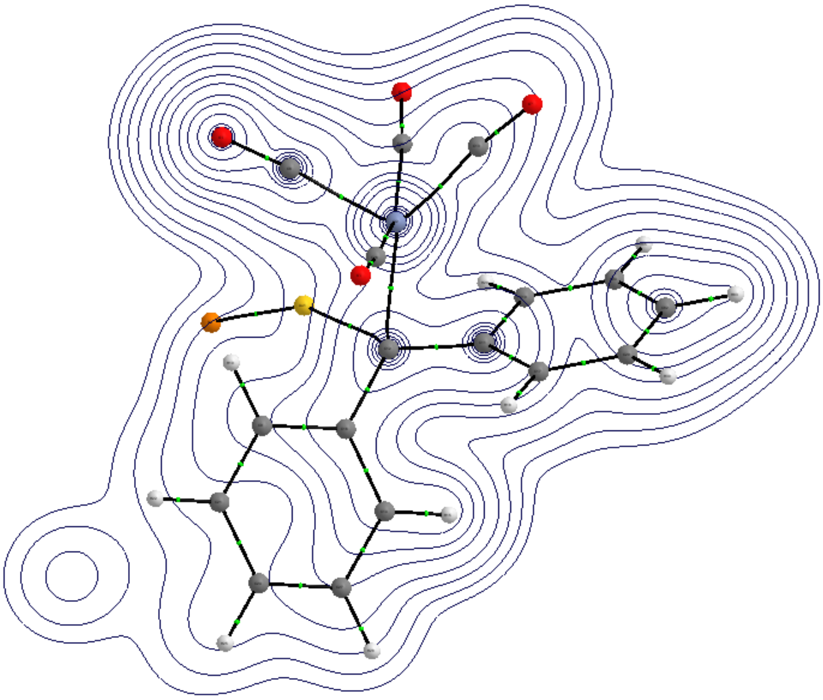

Figure S-14 Graphical representation of bond critical points (green dots) and the electron density contour map in the plane C1, Cr, C_{ipso} as obtained by the AIM method for complex **14**. The ligands at phosphorous are left out for clarity.

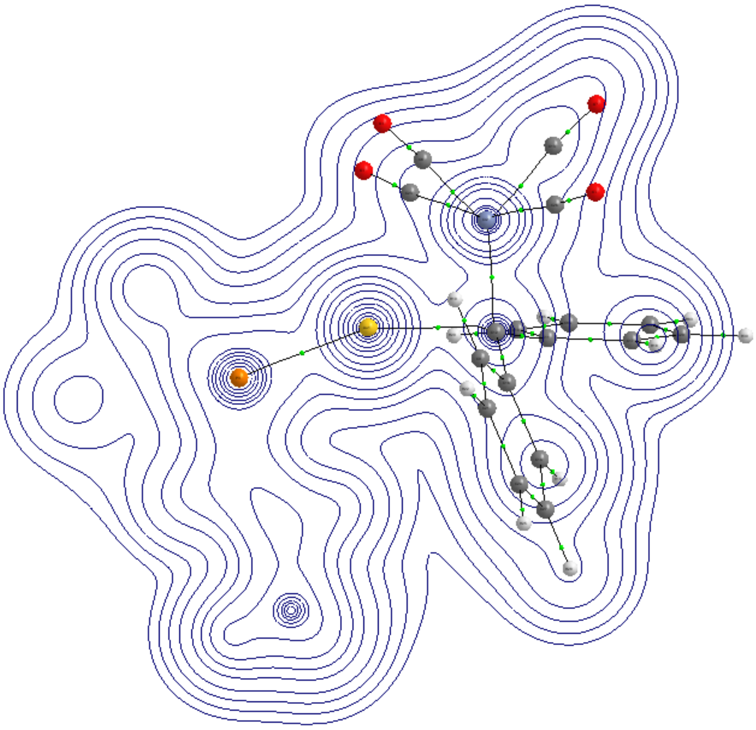

Figure S-15 Graphical representation of bond critical points (green dots) and the electron density contour map in the plane Au, C1, Cr as obtained by the AIM method for complex **14**. The ligands at the phosphorous are left out for clarity.

One should be cautious, however, not to over-interpret the AIM results. It is known that the AIM method may have difficulties to identify bridging bonding interactions. In the present case, the AIM analysis finds a bond critical point between Au and the carbene carbon atom C1 in both complexes (see Figures S-13 and S-15). There is no separate nearby bond critical point between Au and Cr, since the electron density distribution indicates only one bonding path that is directed more towards C1 than to Cr. Moreover, for complex **13** the AIM analysis provides an unexpected bond critical point between Au and a carbonyl group (see Figure S-13), which is in contrast to the low NBO Wiberg bond index of 0.15 and the lack of a distinct orbital interaction in the fragment analysis.

NMR chemical shifts. Experimentally, the NMR chemical shifts have been measured for C_{ipso} and C'_{ipso} in complex **14**. We have calculated these shifts using several computational procedures (for different density functionals and basis sets, without and with inclusion of relativistic effects). The NMR chemical shifts δ are obtained from the computed isotropic shielding constants σ by $\delta = \delta_{ref} + \sigma_{ref} - \sigma$.

As in the experimental work, dichloromethane was chosen as reference. We computed σ_{ref} at the same level as σ, and δ_{ref} was taken from experiment.

Table S-12. Isotropic shielding constants and isotropic chemical shifts calculated at various levels for C_{ipso} and C'_{ipso} in complex **14** (geometry optimized at the BP86/def2-TZVP level).

	functional	**basis set**	**ECP (Au)**	**relativistic**	**Isotropic shielding constant σ /ppm**			**Isotropic chemical shift δ / ppm**		
					CH_2Cl_2	C_{ipso}	C'_{ipso}	C_{ipso}	C'_{ipso}	$\delta_{C'ipso}-\delta_{Cipso}$
	experimental							93	144	51
1	BP86[*]	def2-SVP	def2-ecp	no	118.77	92.99	46.84	79.58	125.73	46.15
2	BP86[*]	[1]	def2-ecp	no	103.95	83.30	33.76	74.45	123.99	49.55
3	B3LYP[*]	[1]	def2-ecp	no	106.38	80.34	29.68	79.84	130.50	50.66
4	BP86[#]	TZP	none	no	108.29	84.49	41.14	77.60	120.95	43.35
5	BP86[#]	TZP	none	Spin-orbit coupling	114.52	84.04	38.20	84.28	130.12	45.84
6	BP86[$]	[2]	SDD	no	107.45	82.80	33.72	78.46	127.53	49.08
7	B3LYP[$]	[2]	SDD	no	109.55	79.79	29.26	83.56	134.09	50.53

[*] Turbomole, [#] ADF, [$] Gaussian, various basis sets: [1] Cr, C_{ipso}, C'_{ipso}, C1 def2-TZVP, others def2-SVP; [2] Au SDD, others 6-311+G**

It is obvious from Table S-12 that the differences between the NMR chemical shifts of C_{ipso} and C'_{ipso} are well reproduced by all computational methods used, with C_{ipso} being remarkably shielded. The shifts themselves are generally underestimated. As expected, the agreement between the calculated and experimental shifts improves upon going from the GGA functional BP86 to the hybrid functional B3LYP (see entries 2 and 3, or entries 6 and 7), upon extending the basis set (see entries 3 and 7), and upon including relativistic corrections (see entries 4 and 5). To provide a best estimate for the NMR shifts, we add to our best non-relativistic result (entry 7) the relativistic corrections (differences of entries 5 and 4), which yields 90.24 ppm for C_{ipso}, 143.26 ppm for C'_{ipso}, and 53.02 ppm for the difference, in good agreement with the experimental values (see Table S-12). The electronic structure obtained from the DFT calculations is thus consistent with the experimental NMR data.

Conclusion. The gold moiety is a weakly bound unit in both complexes: the Cr-C1 bond coordinates in η^2-fashion to the gold moiety. A relatively weak bonding interaction is also seen from the small Wiberg bond indices calculated for the Au-Cr and Au-C1 bonds. The strong Cr-C1 bonding arises from simultaneous σ-donation and π-back-donation, with strong mixing of the respective fragment orbitals. Finally, even though C_{ipso} gets much closer to the chromium atom upon removal of a carbonyl ligand, there is no significant bonding interaction between these two atoms both according to orbital analysis (NBO, fragmentation) and topological analysis of the electron density (AIM).

Appendix D

Cyclization of an α,β-Unsaturated Hydrazone Catalyzed by a BINOL-Phosphoric Acid: Pericyclic or Not?

Berit Heggen, Mahendra Patil and Walter Thiel

J. Comput. Chem., **2016**, 37, 280 – 285.

Carried out and analyzed all the calculations in the paper.

Cyclization of an α,β-Unsaturated Hydrazone Catalyzed by a BINOL-Phosphoric Acid: Pericyclic or Not?

Berit Heggen,[a] Mahendra Patil,[b] and Walter Thiel*[a]

Density functional theory is used to study the mechanism of the title reaction, one of the first catalytic asymmetric 6π-electrocyclizations observed experimentally. The benzylideneacetone-derived phenyl hydrazone is chosen as model substrate for the cyclization reaction, both in the protonated (**A**) and unprotonated (**B**) form, while the isoelectronic carbon analogue, 1,5-diphenylpentadienyl anion (**C**), serves as a reference for comparisons. The barrier to cyclization is computed to be more than 15 kcal/mol lower in **A** compared with **B**, in line with the observed acid catalysis. The relevant transition states to cyclization are characterized for **A** and **C** using orbital inspection, natural bond orbital analysis, nucleus independent chemical shifts, and stereochemical indicators. The cyclization of **C** is confirmed to be pericyclic, while that of **A** can be described as pseudopericyclic ring closure involving an intramolecular nucleophilic addition. © 2015 Wiley Periodicals, Inc.

DOI: 10.1002/jcc.24044

Introduction

Phosphoric acids derived from 1,1′-bi-2-naphthol (BINOL) play an important role in Brønsted acid and hydrogen bonding organocatalysis.[1–3] Brønsted acid catalysis can be used not only for electrophilic activation of the reactant but also for inducing stereoselectivity in the course of the reaction by generating ion pairs of the protonated reactant and the conjugate base of the (chiral) Brønsted acid. This strategy is called asymmetric counterion-directed catalysis.[4]

Müller and List reported an asymmetric intramolecular carbon–nitrogen bond formation in unsaturated hydrazones that is catalyzed by a BINOL-derived phosphoric acid; the proposed catalytic cycle is shown in Figure 1.[5,6] As the putative reactive species is isoelectronic to the pentadienyl anion, they characterized this reaction as catalytic asymmetric 6π-electrocyclization. So far, only few asymmetric electrocyclization reactions are known.[7–10] As it is difficult to fully determine the mechanism of such reactions solely from experiment, we decided to study it computationally using density functional theory (DFT), with focus on the cyclization step highlighted in Figure 1.

In this article, we address the question whether the title reaction is pericyclic or pseudopericyclic or follows some other pathway. Pericyclic reactions are characterized by the existence of a closed-loop 6π molecular orbital at the transition state (TS).[11] DFT computations allow us to check for the presence of such an orbital but also offer other means for TS analysis. One crucial indicator is the aromatic character of the TS (compared with reactants and products), which can be assessed by the nucleus independent chemical shift (NICS) analysis introduced by Schleyer.[12,13] Another criterion is the stereochemistry: pericyclic reactions are stereoselective and obey symmetry-based selection rules. For example, in pericyclic ring closing reactions, the orbitals at the terminal positions forming the new bond have to rotate in a particular concerted manner to satisfy the symmetry requirements for constructive overlap (disrotatory in a thermally allowed 6π-electrocyclization). By contrast, pseudopericyclic reactions are characterized as "concerted transformations whose primary changes in bonding compass a cyclic array of atoms, at one (or more) of which nonbonding and bonding atomic orbitals interchange roles."[14] In pseudopericyclic ring closing reactions, the TS geometry is typically close to planarity, and the 6π orbitals have at least one orbital disconnection, so that aromaticity is not enhanced at the TS. The barriers to pseudopericyclic reactions are usually very small.[15,16]

Methodology

Geometry optimizations were performed using the B3LYP functional[17] along with the 6-31G* basis set,[18,19] which is a common choice for such studies.[10,20] The optimized structures were characterized as minima or TSs by frequency analysis, and intrinsic reaction coordinate (IRC) calculations[21] were performed to connect each TS to the associated reactant and product. More accurate relative energies were obtained from single-point B3LYP calculations at the optimized structures with a larger basis set (6-311+G**) and Grimme dispersion corrections.[22] Solvation effects were taken into account by use of the polarized continuum model (PCM)[23] with chlorobenzene as solvent (as in the experimental work). All computations were done using the Gaussian 09 program package.[24]

Results

We investigated the three systems shown in Figure 2. The parent substrate in the experimental work[5,6] was the

[a] *B. Heggen, W. Thiel*
Max-Planck-Institut für Kohlenforschung, Kaiser-Wilhelm-Platz 1, 45470 Mülheim an der Ruhr, Germany
E-mail: thiel@kofo.mpg.de
[b] *M. Patil*
Centre for Excellence in Basic Sciences Health Centre, University of Mumbai, Vidhyanagaria Campus, Mumbai 400098, India

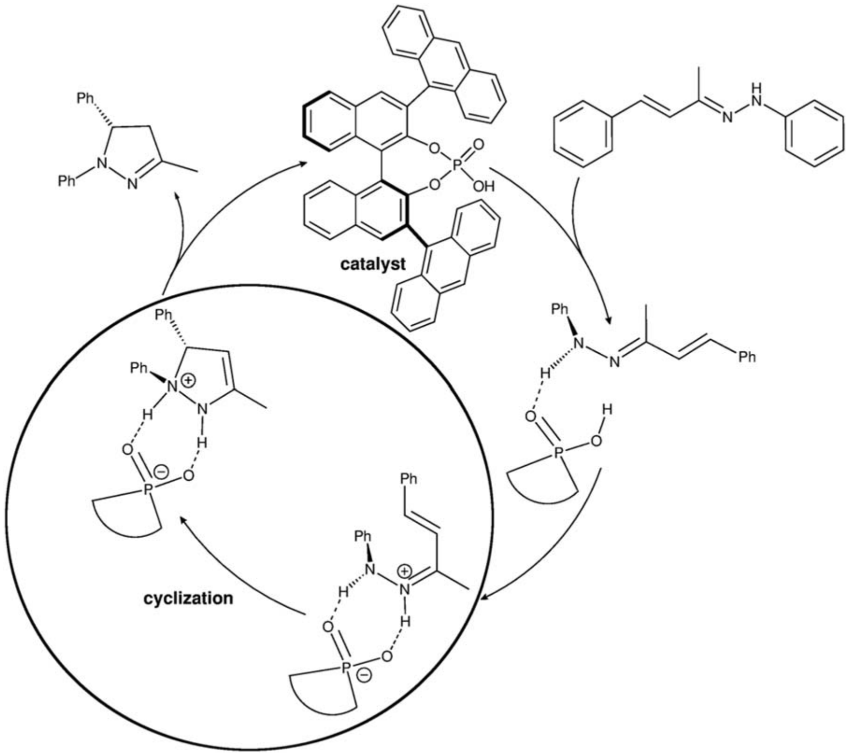

Figure 1. Proposed catalytic cycle for the ring closing reaction[5,6] highlighting the cyclization step investigated here.

benzylideneacetone-derived phenyl hydrazone, which we consider both in its protonated (**A**) and unprotonated (**B**) form to gauge the effect of acid catalysis. The isoelectronic carbon analogue **C** (1,5-diphenylpentadienyl anion) serves as a reference that is known to cyclize in a pericyclic manner.[25] For each of these three substrates, we studied the cyclization reaction (shown in Fig. 3 for **A**) by optimizing the structures of the reactant **1** and product **2** as well as the corresponding TSs.

In the following, we report the results of calculations on these three model systems. In the case of **A**, we do not include the conjugate base of the catalyst, and we check only at a final stage whether the essential features of the computed cyclization mechanism for **A** remain the same when the conjugate base is coordinated.

On cyclization of **A**, two stereocenters are formed: one at N1 and one at C5 (cf. Fig. 3). In principle, the phenyl groups can be oriented either *cis* or *trans* to each other in the product. TSs for both pathways could be located for **A**, and correspondingly also for **B**; it should be noted, however, that IRC computations starting from TS-*trans* of **B** do not lead to a planar reactant but another reactant minimum with the phenyl group at N1 already rotated out of the molecular plane. By contrast, we found only one TS for **C**, namely TS-*cis* for the allowed disrotatory ring closure, whereas TS-*trans* for the formally forbidden conrotatory process was elusive at the chosen computational level. To obtain the experimentally observed product, the cyclization must be followed by a deprotonation for **A** and **C** and by a proton shift from N1 to N2 for **B**.

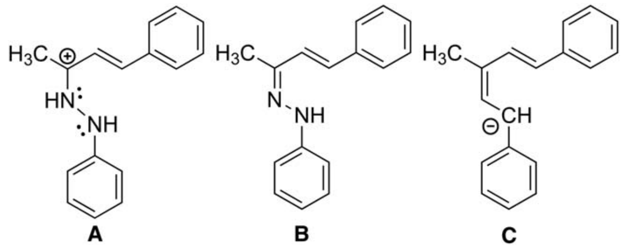

Figure 2. Schematic drawing of the three systems studied: protonated hydrazone **A**, unprotonated hydrazone **B**, and the carbon analogue, pentadienyl anion **C**. Only one of the resonance structures of **A** is shown.

Table 1 lists the relative single-point free energies (PCM/B3LYP-D/6-311+G**//B3LYP/6-31G*) for all minima and TSs of the three model systems. Further energies as well as the optimized geometries are documented in the Supporting Information.

First of all, it is obvious that acid catalysis reduces the activation barrier for the cyclization considerably. This agrees well with the experimental finding that no reaction is observed without adding an acid.[5,6] The computed reaction barrier for the cyclopentadienyl anion **C** is rather high. Literature values for DFT barriers of various pericyclic reactions cover a fairly large range and slightly depend on substituents and functionals.[26,27] High-level *ab initio* calculations predict a gas-phase activation energy of 36–37 kcal/mol for **C** while B3LYP overestimates this value by about by 5–6 kcal/mol,[27] which is in line with our present results (see Supporting Information Table 1, gas-phase energy barrier of 42.7 kcal/mol for **C**). We consider this to be tolerable as our focus is on the qualitative description of the reaction.

To gain more detailed mechanistic insight, we performed a natural bond order (NBO) analysis to determine charges, bonding

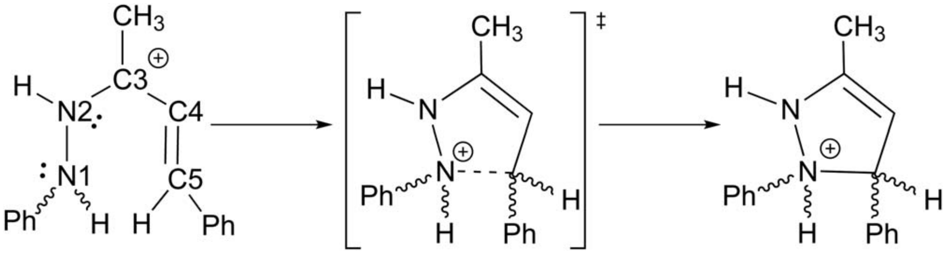

Figure 3. Reaction equation for the investigated cyclization of **A**.

parameters, and the occupation of lone pairs and π orbitals. The results are summarized in Tables 2 and 3, respectively.

We first compare **1-A** and **1-B**. On protonation, the substituents at N1 of the reactant are rotated out of the molecular plane to an almost perpendicular position. The net positive charge in **1-A** is mainly localized at C3 and C5. There is only one π double bond (C4–C5) in **A** compared with two such double bonds in **B** (N2–C3 and C4–C5). On protonation, both nitrogen atoms keep their lone pairs, but their occupations are reduced, and there is an antibonding admixture of a partially filled *p*-orbital at C3. The occupations in the *p*- and π-orbitals sum up to almost six.

We next compare **1-A** and **1-C**. The electron distribution in **1-C** is affected by the lack of heteroatoms and the presence of a plane of symmetry. The charge is rather evenly distributed over the five central atoms C1–C5, and the corresponding bond orders are rather uniform, pointing to a delocalized system. There are two double bonds C1–C2 and C4–C5 in **1-C** compared with just one double bond C4–C5 in **A**. These two double bonds are accompanied by a partially filled *p*-orbital at C3. The populations in this *p*-orbital and the two relevant π-orbitals sum up to less than five electrons (cf. Tables 2 and 3). Closer inspection of the NBO analysis shows that there is considerable delocalization in **1-C** with electrons being moved to antibonding π*-orbitals. Moreover, the π-system on the five central atoms C1–C5 is in conjugation with the π-system of the adjacent phenyl rings, which should involve a total of 18 π-electrons. Summing up the populations of all *p*-, π-, and π*-orbitals indeed yields a value very close to 18 (as expected).

The electron distribution in **1-A** changes when moving to the TS. On bond formation between N1 and C5, the respective bond order increases from almost zero to 0.4–0.6 at the TS and further to 0.8–0.9 in the product. The *cis*- and *trans*-TS of **A** have similar electronic structures. The lone pairs at the nitrogen atoms are kept, while the corresponding charges and occupations change slightly. Conversely, the double bond is shifted to C3–C4 while the partially filled *p*-orbital is moved to C5, and the NBO analysis does not yet yield any bonding orbital between N1 and C5. Again, the populations in the *p*- and π-orbitals sum up to six.

Table 1. Relative free energies for the protonated hydrazone A, the unprotonated hydrazone B, and the pentadienyl anion C in kcal/mol (PCM/B3LYP-D/6-311+G**//B3LYP/6-31G*).

ΔG (kcal/mol)	A	B	C
1	0	0	0
TS-*trans*	18.49	34.35	–
TS-*cis*	15.71	32.85	34.64
2-*trans*	10.80	29.52	–
2-*cis*	12.36	30.52	23.75

The *cis*-cyclization of **B** proceeds in a disrotatory manner. At TS-*cis*, the new N1–C5 bond is partially formed, with a bond order of 0.60; the double bond is kept but shifted to C3–C4, and a second lone pair appears at N2. In the *trans*-cyclization (which is connected to a nonplanar reactant minimum, see above), the TS also has a partially formed N1–C5 bond (bond order of 0.54), but no double bond; instead there is new partially filled lone pair at C3. In both cases, the populations of the relevant orbitals sum up to six. However, only TS-*cis* exhibits the characteristic features of a pericyclic conjugated TS.

The disrotatory TS-*cis* in the pure carbon analogue **C** is also pericyclic, but its electronic structure is somewhat different. While the negative charge is mainly localized at C2 and C4 and there is a C2–C3 double bond formed, the NBO analysis finds a second double bond (C4–C5) for TS-*cis*, populated with around 1.4 electrons. The electron distribution at TS-*cis* seems to be right in between reactant and product. A new σ-orbital along the C1–C5 bond is already formed at the TS, which is part of the extended conjugated system characteristic of 6π-electrocyclizations. The populations of this new σ-orbital and of the π- and π*-orbitals at atoms C1–C5 sum up to six, and there is no delocalization into the adjacent phenyl rings.

The product of the heterosystem **A** has a distinct C3–C4 double bond (bond order of 1.8) and a lone pair localized at N2. Formally, the initial product of *cis*-cyclization of **B** is a zwitterion with tetracoordinated N1 and doubly coordinated N2 (which is then stabilized by a proton transfer from N1 to N2); the electronic structure of the initial product is quite similar to that of **A** having a C3–C4 double bond and two lone pairs at N2 (due to the zwitterionic character). The product of **C** is a cyclic carbanion with a delocalized π-system (e.g., with equal bond orders of 1.4 for C2–C3 and C3–C4).

In a pericyclic 6π-electrocyclization, the six electrons need to be located in a closed-loop cyclic array at the TS, giving rise to a corresponding in-phase ring orbital. No such orbital can be identified on close inspection of the high-lying occupied orbitals of **A** at the TS (for orbital correlations between the reactant and TS of **A** see the Supporting Information). Pericyclic reactions are associated with an aromatic TS, and hence we tested the character of the computed TSs through a NICS analysis as originally introduced by Schleyer in 1996.[12] NICS

Table 2. NBO analysis for the ring atoms in the reactant 1, the TS and the product 2 of the protonated hydrazone A, the unprotonated hydrazone B, and the pentadienyl anion C: charges and occupation of lone pairs from natural population analysis; antibonding orbitals are marked by*.

		Charge			Occupation of lone pairs		
	Atom	A	B	C	A	B	C
1	N1/C1	−0.47	−0.41	−0.34	1.86	1.70	
	N2/C2	−0.35	−0.26	−0.20	1.57	1.92	
	C3	0.35	0.18	−0.17	0.80*		1.18
	C4	−0.34	−0.26	−0.20			
	C5	−0.04	−0.22	−0.34			
TS-*trans*	N1/C1	−0.37	−0.34		1.63		
	N2/C2	−0.45	−0.45		1.80	1.92	
	C3	0.25	0.21			0.91	
	C4	−0.37	−0.49				
	C5	0.02	−0.05		0.69		
TS-*cis*	N1/C1	−0.35	−0.31	−0.26	1.58		
	N2/C2	−0.44	−0.47	−0.43	1.81	1.92 and 1.55	
	C3	0.22	0.19	−0.05			
	C4	−0.36	−0.48	−0.43			
	C5	−0.01	−0.06	−0.26	0.72		
2-*trans*	N1/C1	−0.29	−0.31				
	N2/C2	−0.46	−0.50		1.89	1.94 and 1.63	
	C3	0.17	0.18				
	C4	−0.31	−0.49				
	C5	−0.05	−0.05				
2-*cis*	N1/C1	−0.29	−0.30	−0.25			
	N2/C2	−0.46	−0.51	−0.46	1.88	1.94 and 1.62	
	C3	0.18	0.17	−0.04			
	C4	−0.32	−0.49	−0.53			1.41
	C5	−0.05	−0.05	−0.25			

values are a very suitable measure of aromaticity.[13,15,16,28–31] They are computed as the negative of the absolute shielding constant, typically at the ring center. They reflect the diamagnetic ring current; negative NICS values indicate aromaticity. As the ring current is usually governed by the π-system, it is customary to evaluate the NICS values also below or above

Table 3. NBO analysis for the bonding in the reactant 1, the TS and the product 2 of the protonated hydrazone A, the unprotonated hydrazone B, and the pentadienyl anion C: bond lengths in Å, Wiberg bond orders (BO), and occupation of π bonding orbitals; antibonding orbitals are marked by*.

		Bond length/Å			BO			Occupation of π bonds		
	Bond	A	B	C	A	B	C	A	B	C
1	N1–N2/C1–C2	1.40	1.35	1.39	1.02	1.14	1.50			1.80
	N2–C3/C2–C3	1.33	1.30	1.42	1.40	1.68	1.34		1.92	
	C3–C4	1.42	1.47	1.42	1.28	1.10	1.33			
	C4–C5	1.37	1.35	1.39	1.55	1.76	1.50	1.72	1.98	1.80
	C5–N1/C5–C1	2.99	3.03	3.30	0.02	0.02	0.04			
TS-*trans*	N1–N2/C1–C2	1.41	1.44		1.02	1.02				
	N2–C3/C2–C3	1.40	1.34		1.11	1.42				
	C3–C4	1.35	1.39		1.67	1.45		1.86		
	C4–C5	1.45	1.45		1.14	1.17				
	C5–N1/C5–C1	2.12	1.88		0.36	0.54				
TS-*cis*	N1–N2/C1–C2	1.42	1.42	1.47	1.02	1.04	1.16			
	N2–C3/C2–C3	1.40	1.35	1.40	1.09	1.36	1.43			1.84
	C3–C4	1.35	1.38	1.40	1.70	1.52	1.43	1.88 and 0.35*	1.88	
	C4–C5	1.46	1.47	1.47	1.13	1.12	1.16			1.44
	C5–N1/C5–C1	2.04	1.82	1.97	0.42	0.60	0.61			
2-*trans*	N1–N2/C1–C2	1.47	1.48		0.97	0.95				
	N2–C3/C2–C3	1.43	1.36		1.03	1.34				
	C3–C4	1.34	1.37		1.80	1.55		1.94	1.93	
	C4–C5	1.50	1.50		1.02	1.02				
	C5–N1/C5–C1	1.61	1.58		0.79	0.82				
2-*cis*	N1–N2/C1–C2	1.46	1.47	1.52	0.98	0.96	1.01			
	N2–C3/C2–C3	1.43	1.36	1.41	1.03	1.33	1.48			1.91
	C3–C4	1.34	1.37	1.39	1.79	1.56	1.40	1.94	1.93	
	C4–C5	1.50	1.50	1.52	1.02	1.03	1.02			
	C5–N1/C5–C1	1.65	1.60	1.59	0.75	0.81	0.94			

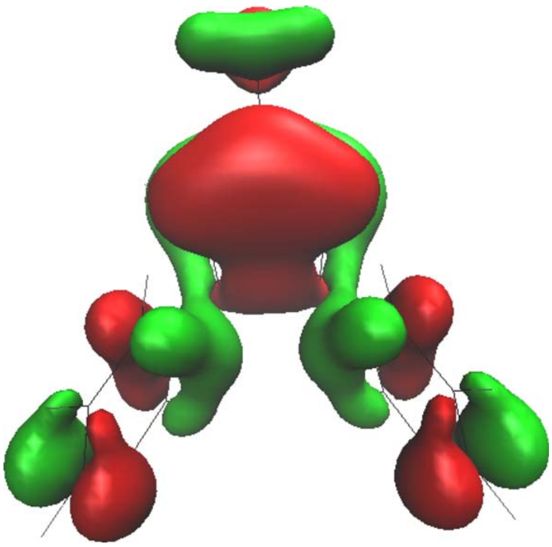

Figure 4. In-phase orbital at TS-*cis* of the carbon analogue **C**.

the ring plane to get a clearer picture. In the case of an aromatic TS connecting a nonaromatic reactant to a nonaromatic product, the NICS values will have a minimum at the TS.

In the case of **C**, there is a characteristic cyclic ring orbital for TS-*cis* (see Fig. 4), and the NICS values have a distinct minimum at TS-*cis* in the ring plane (position 0), see Table 4. The NICS values above and below the ring plane differ quite strongly because of the influence of the phenyl substituents (both above the plane in the *cis*-case), but they generally remain smallest at the TS compared with reactant and product (at all positions except at −2.0 Å). The cyclization of **C** via TS-*cis* is thus confirmed to be pericyclic, in line with the rule that an allowed thermal 6π-electrocyclization needs to be attended by a disrotatory motion of the terminal groups.

Given the large differences between the NICS values above and below the ring plane even in the case of the reference molecule **C**, it seems most appropriate to use the values in the ring plane (position 0) for characterization in the less clear-cut cases of **A** and **B**. The corresponding NICS values for **B** show a minimum at both TSs for cyclization, which is, however, more pronounced for the disrotatory TS-*cis*. The NICS analysis thus confirms that the *cis*-cyclization of **B** can be characterized as pericyclic, as suggested by the NBO analysis and the similarity in the computed barriers for **B** and **C** (see above and Table 1). For **A**, there is no pronounced NICS minimum in the ring plane (position 0) for either of the two TS structures (see Table 4).

In additional exploratory calculations, we considered the influence of the coordination of the conjugated base of the acidic catalyst on the reaction. In the cyclization of **A**, the four possible diastereomeric TSs are now all distinct, but the reaction mechanism remains qualitatively the same, and the same applies to the stereochemical outcome of the reaction. Furthermore, the relevant orbitals in the reactant and the TSs do not change significantly on coordination of the conjugated base. We refrain from a more detailed quantitative discussion because our calculations with added conjugate base only explored these qualitative aspects without being comprehensive. Therefore, these calculations did not offer insights into the origin of the experimentally observed enantioselectivity.[5,6]

Discussion and Conclusions

In summary, the cyclization of **A** cannot be classified as a pericyclic reaction because it does not follow a concerted disrotatory path and does not involve an aromatic TS. By contrast, the cyclization of the isoelectronic carbon analogue **C** via TS-*cis* is a pericyclic reaction as it fulfills these criteria. Likewise, the cyclization of the unprotonated hydrazone **B** appears to be pericyclic; hence, the protonation of the hydrazone leads to a loss of the pericyclic nature of the cyclization. This is related to the geometrical deformation of the planar reactant **B** on protonation to **A**, involving an out-of-plane twist of the phenyl group at N1 that prevents a concerted disrotatory motion on cyclization.

Table 4. NICS values calculated for the reactant 1, the TS for cyclization, and the product 2 at the geometric center of the ring atoms N1/C1–N2/C2–C3–C4–C5 (position 0), at four points above the ring plane (0.5, 1.0, 1.5, and 2.0 Å vertically from the center of the ring, on the same side as the phenyl group at N1/C1) and correspondingly at four points below the ring plane.

Position	−2.0	−1.5	−1.0	−0.5	0	0.5	1.0	1.5	2.0
Protonated hydrazone **A**									
1	−0.04	−0.07	0.05	0.77	1.43	0.59	−0.25	−0.25	−0.1
TS-*trans*	−0.11	−0.98	−2.84	−4.50	−3.57	−0.80	0.64	0.90	0.79
TS-*cis*	0.38	0.25	−0.48	−2.65	−5.75	−5.57	−2.89	−1.04	−0.41
2-*trans*	−0.48	0.09	−1.15	−3.54	−4.45	−3.27	−1.35	−0.17	−1.06
2-*cis*	0.22	−0.16	−1.30	−3.58	−5.13	−4.14	−2.13	−0.64	−1.27
Unprotonated hydrazone **B**									
1	−0.60	−1.03	−1.63	−1.36	0.23	0.89	0.30	−0.07	−0.03
TS-*trans*	−0.28	−1.19	−3.26	−5.53	−4.89	−1.89	−0.17	0.17	−0.15
TS-*cis*	−0.06	−0.59	−1.80	−4.06	−6.87	−6.85	−4.22	−2.06	−1.22
2-*trans*	0.71	0.13	−1.19	−2.63	−2.69	−1.37	−0.20	0.38	0.53
2-*cis*	−0.01	−0.58	−1.86	−3.88	−4.52	−3.16	−1.71	−0.84	−2.16
Cyclopentadienyl anion **C**									
1	−0.10	−0.26	−0.33	0.16	0.59	−0.01	−0.52	−0.38	−0.18
TS-*cis*	−0.05	−0.35	−1.29	−3.76	−7.24	−7.79	−5.40	−2.97	−1.64
2-*cis*	0.01	−0.29	−0.58	−0.89	−1.35	−1.16	0.15	0.92	4.45

The cyclization of **A** seems to be a pseudopericyclic reaction considering the planar TS geometry and the presence of cyclic orbitals with disconnections. We note, however, that our computed barriers of about 16–18 kcal/mol (cf. Table 1) are rather high compared with those reported for other pseudopericyclic reactions, which normally range from 0 to 10 kcal/mol according to B3LYP calculations.[15,16,30,32] Qualitatively, pseudopericyclic reactions are often assumed to be essentially barrierless.

The cyclization of **A** may also be considered as a nucleophilic addition, with the lone pair at N1 attacking C5 as part of an allylic moiety (C3–C4–C5 with positively charged C3). This notion is supported by the NBO analysis that reveals a strong donation from the lone pair at N1–C5 at the TS: the E(2) donor–acceptor interaction is 84.2 kcal/mol for TS-*trans* and 103.8 kcal/mol for TS-*cis*, respectively. This scenario would resemble a 5-*endo*-trig reaction which is assumed to be disfavored according to Baldwin's rules,[33] which are, however, only qualitative and may be less reliable for systems containing heteroatoms.[34–37] Recently, Johnston et al. demonstrated that also all-carbon systems may preferentially cyclize in a 5-*endo*-trig manner.[38] They probed by DFT computations whether an electrocyclization is reasonable but had to exclude this pathway. In any event, the concepts of pseudopericyclic ring closure and intramolecular nucleophilic addition do not exclude each other as they address different aspects and are based on different view points (electronic structure and nucleophilicity). The title reaction may thus well be described in both terms.

To conclude, our DFT computations show that the cyclization of **A** is not of pericyclic nature. It may be characterized as a pseudopericyclic ring closure involving an intramolecular nucleophilic addition.

Acknowledgments

The authors thank Prof. Benjamin List for suggesting a theoretical study of the title reaction and for valuable discussions. We are grateful to the reviewers for constructive comments. This article is dedicated to Paul von Ragué Schleyer, one of the great pioneers in computational chemistry.

Keywords: density functional theory · nucleus independent chemical shift · transition state · electrocyclization · pseudopericyclic

How to cite this article: B. Heggen, M. Patil, W. Thiel. *J. Comput. Chem.* **2016**, *37*, 280–285. DOI: 10.1002/jcc.24044

Additional Supporting Information may be found in the online version of this article.

[1] M. Terada, *Chem. Commun.* **2008**, 4097.
[2] X. Yu, W. Wang, *Chem. Asian J.* **2008**, *3*, 516.
[3] A. Moyano, R. Rios, *Chem. Rev.* **2011**, *111*, 4703.
[4] M. Mahlau, B. List, *Angew. Chem. Int. Ed.* **2013**, *52*, 518.
[5] S. Müller, B. List, *Angew. Chem. Int. Ed.* **2009**, *48*, 9975.
[6] S. Müller, B. List, *Synthesis* **2010**, *13*, 2171.
[7] S. Thompson, A. G. Coyne, P. C. Knipe, M. D. Smith, *Chem. Soc. Rev.* **2011**, *40*, 4217.
[8] X. P. Yin, X. P. Zeng, Y. L. Liu, F. M. Liao, J. S. Yu, F. Zhou, J. Zhou, *Angew. Chem. Int. Ed.* **2014**, *53*, 13740.
[9] A. Das, C. M. R. Volla, I. Atodiresei, W. Bettray, M. Rueping, *Angew. Chem. Int. Ed.* **2013**, *52*, 8008.
[10] S. Raja, M. Nakajima, M. Rueping, *Angew. Chem. Int. Ed.* **2015**, *54*, 2762.
[11] S. M. Bachrach, Computational Organic Chemistry; Wiley: Hoboken, New Jersey, **2007**.
[12] P. v. R. Schleyer, C. Maerker, A. Dransfeld, H. Jiao, N. J. R. van Eikema Hommes, *J. Am. Chem. Soc.* **1996**, *118*, 6317.
[13] Z. Chen, C. S. Wannere, C. Corminboeuf, R. Puchta, P. v. R. Schleyer, *Chem. Rev.* **2005**, *105*, 3842.
[14] J. A. Ross, R. P. Seiders, D. M. Lemal, *J. Am. Chem. Soc.* **1976**, *98*, 4325.
[15] A. R. de Lera, R. Alvarez, B. Lecea, A. Torrado, F. P. Cossio, *Angew. Chem. Int. Ed.* **2001**, *40*, 557.
[16] J. Rodríguez-Otero, E. M. Cabaleiro-Lago, *Chem. Eur. J.* **2003**, *9*, 1837.
[17] A. D. J. Becke, *J. Chem. Phys.* **1993**, *98*, 5648.
[18] R. Ditchfield, W. J. Hehre, J. A. Pople, *J. Chem. Phys.* **1971**, *54*, 724.
[19] M. J. Frisch, J. A. Pople, *J. Chem. Phys.* **1984**, *80*, 3265.
[20] C. Zhou, D. M. Birney, *J. Am. Chem. Soc.* **2002**, *124*, 5231.
[21] K. Fukui, *Acc. Chem. Res.* **1981**, *14*, 363.
[22] S. Grimme, J. Antony, S. Ehrlich, H. Krieg, *J Chem. Phys.* **2010**, *132*, 154104.
[23] J. Tomasi, B. Mennucci, R. Cammi, *Chem. Rev.* **2005**, *105*, 2999.
[24] M. J. Frisch, G. W. Trucks, H. B. Schlegel, G. E. Scuseria, M. A. Robb, J. R. Cheeseman, G. Scalmani, V. Barone, B. Mennucci, G. A. Petersson, H. Nakatsuji, M. Caricato, X. Li, H. P. Hratchian, A. F. Izmaylov, J. Bloino, G. Zheng, J. L. Sonnenberg, M. Hada, M. Ehara, K. Toyota, R. Fukuda, J. Hasegawa, M. Ishida, T. Nakajima, Y. Honda, O. Kitao, H. Nakai, T. Vreven, J. A. Montgomery, Jr., J. E. Peralta, F. Ogliaro, M. Bearpark, J. J. Heyd, E. Brothers, K. N. Kudin, V. N. Staroverov, T. Keith, R. Kobayashi, J. Normand, K. Raghavachari, A. Rendell, J. C. Burant, S. S. Iyengar, J. Tomasi, M. Cossi, N. Rega, J. M. Millam, M. Klene, J. E. Knox, J.-B. Cross, V. Bakken, C. Adamo, J. Jaramillo, R. Gomperts, R.-E. Stratmann, O. Yazyev, A. J. Austin, R. Cammi, C. Pomelli, J. W. Ochterski, R. L. Martin, K. Morokuma, V. G. Zakrzewski, G. A. Voth, P. Salvador, J. J. Dannenberg, S. Dapprich, A. D. Daniels, O. Farkas, J. B. Foresman, J. V. Ortiz, J. Cioslowski, D. J. Fox, Gaussian 09, Rev. B.01; Gaussian: Wallingford, CT, **2010**.
[25] R. Huisgen, *Angew. Chem. Int. Ed.* **1980**, *19*, 947.
[26] M. Elango, V. Subramanian, *J. Phys. Chem. A* **2005**, *109*, 11870.
[27] T. P. M. Goumans, A. W. Ehlers, K. Lammerstma, E. U. Würthwein, S. Grimme, S. *Chem. Eur. J.* **2004**, *10*, 6468.
[28] H. Jiao, P. v. R. Schleyer, *J. Phys. Org. Chem.* **1998**, *11*, 655.
[29] N. Gupta, R. K. Bansal, M. v. Hopffgarten, G. Frenking, *J. Phys. Org. Chem.* **2011**, *24*, 786.
[30] E. M. Cabaleiro-Lago, J. Rodríguez-Otero, S. M. Varela-Varela, A. Pena-Gellego, J. M. Hermida-Ramón, *J. Org. Chem.* **2005**, *70*, 3921.
[31] J. Rodríguez-Otero, E. M. Cabaleiro-Lago, *Angew. Chem. Int. Ed.* **2002**, *41*, 1147.
[32] W. M. F. Fabian, V. Bakulev, C. O. Kappe, *J. Org. Chem.* **1998**, *63*, 5801.
[33] K. Gilmore, I. V. Alabugin, *Chem. Rev.* **2011**, *111*, 6513.
[34] C. Chatgilialoglu, C. Ferreri, M. Guerra, V. Timokhin, G. Froudakis, T. Gimisis, *J. Am. Chem. Soc.* **2002**, *124*, 10765.
[35] J. Ichikawa, G. Lapointe, Y. Iwai, *Chem. Commun.* **2007**, 2698.
[36] T. Kleine, K. Bergander, R. Fröhlich, B. Wibbeling, E. U. Würthwein, *J. Org. Chem.* **2011**, *76*, 1979.
[37] C. P. Johnston, A. Kothari, T. Sergeieva, S. I. Okovytyy, K. E. Jackson, R. S. Paton, M. D. Smith, *Nat. Chem.* **2015**, *7*, 171.
[38] J. P. Snyder, *J. Org. Chem.* **1980**, *45*, 1341.

Received: 9 May 2015
Revised: 17 July 2015
Accepted: 20 July 2015

Appendix E

Theoretical Investigation on the Mechanism of Iron Catalyzed Cross Coupling Reactions via Ferrate Intermediates

Berit Heggen and Walter Thiel

J. Organomet. Chem., **2016**, 804, 42 – 47.

Carried out and analyzed all the calculations in the paper.

Journal of Organometallic Chemistry 804 (2016) 42–47

Contents lists available at ScienceDirect

Journal of Organometallic Chemistry

journal homepage: www.elsevier.com/locate/jorganchem

Theoretical investigation on the mechanism of iron catalyzed cross coupling reactions via ferrate intermediates

Berit Heggen, Walter Thiel*

Max-Planck-Institut für Kohlenforschung, Kaiser-Wilhelm-Platz 1, 45470 Mülheim an der Ruhr, Germany

ARTICLE INFO

Article history:
Received 23 October 2015
Received in revised form
14 December 2015
Accepted 20 December 2015
Available online 23 December 2015

Keywords:
Iron
Cross coupling
DFT
Mechanism
Alkylation

ABSTRACT

Iron is a versatile catalyst for cross coupling reactions. These reactions may proceed either via classical redox cycles involving low-valent iron species or via highly alkylated organoferrate complexes. Experimentally, it is difficult to trap reactive intermediates, but it has been possible to prepare iron complexes similar to the supposed active catalyst that are able to methylate activated electrophiles (J. Am. Chem. Soc. 130 (2008) 8773–8787). Motivated by these experiments we studied the methylation of 4-chlorobenzoyl chloride by the organoferrate complex $[(Me)_4\ Fe(MeLi)][Li(OEt_2)]_2$ employing density functional theory at the OPBE/6-311+G** level, as well as B3LYP/6-311+G** calculations with explicit inclusion of dispersion and solvent effects (describing iron with the QZVP basis and SDD pseudopotential). In the preferred mechanism, methyl transfer takes place via substitution at the organoferrate complex, with the leaving methyl group being replaced by chloride. In line with the experimental findings, up to four methyl groups can be transferred in this manner. By locating all conceivable transition states and intermediates, the calculations shed light on the relative ease of substitution at the various positions of the organoferrate complex, both in the first and subsequent methyl tranfers. Transition states for an alternative redox mechanism could not be located.

1. Introduction

In recent years iron has emerged as a versatile catalyst in cross coupling reactions [1–9]. In contrast to cross coupling reactions catalyzed by *e.g.* palladium or copper, the underlying mechanisms are not yet well understood in the case of iron. There is consensus that the mechanism may vary depending on reagents and precursors [10–13]. Generally speaking, there are two main alternatives: either so-called -ate mechanisms involving highly alkylated iron species [14] or catalytic redox cycles consisting of up to three formal steps: oxidative addition, transmetalation, and reductive elimination. For the latter, different experimental and computational studies proposed different oxidation states for the low-valent iron center [11,15–22].

Experimentally, the mechanisms of iron catalyzed cross coupling reactions are difficult to elucidate because any reactive intermediates formed in situ are expected to be unstable and short-lived. Fürstner and coworkers succeeded in synthesizing several iron complexes believed to be similar to the reactive intermediates and tested their activity in cross coupling reactions [23]. Among others, they prepared the organoferrate complex **1**, $[(Me_4\ Fe)(MeLi)][Li(OEt_2)]_2$ (*cf.* Fig. 1), which could be crystallized for structure determination and was shown to transfer one or several methyl groups to activated substrates such as acid chlorides and enol triflates [23,24]. The methylation may proceed either by a substitution reaction, in which the methyl group is directly transferred to the substrate, or by a two-step reaction with an oxidative addition and a reductive elimination step. Motivated by the experimental findings on complex **1** [23], we decided to analyze the mechanism of the corresponding methyl transfers using density functional theory (DFT).

To choose the most suitable DFT level for this ferrate complex, we first tested several functionals and basis sets, and we also identified the most probable spin state. The findings from this initial stage are included in the next section describing the computational methodology. Thereafter we present our computational results on the mechanism of methylation.

---

* Corresponding author.
E-mail address: thiel@kofo.mpg.de (W. Thiel).

http://dx.doi.org/10.1016/j.jorganchem.2015.12.026

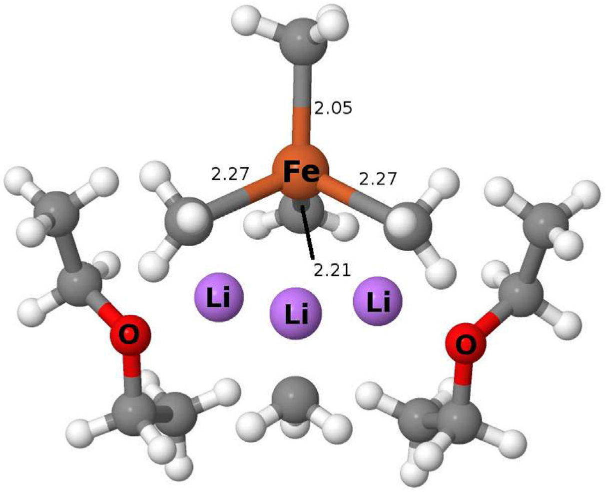

Fig. 1. Crystal structure of organoferrate complex **1** from Ref. [23] (color code: carbon atoms in gray, hydrogen atoms in white). Key distances are given in Å. (For interpretation of the references to colour in this figure legend, the reader is referred to the web version of this article.)

2. Computational methods

We performed DFT calculations to investigate the iron complex **1** and its reactions. Previous DFT benchmarks on transition metal complexes [25,26], in particular iron complexes, suggested that the OPBE functional gives a good description of spin states [27,28]. We thus initially adopted the OPBE functional and applied it in combination with the 6-311+G** basis set [29–31], while using the LANL2DZ pseudopotential and basis set for the iron atom [32–34].

To determine the preferred spin state, complex **1** was optimized as singlet, triplet, and quintet, starting in each case from the crystal structure. Table 1 lists the resulting relative energies and the RMSD values (root mean square deviations) relative to the crystal structure; the selected bond lengths and angles included in the RMSD evaluation are given in the Supporting Information, Table SI-1. The quintet state is lowest in energy followed by the triplet state and, still higher, the singlet state. The RMSD values clearly show that the computed geometry of the quintet is closest to the crystal structure, whereas the geometries of the singlet and triplet deviate strongly. Hence, the ground state of complex **1** is a quintet (consistent with an oxidation state of +2 for iron).

For further validation, we tested additional functionals that are recommended in the literature for transition metal complexes [35–39]: M06 [40], B3LYP [41,42], B3LYP+D with D3 dispersion corrections [38], and TPSSh [43]. Complex **1** was optimized in the quintet state using these functionals. We again chose the 6-311+G** basis set for all atoms except iron, which was described by the SDD basis set and pseudopotential [44]. All optimizations were started from the crystal structure. Table 2 collects the RMSD values for the same set of bond lengths and angles as before (mainly around the central iron-methyl tetrahedron, see Table SI-1).

Table 1
Energies and free energies (relative to the quintet state) and RMSD values of the optimized geometries with respect to the crystal structure of complex **1** (OPBE/6-311+G**, Fe: LANL2DZ).

Spin state	Singlet	Triplet	Quintet
E (kcal/mol)	34.56	17.24	0.00
G (kcal/mol)	39.93	20.66	0.00
RMSD bonds (Å)	0.19	0.13	0.07
RMSD angles (°)	13.5	15.5	4.7

Table 2
RMSD values of the optimized quintet geometries with respect to the crystal structure of complex **1** for various functionals (basis set: 6-311+G**, SDD for iron).

Functional	OPBE	M06	B3LYP	B3LYP+D	TPSSh
RMSD bonds (Å)	0.07	0.13	0.09	0.11	0.13
RMSD angles (°)	4.7	5.7	4.7	5.6	6.0

The smallest errors in geometry (compared to the crystal structure) are indeed found for the quintet structures computed with the OPBE functional closely followed by B3LYP. Larger deviations, especially for bond angles, are obtained with M06, B3LYP+D, and TPSSh. Given these results we decided to perform geometry optimizations using the OPBE functional employing the LANL2DZ basis set and pseudopotential for iron; for brevity this standard computational setup is termed OPBE-level.

For further analysis the geometries optimized at the OPBE-level were used for single-point calculations with several other functionals (BP86, B3LYP, B3LYP+D, TPSSh, M06) and/or larger basis sets such as QZVP [45] or SDD [32,46] for iron (SDD pseudopotential as well). When appropriate, solvent effects were taken into account by using the polarizable continuum model (PCM) [47] with THF as solvent (as in the experiment). All calculations were carried out using the Gaussian09 program package, revision D.01 [48]. Harmonic frequencies were calculated for all stationary points to confirm them as minima (no imaginary frequency) or transition states (one imaginary frequency) and to compute zero-point energy corrections (at 238.15 K, the temperature used in the experiments). Additionally, intrinsic reaction coordinate calculations (IRC) [49] were performed to ensure that the transition states connect to the expected reactants and products, taking 30 IRC steps in each direction with subsequent optimization of the resulting geometry. This always led to the correct minimum structures of reactants and products.

3. Results and discussion

As exemplary reaction we first studied the transfer of a methyl group from complex **1** to 4-chlorobenzoyl chloride **2**, see Scheme 1. As can be seen, **1** carries in total five methyl groups. Four of them are directly bound to the central iron atom forming a tetrahedral coordination sphere. The fifth methyl group is farther away from the central iron atom (3.84 Å compared to 2.05 to 2.27 Å) being coordinated to the three lithium atoms in-between. To distinguish these five methyl groups they are colored differently in Scheme 1. The black methyl group is in the top position (in short: to), the two red ones are equivalent by symmetry and occupy the back position (ba), the blue one is in the front position (fr), and the green one is located below the lithium atoms in the bottom position (bo).

For the oxidative addition-reductive elimination mechanism, we located an intermediate with the substrate **2** being attached to the iron complex **1**, both in the triplet and quintet state (Fig. 2). The free energy relative to the separated reactants is 1.11 kcal/mol for the quintet species and 0.45 kcal/mol for the triplet species (*i.e.* 0.66 kcal/mol lower in free energy). In both cases, the carbonyl carbon C1 is bound to the central iron atom (Fe–C1: quintet, 1.98 Å; triplet: 1.81 Å), thereby distorting the tetrahedral coordination sphere around iron, while the chlorine atom binds to the free lithium atom (Li–Cl: quintet, 2.13 Å; triplet, 2.10 Å); the pertinent Li–O distances are similar (quintet, 2.08 and 2.16 Å; triplet, 2.12 and 2.17 Å). In the quintet intermediate the iron atom remains almost at the center of a distorted tetrahedron, whereas in the triplet state the Fe[Me]$_4$-unit with the attached substrate is turned away from the center of the lithium triangle. We did not manage to locate any

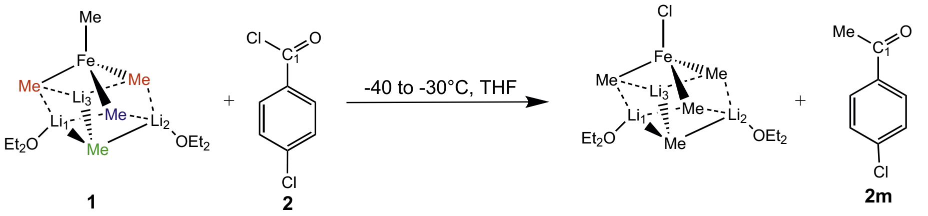

Scheme 1. Investigated reaction for the alkylation of 4-chlorobenzoyl chloride **2** by ferrate complex **1**; reaction conditions are indicated. To highlight the different methyl groups they are colored (black: top, red: back, blue: front, green: bottom).

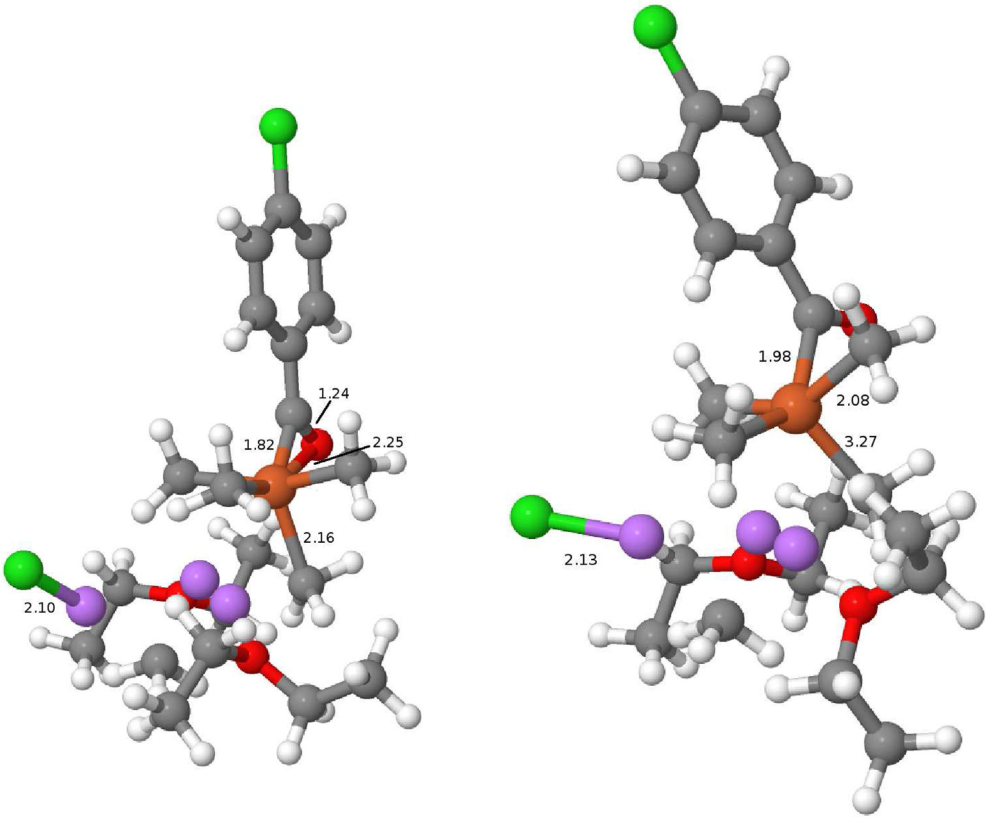

(a) triplet (b) quintet

Fig. 2. Putative intermediate structures for the addition of 4-chlorobenzoyl chloride **2** to complex **1** in the triplet state (left) and the quintet state (right) (color code: gray: carbon, white: hydrogen, brown: iron, violet: lithium, red: oxygen, green: chlorine). Key distances are given in Å.

transition state for oxidative addition or reductive elimination that would connect these intermediates to reactants or products. Scans of the quintet potential energy surface indicate that the oxidative addition step will require somewhat more activation than the substitution reaction (see below) and that the subsequent reductive elimination step should be facile. We also did not find any corresponding pathways when allowing for intersystem crossing (as commonly encountered in iron chemistry).

On the other hand, we could locate distinct transition states (TS) for the substitution pathway in the quintet state. As an example, Fig. 3 shows the transition state for the transfer of the methyl group at the top position of complex **1** to substrate **2**. This transition state is consistent with a substitution mechanism. The transition vector (imaginary frequency: 435i cm^{-1}) describes the motion of the methyl-carbon (Me) along a straight line between iron and the carbonyl carbon C1 of substrate **2**. The angle between Fe, Me, and C1 is 171°, and the Fe—Me and Me—C1 distances are 2.19 and 2.12 Å, respectively. For comparison, the corresponding Fe—Me distance in the isolated ferrate complex **1** is 2.05 Å, and the C1—Me bond length in the product is 1.51 Å. The hydrogen atoms of the migrating methyl group invert upon moving from the ferrate complex towards **2**. Moreover, the closer the methyl group gets towards the carbonyl group, the farther away moves the chloride bound to the carbonyl carbon (C1—Cl: quintet reactant, 1.80 Å; quintet TS, 1.95 Å). In fact, following the IRC path towards the products indicates some kind of double substitution: the chloride of substrate **2** is replaced by a methyl group from **1** but then moves into the free coordination site at the iron center, replacing the methyl group and thereby keeping the ferrate complex in shape.

Analogous transition states in the quintet state were located for the transfer of methyl groups from the back and bottom positions, and their nature was confirmed by frequency analysis and IRC

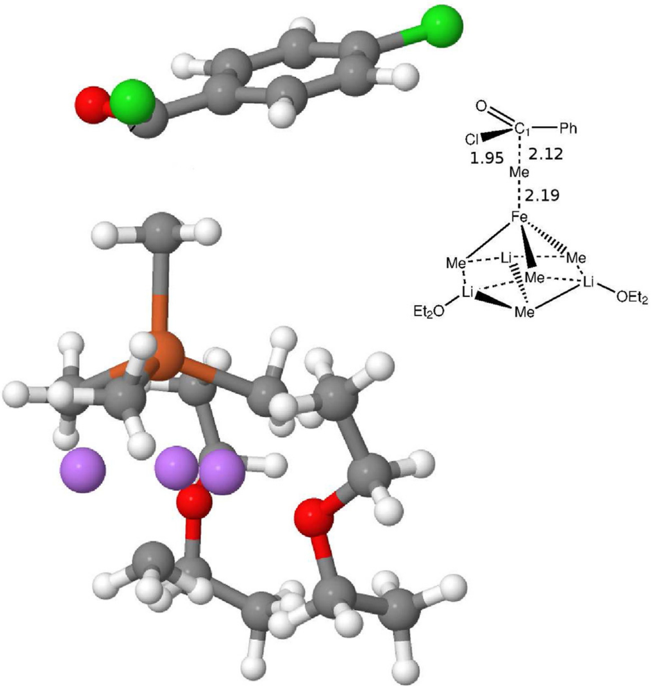

Fig. 3. Transition state for the transfer of the methyl group from the top position of complex **1** to 4-chlorobenzoyl chloride **2** in the quintet state (color code: gray: carbon, white: hydrogen, brown: iron, violet: lithium, red: oxygen, green: chlorine). Key distances are given in Å.

calculations as well. A similar transition state could also be found at the front position, but IRC calculations failed to connect it with the expected product but yielded an unreasonably distorted structure (probably because of steric hindrance by the nearby ether groups). Therefore, we do not further consider methyl transfer from the front position in the following.

Table 3 lists Gibbs free energies of the three transition states relative to the separated reactants **1** and **2** at infinite distance (for relative energies see Table SI-2 in the Supporting Information). Geometries were fully optimized at the OPBE-level (entry 1) and at the B3LYP+D-level (entry 9). Single-point calculations were performed at the OPBE-optimized geometries (all other entries) to assess the effects of various computational options (functionals, basis sets, pseudopotentials, solvent effects, dispersion corrections); zero-point energies and thermal corrections were taken from harmonic frequency calculations at the OPBE-level.

Table 3
Relative Gibbs free energies of the transition states in the quintet state for single methyl transfers from the back, bottom, and top positions. Entries 1 and 9 are optimized, the others represent single-point calculations at the geometries obtained at the OPBE-level. Energies are given in kcal/mol relative to separated reactants. Basis set: 6-311+G**; for iron the basis set and pseudopotential are indicated individually in the footnotes.

Entry	Method	Top	Back	Bottom
1 opt	OPBE[a]	28.67	26.72	28.40
2	OPBE[b]	21.83	28.08	23.02
3	OPBE[c]	29.78	26.82	28.45
4	OPBE[d]	28.04	26.26	28.09
5	OPBE[e]	20.72	27.42	22.63
6	B3LYP[d]	28.26	23.43	25.59
7	B3LYP+D[d]	21.80	14.17	18.08
8	B3LYP+D[e]	14.11	16.06	12.97
9 opt	B3LYP+D[e]	17.63	12.80	17.69
10	BP86[d]	21.88	17.19	20.68
11	M06[d]	22.36	16.67	21.23
12	TPSSh[d]	25.09	20.52	23.48

[a] Fe: LANL2DZ (basis set and pseudopotential).
[b] Fe: LANL2DZ (basis set and pseudopotential), PCM (THF).
[c] Fe: SDD (basis set and pseudopotential).
[d] Fe: QZVP, SDD (pseudopotential).
[e] Fe: QZVP, SDD (pseudopotential), PCM (THF).

The trends are generally the same for the relative energies and relative free energies of the three transition states, so we will focus on the latter in the following (Table 3). The OPBE results indicate that the choice of basis set and pseudopotential has only a minor influence on the relative free energies (up to 1 kcal/mol, see entries 1, 3, and 4 as well as 2 and 5). Comparing the results of different functionals using the large QZVP basis and the SDD pseudopotential at iron shows that OPBE generally yields the highest barriers: the computed values are lower for B3LYP by 0–3 kcal/mol (entries 4 vs. 6), for BP86 by 6–9 kcal/mol (entries 4 vs. 10), for M06 by 6–10 kcal/mol (entries 4 vs. 11), and for TPSSh by 3–6 kcal/mol (entries 4 vs. 12); in all cases, the computed barriers are lowest for methyl transfer at the back position, while those at the top and bottom positions tend to be somewhat larger and of similar magnitude. Explicit inclusion of dispersion effects at the B3LYP level lowers the computed barriers substantially, by 6–9 kcal/mol (entries 6 vs. 7), and brings them rather close, within 1–3 kcal/mol, to those obtained from the M06 functional that implicitly accounts for dispersion (entries 7 vs. 11). Inclusion of solvent effects via PCM(THF) significantly lowers the computed barriers at the top and bottom positions, by 7–8 and 5 kcal/mol, respectively, and slightly increases them by 1–2 kcal/mol at the top position (entries 1 vs. 2, 4 vs. 5, and 7 vs. 8).

Obviously, the chosen computational methods predict quite different barriers, and it is hard to decide *a priori* on the most trustworthy approach. The OPBE functional seems least suitable for the energetics in view of the fact that modern functionals with a good track record in transition metal chemistry (M06, TPSSh) give much smaller barriers. Moreover, dispersion and solvent effects appear to be quite large and non-uniform in the present case, and should thus be both included explicitly. Therefore, we decided to re-optimize all relevant species at the B3LYP+D level using the large QZVP basis and the SDD pseudopotential at iron and representing solvent effects through PCM (THF); we consider the resulting free energy barriers to be our most reliable results (entry 9). At this B3LYP+D level, the lowest barrier is found for the methyl transfer at the back position (12.8 kcal/mol), significantly smaller than those at the top and bottom positions (17.6–17.7 kcal/mol). The reaction at the back position is also favored by other approaches (see *e.g.* entries 6 and 10–12), which however predict larger values since they do not account for dispersion and/or solvent effects.

For the sake of completeness, we also considered reactions in the triplet and singlet states as intersystem crossings are common in iron chemistry. Only some of the corresponding transition states for methyl transfer could be located, but they were always much higher in energy than those in the quintet state. Therefore we conclude that spin crossings do not play a role in the substitution reactions investigated presently.

It is known from experiment that not only one methyl group is transferred per complex **1** but three or four. Therefore we located transition states for the whole sequence of methyl transfers between complex **1** and 4-chlorobenzoyl chloride **2** (without considering the methyl group in the front position, as discussed above). The geometries were first optimized at the OPBE-level and then re-optimized at the B3LYP+D-level. Generally, the geometries of the transition states for the second, third, and fourth methyl transfer are qualitatively quite similar to those for the first transfer.

The relative Gibbs free energies for all transition states are documented in the Supporting Information (see Table SI-3). Here, we present in Table 4 only the relative Gibbs free energies for three of the most probable sequences of multiple transfers, *i.e.* those with the lowest barriers to overcome, and visualize them in Fig. 4. The free energy barriers are given in Table 4 relative to the preceding minimum, while the Gibbs free energies are plotted in Fig. 4 with respect to the separated reactants (**1** and four molecules of **2**).

We only comment on the results obtained by geometry optimization at the B3LYP+D-level with inclusion of dispersion and solvent effects, which is the most reliable approach applied presently (see above, Table 3, entry 9). The most favorable sequence starts with a substitution at back position, followed by substitution at the bottom and the second back position (ba-bo-ba), with barriers of similar magnitude (9.1–13.6 kcal/mol), while the fourth substitution at the remaining top position (to) is notably less facile (18.7 kcal/mol). The alternative ba-ba-bo-to sequence has a very similar free energy profile. When the reaction starts at the top position, the initial free energy barrier is higher (17.6 kcal/mol) while the following steps in the to-ba-bo-ba sequence are quite facile. The computed barriers indicate that the transfer of three methyl groups per ferrate complex is probable (if the first one is feasible) whereas the fourth transfer is less likely (involving the less favorable substitution at the top position). Generally speaking, the barriers for methyl transfer at the back and top positions remain similar regardless whether they occur in the first or subsequent steps, whereas those at the top position are lowered substantially in later steps (presumably because of the changes in the ligand sphere of complex **1**).

Experimentally, the methylation of 4-chlorobenzoyl chloride **2** by complex **1** is very facile and fast (complete consumption of 0.57 mmol of **2** within 20 min at −30 to −40°) [23]. In line with these findings, we compute the overall reaction to be strongly exergonic (see Fig. 4). The computed free energy barriers are clearly much too high at the OPBE-level, but more realistic at the preferred B3LYP+D level with inclusion of dispersion and solvent effects (maximum barrier of 13.6 kcal/mol for the first three steps). It is known from the literature that B3LYP does generally reasonably well in estimating reaction barriers, with a slight tendency to overestimate them [50,51]. We also note that experimentally there may be some side reactions, because 100% conversion was reported to lead to a yield of 60% [23]. Given these caveats, we feel that the B3LYP+D results are in reasonable agreement with the experimental findings.

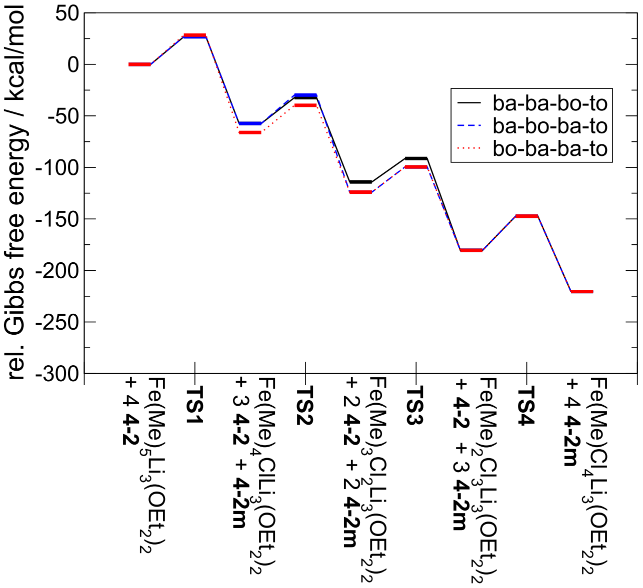

(a) optimized: OPBE/6-311+G** Fe: LANL2DZ

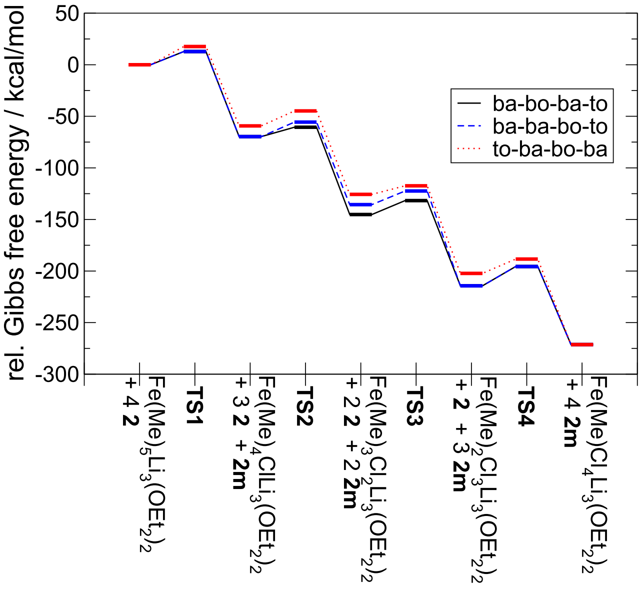

(b) optimized: B3LYP+D/6-311+G**, Fe: QZVP, SDD (pseudopotential), PCM (THF)

Fig. 4. Free energy profiles for subsequent transfer of methyl groups from complex **1** to **2**, relative to the separated reactants. The sequences of transfer positions are indicated in the figures (see text). (For interpretation of the references to colour in this figure legend, the reader is referred to the web version of this article.)

4. Conclusion

For the presently investigated ferrate complex **1**, the OPBE functional gives a reasonable geometry but overestimates the barriers for methyl transfer significantly. The most realistic free energy profiles are provided by the B3LYP+D approach with explicit inclusion of dispersion and solvent effects. At this level, the transfer of the methyl group at the back position of **1** is most facile, with a free energy barrier of 12.8 kcal/mol. Subsequent transfers of methyl groups from the bottom and the second back position are essentially as facile, while the fourth transfer from the top position requires some more activation. These computational results are in qualitative agreement with the experimental observation of multiple methyl transfers at low temperatures and short reaction times. Transition states for an alternative two-step mechanism, oxidative addition followed by reductive elimination, could not be located.

Table 4
Free energy barriers in kcal/mol for consecutive transfer of different methyl groups from complex **1** to substrate molecules **2**, each relative to the preceding minimum.

Sequence	1st	2nd	3rd	4th
OPBE/6-311+G** Fe: LANL2DZ, optimized				
ba-ba-bo-to	26.72	25.05	22.73	33.18
ba-bo-ba-to	26.72	27.55	24.49	33.18
bo-ba-ba-to	28.40	26.38	24.49	33.18
B3LYP+D/6-311+G** Fe: QZVP, SDD (pseudopotential), PCM (THF), optimized				
ba-bo-ba-to	12.80	9.07	13.64	18.69
ba-ba-bo-to	12.80	14.15	13.12	18.69
to-ba-bo-ba	17.63	14.50	8.34	13.89

The present DFT calculations confirm that iron catalyzed cross coupling reactions involving methyl donors can proceed via organoferrate intermediates (such as complex **1**) through a direct substitution mechanism.

Acknowledgments

We thank Prof. Alois Fürstner for suggesting a theoretical study on the ferrate complex and its alkylation mechanism and for valuable discussions on this topic. BH is grateful to Dr. Gopinadhanpillai Gopakumar for advice and guidance during the initial stages of the project and fruitful discussions.

Appendix A. Supplementary data

Supplementary data related to this article can be found at http://dx.doi.org/10.1016/j.jorganchem.2015.12.026.

References

[1] A. Fürstner, A. Leitner, M. Méndez, H. Krause, J. Am. Chem. Soc. 124 (2002) 13856–13863.
[2] T. Hatakeyama, S. Hashimoto, K. Ishizuka, M. Nakamura, J. Am. Chem. Soc. 131 (2009) 11949–11963.
[3] W.M. Czaplik, M. Mayer, J. Cvengroš, A.J. von Wangelin, ChemSusChem 2 (2009) 396–417.
[4] T. Kauffmann, Angew. Chem. Int. Ed. 35 (1996) 386–403.
[5] A. Rudolph, M. Lautens, Angew. Chem. Int. Ed. 48 (2009) 2656–2670.
[6] D. Gärtner, A. Luiz, S. Grupe, J. Arp, A.J. von Wangelin, Angew. Chem. Int. Ed. 54 (2015) 10545–10549.
[7] I. Bauer, H.-J. Knölker, Chem. Rev. 115 (2015) 3170–3387.
[8] E. Nakamura, N. Yoshikai, J. Org. Chem. 75 (2010) 6061–6067.
[9] G. Cahiez, A. Moyeux, J. Cossy, Adv. Synth. Catal. 357 (2015) 1983–1989.
[10] B. Scheiper, M. Bonnekessel, H. Krause, A. Fürstner, J. Org. Chem. 69 (2004) 3943–3949.
[11] J. Kleimark, P.-F. Larsson, P. Emamy, A. Hedström, P.-O. Norrby, Adv. Synth. Catal. 354 (2012) 448–456.
[12] D. Noda, Y. Sunada, K. Hatakeyama, M. Nakamura, H. Nagashima, J. Am. Chem. Soc. 131 (2009) 6078–6079.
[13] B.D. Sherry, A. Fürstner, Acc. Chem. Res. 41 (2008) 1500–1511.
[14] R.B. Bedford, P.B. Brenner, E. Carter, P.M. Cogswell, M.F. Haddow, J.N. Harvey, D.M. Murphy, J. Nunn, C.H. Woodall, Angew. Chem. Int. Ed. 53 (2014) 1804–1808.
[15] R.B. Bedford, Acc. Chem. Res. 48 (2015) 1485–1493.
[16] S. Malhotra, P.S. Seng, S.G. Koenig, A.J. Deese, K.A. Ford, Org. Lett. 15 (2013) 3698–3701.
[17] A. Hedström, E. Lindstedt, P.-O. Norrby, J. Org. Chem. 748 (2013) 51–55.
[18] J. Kleimark, A. Hedström, P.-F. Larsson, C. Johansson, P.-O. Norrby, ChemCatChem 1 (2009) 152–161.
[19] M. Guisán-Ceinos, F. Tato, E. Bunuel, P. Calle, D.J. Caárdenas, Chem. Sci. 4 (2013) 1098–1104.
[20] Q. Ren, S. Guan, F. Jiang, J. Fang, J. Phys. Chem. 117 (2013) 756–764.
[21] A. Bekhradnia, P.-O. Norrby, Dalton Trans. 44 (2015) 3959–3962.
[22] S.L. Daifuku, J.L. Kneebone, B.E.R. Snyder, M.L. Neidig, J. Am. Chem. Soc. 137 (2015) 11432–11444.
[23] A. Fürstner, R. Martin, H. Krause, G. Seidel, R. Goddard, C.W. Lehmann, J. Am. Chem. Soc. 130 (2008) 8773–8787.
[24] C.-L. Sun, A. Fürstner, Angew. Chem. Int. Ed. 52 (2013) 13071–13075.
[25] C.J. Cramer, D.G. Truhlar, Phys. Chem. Chem. Phys. 11 (2009) 10757–10816.
[26] M. Swart, A.W. Ehlers, K. Lammertsma, Mol. Phys. 102 (2004) 2467–2474.
[27] J.P. Perdew, K. Burke, M. Ernzerhof, Phys. Rev. Lett. 77 (1996) 3865–3868.
[28] A.J. Cohen, N.C. Handy, Mol. Phys. 99 (2001) 607–615.
[29] R. Ditchfield, W.J. Hehre, J.A. Pople, J. Chem. Phys. 54 (1971) 724728.
[30] R. Krishnan, J.S. Brinkley, R. Seeger, J.A. Pople, J. Chem. Phys. 72 (1980) 650–654.
[31] M.J. Frisch, J.A. Pople, J. Chem. Phys. 80 (1984) 3265–3269.
[32] T.H. Dunning, P.J. Hay, Modern Theoretical Chemistry, vol. 3, Plenum, 1977.
[33] P.J. Hay, W.R. Wadt, J. Chem. Phys. 82 (1985) 299–310.
[34] P.J. Hay, W.R. Wadt, J. Chem. Phys. 82 (1985) 270–283.
[35] O. Salomon, M. Reiher, B.A. Hess, J. Chem. Phys. 117 (2002) 4729–4737.
[36] Y. Zhao, D.G. Truhlar, Acc. Chem. Res. 41 (2008) 157–167.
[37] R. Valero, R. Costa, I.de.P.R. Moreira, D.G. Truhlar, F. Illas, J. Chem. Phys. 128 (2008) 114103.
[38] S. Grimme, J. Antony, S. Ehrlich, H. Krieg, J. Chem. Phys. 132 (2010) 154104.
[39] K.P. Jensen, Inorg. Chem. 47 (2008) 10357–10365.
[40] Y. Zhao, D.G. Truhlar, Theor. Chem. Acc. 120 (2008) 215–241.
[41] A.D.J. Becke, J. Chem. Phys. 98 (1993) 5648–5652.
[42] C. Lee, W. Yang, R.G. Parr, Phys. Rev. B 37 (1988) 785–789.
[43] J.M. Tao, J.P. Perdew, V.N. Staroverov, G.E. Scuseria, Phys. Rev. Lett. 91 (2003) 146401.
[44] D. Andrae, U. Haeussermann, U. Dolg, H. Stoll, H. Preuss, Theor. Chim. Acta 77 (1990) 123–141.
[45] F. Weigend, R. Ahlrichs, Phys. Chem. Chem. Phys. 7 (2005) 3297–3305.
[46] M. Dolg, U. Wedig, H. Stoll, H. Preuss, J. Chem. Phys. 86 (1987) 866–872.
[47] J. Tomasi, B. Mennucci, R. Cammi, Chem. Rev. 105 (2005) 2999–3093.
[48] M. J. Frisch et al., Gaussian, Inc., Wallingford CT (2010).
[49] K. Fukui, Acc. Chem. Res. 14 (1981) 363–368.
[50] G.T. de Jong, D.P. Geerke, A. Diefenbach, F.M. Bickelhaupt, Chem. Phys. 313 (2005) 261–270.
[51] A. Kazaryan, E.J. Baerends, J. Comp. Chem. 34 (2013) 870–878.